ISSN **2960-9534**
DOI https://doi.org/10.36073/2960-9534

JOURNAL OF THE GEORGIAN CERAMISTS' ASSOCIATION

INTERNATIONAL JOURNAL OF CERAMICS, COMPOSITES, SCIENCE AND ADVANCED TECHNOLOGIES

Scientific, technical and industrial illustrated, registered, referral magazine

Vol. 27. 2(54).2025

Guidelines for submitting an article to the journal

- It is necessary to submit, one hardcopy of the article, as well as an electronic versionin English language, to editorial office.
- The length of the article is not limited to pages (including tables and images with appropriate numbering). Interval 1.5. Program-Sylfaen. Font size 12, the article must be accompanied by an abstract in Georgian of no more than 300 words.
- The article should use International System of Units (SI), as well as those units that are equated to this system.
- Mathematical and chemical formulas should be clearly indicated so that the difference between Capital (upper case) and Nuskhuri (Georgian script AD 800-1100) (lower case) letters, quality coefficient and co-multiplier can be easily discerned. All letter designations in the text of the article and formula are subject to decoding. Different concepts can not be represented by the same symbol.
- The literary source should be indicated at the end of the article as follows: for a book - indicating the author, title, title of publication, place of publication, year of publication and total number of pages;

  for a journal - indicating the author of the article, the name of the journal, year of publication, volume, number, beginning and end pages of the article;

  Foreign surnames, the title of the book and journal must be in the original language without abbreviation, it is not allowed to refer to unpublished work.
- When using a copyright certificate, it is necessary to refer to the bulletin of the invention (where the formula of the invention is published) indicating the number and year of publication.
- Pictures and drawings should be presented only in text in one copy in computerized form, they should not be overloaded with details and inscriptions. The position must be indicated by numbers and decoded by inscriptions under the picture;
- The article must be signed by one of the authors. It is necessary to indicate place of work, position, scientific degree, and telephone number.
- The publishing fee for foreign authors not residing in Georgia makes up 100 euros. It's free for authors residing in Georgia.

CONTENTS

UDC 691.42

STUDY OF CLAY SHALES FROM THE DURUJI RIVER GORGE FOR THE PRODUCTION OF POROUS THERMAL INSULATION MATERIALS

L. Gabunia, I. Kamushadze, E. Shapakidze, I. Gejadze, T. Petriashvili

Ivane Javakhishvili Tbilisi State University, Alexander Tvalchrelidze Caucasian Institute of Mineral Resources. 11 Mindeli str., 0186, Tbilisi, Georgia

E-mail: lamgabunia@gmail.com, elena.shapakidze@tsu.ge

Resume: ***Goal.*** The aim of this work is to study the clay shales of the Duruji River gorge to identify the possibility of their use as the main raw in the production of porous thermal insulation materials.

Method. Chemical and petrographic analysis methods were used.

The X-ray phase analysis was carried out using a Dron-4.0 diffractometer ("Burevestnik", St. Petersburg, Russia) with a Cu-anode and a Ni-filter. U=35kv. I=20mA. Intensity - 2 degrees / min. λ=1.54178 Å.

For DTA, a NETZSCH derivatograph with STA-2500 REGULUS thermogravimetric and differential thermal analyzer (TG / DTA) was used. Samples were heated to 1000 ° C, in a ceramic crucible, heating rate 10 °C / min. Reference substance a-Al_2O_3.

Results. Three different types of clay shales were studied under laboratory conditions. Granulometric, X-ray diffraction, and differential thermal analysis were conducted. Heat treatment of the samples in a laboratory electric furnace revealed their ability to expand within a temperature range of 1280–1300°C. The samples were porous in volume, but of non-uniform size and uneven pore distribution.

In order to improve the technological parameters and expand the swelling range, further research was carried out to unify the shale compositions with adjustments to their chemical composition. The shale adjustments were made using natural rocks containing gas-forming substances.

The adjustments to the shale compositions had a positive effect on the properties of the compositions - the temperature at which the mixture transitions to the pyroplastic state was reduced and the pore structure of the samples improved.

As a result of studies at lower temperatures, composites based on clay shale adjusted with natural additives were obtained, characterized by a uniform porous structure.

Conclusion. The conducted research confirmed the possibility of obtaining porous thermal insulation materials based on clay shales from the Duruji Gorge when processing them in the high-temperature range without the addition of foaming agents and the use of refractory molds.

Key words: clay shales of the Duruji River gorge, swelling, heat treatment, porous thermal insulation material.

1. INTRODUCTION

The growth of construction in modern conditions has revealed the need to develop new technologies for the production of thermal insulation materials that, along with technical properties, are easy and inexpensive to produce.

In these conditions, the development of technology for the production of these materials based on natural and inexpensive raw materials is particularly relevant, ensuring the production of new effective thermal insulation materials using a simplified technology, without the addition of foaming agents and the use of refractory forms.

Research conducted in this direction over the past years [1–4] has established the possibility of using waste from the processing of natural rocks as the main raw material for this purpose.

The results of the research showed particular interest in the use of clay shales, which exhibited the ability to swell during heat treatment.

In clay shales, the presence of gas-forming substances in finely dispersed rocks predetermines the possibility of swelling processes occurring during thermal treatment of the rock, which ensures the manifestation of a porous structure in heat-treated samples.

2. MAIN PART

The material for the research was three types of clay shales from the Duruji River gorge.

Results and discussion

A comprehensive study of clay shales was conducted to identify the possibility of their use in the production of silicate thermal insulation materials as the main raw.

For the experiments, three different types of clay shales were selected, located in different parts of the Duruji Gorge, in which, over a number of years, as a result of mudflows, a huge amount of rubble and sand has accumulated, filling the Duruji River basin.

The collected material is a heterogeneous mixture consisting of clays and colloidal particles, rock fragments, etc. The bulk is non-structural and consists mainly of clay fractions and sludge.

All three types of samples collected from individual sites were studied in detail in laboratory conditions.

Shales are quite heterogeneous in their particle size distribution. Each type consists of fragments larger than 10 mm, as well as flat stones of medium and small sizes. The third fraction, a sludge, consists primarily of fine particles (Table 1).

Chemical analysis of all three fractions revealed an almost identical content of the main components in the form of Al_2O_3, $FeO+Fe_2O_3$ and only a 4–5% variation in the content of SiO_2; in the fine fraction, there was no carbon and a low humus content (Table 2).

According to spectral analysis, in all cases the presence of Zn, Ba, Cu, Pb in minimal quantities was detected.

According to differential thermal analysis (Fig. 1), during thermal treatment of shales, a moment of release of hydrated water was detected at a temperature of ~100°C; at 450–720°C, a decrease in mass by 4% is noted; in the temperature range of 500–800°C, the appearance of an exothermic effect is noted, caused, in all likelihood, by the oxidation of iron, dehydration of mica, and the burnout of organic impurities.

According to X-ray phase (Fig. 2) and petrographic analyses, the rocks contain siltstone and psamic structures, argillites, feldspar, quartz, hydromica, biotite, plagioclase, chlorite, muscovite and kaolinite.

Table 1

Granulometric composition of the studied materials

No.	*Name*	*Residue on sieve (mm), %*							
		> 10	*10-2.5*	*2.5-1*	*< 1*	*1-0.5*	*0.5-0.25*	*0.25-0.16*	*< 0.16*
I	Mixture of clay shale	41.4	35.8	12.3	10.5	-	-	-	-
II	Mixture of stones and sand	2.0	48.7	44.1	5.2	-	-	-	-
III	River silt	-	-	-	> 1 8.15	7.53	7.0	10.18	67.15

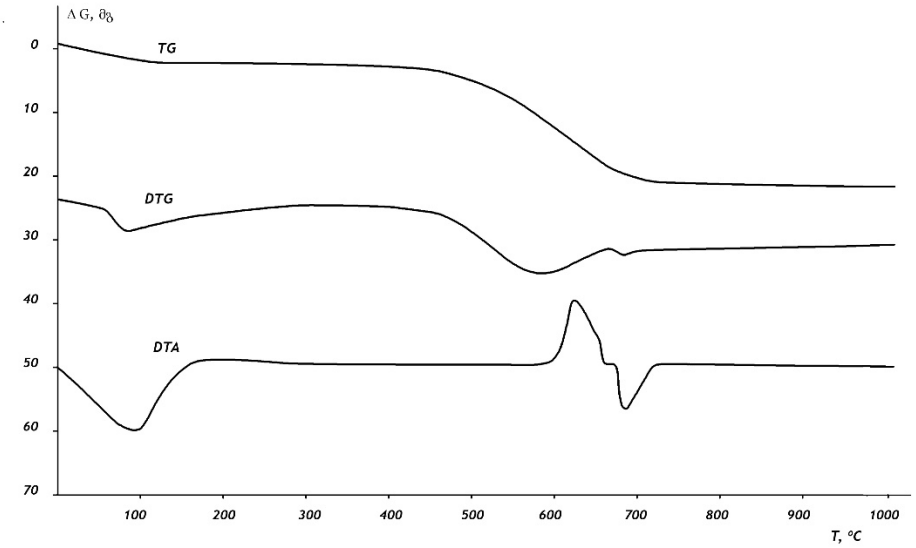

Fig. 1. DTA of clay shales.

Table 2

Chemical composition of the studied materials, wt.%

No.	*Name*	*LOI*	*Humidity*	SiO_2	TiO_2	Al_2O_3	$Fe_2O_3 + FeO$	P_2O_5	MnO	CaO	MgO	SO_3	Na_2O	K_2O	C	*Humus*
I	Mixture of clay shale	4.5	0.68	59.0	0.89	18.8	6.51	0.23	0.23	1.52	1.75	0.23	2.1	3.0	1.74	3.0
I	Mixture of clay shale (< 1 fraction)	6.43	2.97	53.8	0.82	17.2	7.39	0.32	0.32	2.74	1.81	0.73	2.2	3.0	2.94	5.07
II	Mixture of stones and sand	5.0	0.44	56.6	0.8	18,2	7.0	0.24	0.16	3.0	-	5 general 0.3	2.0	2.8	-	1.0
III	River silt	5.2	0.2	60.16	0.89	18.0	6.53	0.25	0.25	0.55	1.5	0.34	1.56	3.0	2.88	4.97

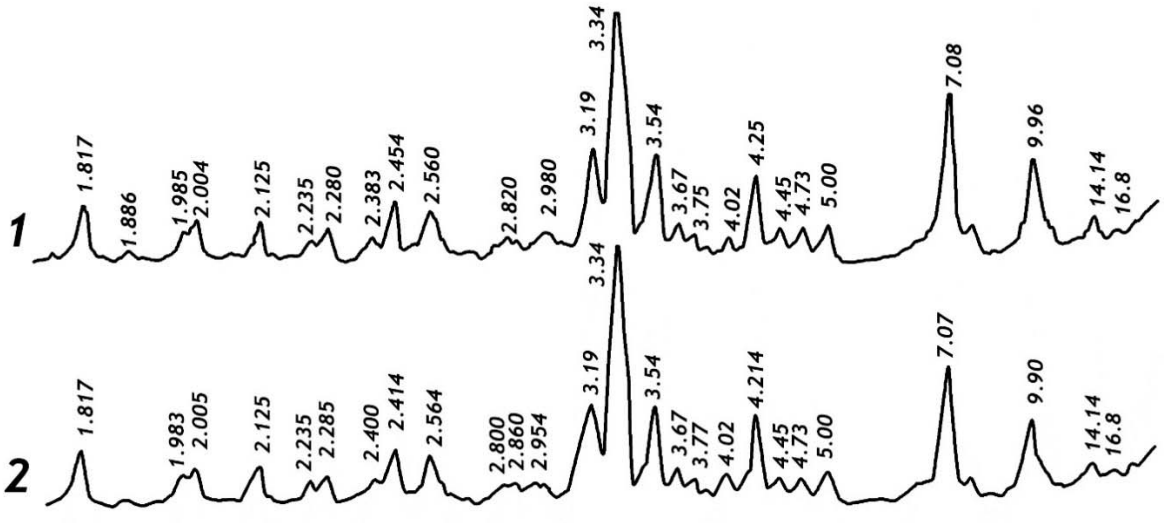

Fig. 2. Radiographs of clay shales: 1 – type I and 2 – type III

Thus, the mineralogical composition has confirmed the presence of iron hydroxides and carbonates, carbon, organic and quartz minor impurities in the shales, which, according to [5], create the necessary basis for the formation of a pyroplastic melt during swelling.

Three types of clay shales were found to have different swelling tendencies when heat-treated in a laboratory furnace at temperatures ranging from 1250°C to 1330°C. The samples showed different swelling characteristics, ranging from large pores to smaller, isolated pores. This process was quite different in river silt-based samples, which were characterized by a uniform, fine-pored structure.

After heat treatment, all samples are characterized by a high temperature of the pyroplastic state and a narrow range of swelling (~30 °C), but in this range they retain their shape, which gives reason to assume that the samples can be processed without the use of special refractory forms.

A similar result was obtained when processing samples obtained by averaging all three types of shale processed at a temperature of 1230°C – 1280°C. The samples were characterized by the simultaneous content of unevenly distributed large and small pores.

During heat treatment, due to the presence of viscosity gradients in the volume of the samples and non-uniform swelling processes in different areas and with different intensities, this led to the formation of a non-uniform structural structure of the samples.

To eliminate this drawback, in order to ensure normal technological and operational parameters, the method of unification of clay shales by correcting its chemical composition with rocks containing gas-forming substances was tested. These additives dissociate when processed at high temperature and contribute to the transition to a pyroplastic state at a relatively low temperature. At the same time, they create an additional source for the formation of gases and swelling of the material.

The experiments were successful both to improve the structure of the expanded material and

to reduce the temperature of the pyroplastic state. The optimal swelling temperature of the adjusted formulations decreased to the range of 1200°C - 1240°C. The swelling process was adjusted and a uniform volumetric distribution of the same size and isolated pores became possible.

3. CONCLUSION

Thus, the conducted research confirms the possibility of obtaining porous thermal insulation materials based on clay shales from the Duruji Gorge when processing them in the high-temperature range without the addition of foaming agents and the use of refractory molds.

REFERENCES

1. L. Gabunia, I. Kamushadze, E. Shapakidze, I. Gejadze. Production of expanded materials using local rocks (in Georgian). Ceramics, Tbilisi. 2(15) 2011, p. 3-5.
2. L. Gabunia, E. Shapakidze, G. Magalashvili, I. Gejadze. Investigation of Duruji River valley clay-shales for their application in various sectors of national economy (in Georgian). Anniversary collection of works of CIMR. Tbilisi, 2009, p. 99-101.
3. R. Skhvitaridze, A. Sakandelidze. Clay shales of the southern slope of the Main Caucasus Range as a new raw material for the production of building materials (in Georgian). Proceedings of the State Technical University. Tbilisi, No.45 (458), 2005, p. 125-29.
4. N. Gabunia, Ts. Napetvaridze, L. Gabunia, I. Kamushadze. Lightweight thermal insulation materials based on local rocks (in Georgian). Proceedings of the State Technical University. Tbilisi, No.45 (458), 2005, p. 37-38.
5. A. D. Shuster, R. A. Rakhimova. Shale as a raw material for producing lightweight concrete aggregates (in Russian). Publishing House "Nauka", Moscow, 1974. P. 63.

უაკ 691.42

მდინარე დურუჯის ხეობის თიხური ფიქლების კვლევა მათგან ფორიანი თბოსაიზოლაციო მასალების მიღების მიზნით

ლ. გაბუნია, ი. ქამუშაძე, ე. შაფაქიძე, ი. გეჯაძე, თ. პეტრიაშვილი

ივანე ჯავახიშვილის სახელობის თბილისის სახელმწიფო უნივერსიტეტი, ალექსანდრე თვალჭრელიძის სახელობის მინერალური ნედლეულის კავკასიის ინსტიტუტი. საქართველო, 0186, თბილისი, მინდელის 11

E-MAIL: lamgabunia@gmail.com, elena.shapakidze@tsu.ge

რეზიუმე: ***მიზანი.*** სამუშაოს მიზანია მდინარე დურუჯის ხეობის თიხური ფიქლების კვლევა მათგან ფორიანი თბოსაიზოლაციო მასალების მიღების მიზნით.

მეთოდი. გამოყენებულ იქნა ქიმიური და პეტროგრაფიული ანალიზის მეთოდები.

რენტგენოფაზური ანალიზისთვის გამოყენებულ იქნა დიფრაქტომეტრი Дрон-4.0, НПП "Буревестник", სპილენძის ანოდით და ნიკელის ფილტრით. U (ძაბვა)-35kv. I (დენის ძალა) - 20mA. გადაღების სიჩქარე - 2 გრად/წთ. λ = 1.54778 Å.

თერმოგრავიმეტრული ანალიზები ჩატარდა NETZSCH დერივატოგრაფზე, STA-2500 REGULUS ანალიზატორის (TG/DTA) გამოყენებით. ნიმუშების გახურება 1000°C კერამიკულ ტიგელებში, გახურების სიჩქარე 10 C/წუთი. ეტალონი - a-Al_2O_3.

შედეგი. ლაბორატორიულ პირობებში შესწავლილ იქნა სამი სხვადასხვა სახის თიხური ფიქალი. ჩატარებულ იქნა მათი გრანულომეტრული, რენტგენოფაზური და დიფერენციალურ-თერმული ანალიზები. ნიმუშების თერმული დამუშავების დროს ლაბორატორიულ ელექტრო-ღუმელში გამოვლინდა თიხური ფიქლების აფუების უნარი 1280–1300°C ტემპერატურულ ინტერვალში. ნიმუშები ხასიათდებოდა ფოროვანი სტრუქტურით მოცულობაში, მაგრამ არაერთგვაროვანი ზომის და არათანაბრად განაწილებული.

ტექნოლოგიური პარამეტრების გაუმჯობესების და აფუების ინტერვალის გაზრდის მიზნით, შემდგომ კვლევებში ჩატარდა თიხური ფიქლების შემადგენლობის უნიფიცირება ქიმიური დანამატების საშუალებით. მაკორექტირებელ დანამატად გამოყენებულ იქნა ბუნებრივი ქანები, რომლებიც აირწარმომქმნელ კომპონენტებს შეიცავდნენ.

ფიქლების კორექტირებამ დადებითი შედეგი გამოიღო მასალების თვისებებზე - დაიწია პიროპლასტიკურ მგომარეობაში გადასვლის ტემპერატურამ და გაუმჯობესდა მასალის ფოროვანი სტრუქტურა.

კვლევის შედეგად, შედარებით დაბალ ტემპერატურებზე, მიღებულ იქნა მაკორექტირებელი დანამატებით კორექტირებული თიხური ფიქლების კომპოზიციები ერთგვაროვანი ფოროვანი სტრუქტურით

დასკვნა: კვლევების შედეგად დადასტურდა ფორიანი თბოსაიზოლაციო მასალების მიღების შესაძლებლობა მდინარე დურუჯის თიხური ფიქლების საფუძველზე მათი დამუშავების შედეგად მაღალტემპერატურულ დიაპაზონში და ქაფწარმომქმნელი აგენტის და სპეციალური ცეცხლგამძლე ფორმების გამოყენების გარეშე.

საკვანძო სიტყვები: მდინარე დურუჯის ხეობის თიხური ფიქლები, აფუება, თერმული დამუშავება, ფორიანი თბოსაიზოლაციო მასალა.

UDC 546.284.636.7

CALCULATION OF STANDARD MOLAR THERMODYNAMIC PARAMETERS OF ANHYDROUS FRAMEWORK SILICATES

Vl. Gordeladze[1], T. Loladze[2]

[1]Faculty of Agricultural Sciences and Chemical Technology, Georgian Technical University, Tbilisi, Georgia
[2]Faculty of Transport Systems and Mechanical Engineering, Georgian Technical University, Tbilisi, Georgia

E-mail: v.gordeladze@gtu.ge

Resume: Objective: To calculate the standard molar values of thermodynamic parameters of anhydrous framework silicates using the method of additivity of structural constituents.

Method: The proposed approach enables the determination of thermodynamic parameters both for individual minerals and for compounds obtained through their combinations.

Results: The study examines, in a systematic manner, feldspars, the nepheline group, alkali feldspars, feldspathoids, and plagioclases. In implementing the method of additivity of structural constituents, specific minerals have been selected to serve as reference standards.

Conclusion: In the cases of Na□O·Al□O□·6SiO□ and K□O·Al□O□·6SiO□, the observed differences in thermodynamic parameter values arise from the fact that solid solutions formed with alkali compounds incorporate monoclinic varieties of feldspars, namely, adularia and barbierite. In contrast, in the albite–microcline system, the components, forming solid solutions, are triclinic varieties, which is reflected in their energetic parameters. Deviations from reference standards for $\Delta\mathbf{H}^{\mathbf{o}}_{\mathbf{f},\mathbf{298}}$ range from 0.20 to 0.52%, and for $\Delta\mathbf{G}^{\mathbf{o}}_{\mathbf{f},\mathbf{298}}$ - from 0.1 to 0.4%. For $\mathbf{S}^{\mathbf{o}}_{\mathbf{298}}$ and $\mathbf{C}_{\mathbf{p},\mathbf{298}}$, the deviations are 0.24–1.99 and 0.07–1.73 entropy units, respectively.

Key words: silicate, framework, structural constituent, thermodynamic parameter, feldspar, alkali feldspar, feldspathoid, plagioclase, nepheline.

1. INTRODUCTION

In the recent past, empirical approaches based on numerous experiments dominated the development of new materials and compounds. This, in turn, led to unjustified expenditures of materials, energy, time, and labor, particularly in the context of critical technological decisions. The impact of high temperatures in certain systems further exacerbates this issue. In such cases, thermodynamic analysis offers a more realistic means of evaluating the nature of chemical interactions.

With the rapid expansion of the range of chemical compounds used across various fields of emerging technologies, experimental determination of their properties cannot keep pace with the ever-growing demand for new data. This necessitates the use of alternative methods for estimating the thermodynamic properties of certain substances. One such approach, a method for calculating thermodynamic properties, is discussed in the present study. Using this method, the standard molar thermodynamic parameters of anhydrous framework silicates have been determined.

2. MAIN PART

The subclass of anhydrous framework silicates is conventionally divided into three groups:

1. The silicon group, encompassing all its forms-quartz, tridymite, and cristobalite;

2. The feldspar group, including $K_2O{\cdot}Al_2O_3{\cdot}6SiO_2$ varieties, consisting of plagioclase-series minerals whose end-members are albite and anorthite;

3. The feldspathoid group, including leucite, nepheline, and kalsilite.

SiO_2 exhibits multiple crystalline phases, among which quartz is the natural modification and, in most cases, is treated as a structural constituent. Structurally, quartz is divided into two modifications: low-temperature (β-quartz) and high-temperature (α-quartz); however, the differences between these structures are minor.

The low-temperature phase of $K_2O{\cdot}Al_2O_3{\cdot}6SiO_2$ is represented by the mineral microcline (Mcl), which is used as a reference standard in this study. Additionally, the plagioclase-series end-members, albite (Ab) and anorthite (An), are used as reference standards. Both minerals crystallize in the low-temperature range as triclinic compounds, similar to microcline.

From the third group of framework silicates, three minerals are also employed as reference standards: leucite (Lc, $K_2O{\cdot}Al_2O_3{\cdot}4SiO_2$), kalsilite (Kf, $K_2O{\cdot}Al_2O_3{\cdot}2SiO_2$), and nepheline (Ne, $Na_2O{\cdot}Al_2O_3{\cdot}2SiO_2$). Among these, leucite crystallizes in the tetragonal system at low temperatures, while the other two crystallize in the hexagonal system.

Analysis of the structural differences of the above compounds leads to the conclusion that no unified approach exists for all of them. However, most researchers agree that structural differences between orthoclase (all varieties of $K_2O{\cdot}Al_2O_3{\cdot}6SiO_2$) and plagioclases are primarily due to the non-rigidity of the silicon–oxygen framework containing substituted aluminum ions. This framework can expand when large cations (K, Ba) enter its cavities and contract around smaller cations (Na, Ca).

Regarding feldspathoids, sources note that they never appear in direct association with quartz. This is explained by their high reactivity, rapidly forming feldspars upon interaction with free silicon, especially at high temperatures.

To implement the proposed method of additivity of structural constituents (developed by Prof. A. Sarukhanishvili, Georgian Technical University), accurate information on the standard molar thermodynamic parameters of framework compounds is required. Based on five sources [2–6], these values are summarized in Table 1, which shows significant variations in some compounds [1]. This variability, inherent to the additivity method, complicates the selection of a particular compound as a standard. The accepted limits for deviations in thermodynamic parameters are: ≤3% for ΔH^{O}_{298} and ΔG^{O}_{298}, and up to three entropy units for $S°_{298}$ and $C_{p,298}$.

For example, Table 2 presents $\Delta H°_{298}$ and $S°_{298}$ values for six widely studied minerals (Ab, An, Mcl, Lc, Kf, Ne) [1]. Based on these data, using three sources instead of five is considered more reasonable for the additivity calculations, although discrepancies between thermodynamic values still remain, potentially affecting calculation accuracy. For instance, for nepheline, $\Delta H°_{f,298}$=–1008.04 kcal/mol and $\Delta G°_{f,298}$=–953.20 kcal/mol [5], which differ significantly from values reported in [2] and [3].

Before applying the additivity method, it was necessary to adopt an approach for classifying feldspars and feldspathoids based on their specific characteristics. The complex nature of feldspar minerals requires their division into numerous varieties, differing chemically, physically, and structurally. Without undermining contributions of other researchers, the classification and nomenclature proposed by Deer, Howie, and Zussman [8] was adopted. This choice is justified as the additivity method applies not only to individual minerals but also to compounds formed from their combinations.

Accordingly, feldspars are subdivided into:

- **Alkali feldspars (Fsp):** general formula $Na_2O(K_2O)\cdot Al_2O_3\cdot 6SiO_2$;
- **Plagioclases (Pla):** feldspars of the $Na_2O\cdot Al_2O_3\cdot 6SiO_2$–$CaO\cdot Al_2O_3\cdot 2SiO_2$ system.

Within the first subgroup, "pure" $Na_2O\cdot Al_2O_3\cdot 6SiO_2$ (barbierite) and $K_2O\cdot Al_2O_3\cdot 6SiO_2$ (adularia) are isostructural at low temperatures (monoclinic system). Similarly, "pure" $Na_2O\cdot Al_2O_3\cdot 6SiO_2$ (albite) and $Ca_2O\cdot Al_2O_3\cdot 2SiO_2$ (anorthite) are also isostructural but crystallize in the triclinic system.

Feldspathoids are treated separately as the nepheline group, including nepheline ($Na_2O\cdot Al_2O_3\cdot 6SiO_2$), kalsilite ($K_2O\cdot Al_2O_3\cdot 2SiO_2$), and leucite ($K_2O\cdot Al_2O_3\cdot 4SiO_2$) [8]. Nepheline and kalsilite are not isostructural, but both have structures based on a tridymite-like framework, where approximately half of the silicon atoms are substituted by aluminum.

Using the available data on feldspars and feldspathoids, the **additivity method of structural constituents** was applied to calculate standard molar thermodynamic parameters, with results presented in Tables 3 and 4. Calculations based on subdividing framework minerals into feldspars and feldspathoids are shown in Tables 5–7 [1]. It should be noted that the same mineral can exhibit different thermodynamic parameter values depending on the group it belongs to. For example, $Na_2O\cdot Al_2O_3\cdot 6SiO_2$ in the alkali feldspar group has $\Delta H°_{f,298}$ = –1883.23 kcal/mol, in the plagioclase group –1873.92 kcal/mol, and generalized –1878.21 kcal/mol. These differences are shown in Table 8.

Legend for tables:

- **A:** standard molar thermodynamic property of the reference;
- **A′:** standard molar thermodynamic property of a substance calculated as the sum of corresponding structural constituent properties;
- **B:** standard molar thermodynamic property obtained by multiplying A′ by the leveling coefficient (B = K□·A′);
- **K□:** ratio coefficient, A/A′;
- **K□:** leveling coefficient, equal to ∑K□/n, where n is the number of structural constituents;
- **SMTP:** standard molar thermodynamic properties;
- **SI:** structural constituents forming a specific compound with zero, lower, or higher silicate structural order relative to the compound;

Reference Et(A): substance with the most reliable standard molar thermodynamic properties from databases, or their average values. In cases of inconsistency, deviations do not exceed defined limits.

Table 1. Comparison of Standard Molar Thermodynamic Parameters According to Five Sources

Compound	Thermodynamic Parameters [2]				Thermodynamic Parameters [4/3]				Thermodynamic Parameters [5/6]			
	$-H^{O}_{298}$ kcal/mol	$-G^{O}_{298}$ kcal/mol	S^{O}_{298} cal/(mol·K)	$C_{P,298}$ cal/(mol·K)	$-H^{O}_{298}$ kcal/mol	$-G^{O}_{298}$ kcal/mol	S^{O}_{298} cal/(mol·K)	$C_{P,298}$ cal/(mol·K)	$-H^{O}_{298}$ kcal/mol	$-G^{O}_{298}$ kcal/mol	S^{O}_{298} cal/(mol·K)	$C_{P,298}$ cal/(mol·K)
Anorthite, (An)	1010.49	956.60	47.63	50.31	1013.33	959.40	48.60	49.51	1008.1	954.4	48.40	49.47
					1014.20	960.27	49.63	50.53	1008.1	954.3	48.40	49.47
Gelenite, (Gel)	951.60	604.21	50.19	49.06	957.10	909.60	50.10	-	951.7	903.4	47.40	49.10
					957.90	910.40	50.14	49.33	951.7	903.4	47.40	58.08
Monticellite, (Mon)	540.89	512.92	26.41	29.45	540.88	-	-	-	540.94	512.77	25.9	29.63
					540.88	512.78	25.9	-	540.94	512.77	25.9	29.63
Diopside, (Di)	766.30	724.69	34.16	40.75	766.29	724.67	34.20	40.50	765.80	724.1	34.20	37.56
					765.46	723.84	34.16	39.87	766.30	724.60	34.20	37.50
Ackermanite, (Ak)	926.67	879.53	50.00	50.59	926.69	879.50	-	-	924.5	877.30	50.00	50.59
					926.66	879.49	50.00	50.65	926.70	884.5	50.00	52.61
Merwinite, (Mer)	1091.41	1037.40	60.49	60.17	1091.67	1037.34	60.50	-	1087.7	1033.5	60.50	60.25
					1091.64	1037.33	60.50	60.29	1094.90	1037.52	60.50	-
Calliophyllite, (Kf)	1014.01	958.60	63.62	57.33	1013.40	952.00	63.60	-	997.8	942.80	63.60	58.31
					1013.64	958.22	63.60	57.26	1020.10	978.90	63.70	-
Leucite, (Lc)	1450.38	1372.61	95.6	78.44	1450.49	1373.60	95.6	-	1442.0	1362.00	88.20	79.36
					1452.28	1374.50	95.9	78.46	1455.40	1364.40	88.00	-
Cordierite, (Cor)	2189.70	2067.81	97.30	108.17	2177,90	2055.00	97.30	-	2192.90	2071.0	97.30	108.17
					2188,90	2066.97	97.30	108.10	-	-	97.30	-
Pyrope, (Pir)	1502.06	1417.88	62.32	77.84	1484.87	-	-	-	1512.1	1428.8	65.0	51.23
					1502.50	1417.76	60.30	76.60	-	1438.35	-	-
Nepheline, (Ne)	1000.38	945.60	59.42	55.36	1008.00	953.20	59.20	-	991.20	938.4	59.40	52.46
					1000.44	945.61	59.20	56.44	981.80	926.8	59.40	55.36
Jadeite, (Jad)	1448.80	1363.38	63.81	76.48	1439.40	1354.04	63.60	76.42	1438.6	1353.0	63.80	91.19
					-	-	63.80	-	1420.00	1340.60	63.80	-
Albite, (Ab)	1876.58	1772.56	108.13	97.94	1874.40	1772.80	99.0	94.61	1873.00	1766.6	100.4	97.94
					1822.22	1776.10	99.14	98.04	1880.44	1773.40	100.4	-

Table 2. Comparison of Standard Molar Thermodynamic Parameters of Feldspars and Feldspathoids According to Five [4–8] and Three [4,5,7] Sources

Symbol and Formula	According to Five Sources				According to Three Sources			
	$-\Delta H^{o}_{f,298}$ kcal/mol		S^{o}_{298} cal/(mol·K)		$-\Delta H^{o}_{f,298}$ kcal/mol		S^{o}_{298} cal/(mol·K)	
	Limits of Variation	Average Value	Limits of Variation	Average Value	Limits of Variation	Average Value	Limits of Variation	Average Value
Ab, $Na_2O{\cdot}Al_2O_3{\cdot}6SiO_2$	1873.10-1882.82	1877.45	99.0- 98.04	99.09	1879.60-1882.22	1880.95	99.03-99.4	99.09
An, $CaO{\cdot}Al_2O_3{\cdot}2SiO_2$	1008.06-1014.20	1010.84	47.6- 48.4	47.82	1010.49-1014.20	1012.67	47.60-47.63	47.62
*Mc*l, $K_2O{\cdot}Al_2O_3{\cdot}6SiO_2$	1888.40-1901.60	1894.64	102.56-105.00	103.00	1901.62-1895.20	1897.87	102.25-102.4	102.33
Lc, $K_2O{\cdot}A_2O_3{\cdot}4SiO_2$	1442.04-1452.28	1450.11	88.0- 95.6	92.60	1450.38-1452.28	1451.05	95.6	9.56
Kr, $K_2O{\cdot}Al_2O_3{\cdot}2SiO_2$	997.20-1014.01	1011.79	63,6- 63,8	63.66	1013.40-1014.01	1013.68	63.62-63.60	63.37
Ne, $Na_2O{\cdot}Al_2O_3{\cdot}2SiO_2$	981.80-1008.04	996.36	59.20- 59.42	59.31	1000.38-1008.0	1002.94	59.20-59.47	59.27

Table 3. Calculation of Thermodynamic Parameters of Framework Silicates (Alkali Feldspars)

Symbol, Compound Formula	SMTP, Etalon (A)	Formula and SMTP, SI			$K_i=A/A'$	$K_n=\Sigma K_i/n$	$B=K_n \cdot A$	Deviation	
		Formula	SMTP, SI	Σ SMTP, (A')				Δ=A-B	%
Calculation of $\Delta H^{o}_{f,298}$, kcal/mol									
Ab, $Na_2O \cdot Al_2O_3 \cdot 6SiO_2$	-1879.38	$Na_2O \cdot 3SiO_2$ Al_2O_3 $3SiO_2$	-809,65 -400,46 -653,19	-1863.40	1.0086	1.0107	-1883.23	3.85	0.20
Mcl, $K_2O \cdot Al_2O_3 \cdot 6SiO_2$	-1894.64	$K_2O \cdot 4SiO_2$ Al_2O_3 $2SiO_2$	-1035.00 -400,46 -435,46	-1870.92	1.0127		-1890.93	-3.71	0.20
Calculation of $\Delta G^{o}_{f,298}$, kcal/mol									
Ab, $Na_2O \cdot Al_2O_3 \cdot 6SiO_2$	-1772.62	$Na_2O \cdot 3SiO_2$ Al_2O_3 $3SiO_2$	-766,05 -377,46 -614,25	-1757,76	1.0085	1.0106	-1776,39	3.77	0.21
Mcl, $K_2O \cdot Al_2O_3 \cdot 6SiO_2$	-1787,51	$K_2O \cdot 4SiO_2$ Al_2O_3 $2SiO_2$	-978,22 -377,46 -409,50	-1765.18	1.0127		-1783.89	3.63	0.20
Calculation of S^{o}_{298}, cal/mol·K									
Ab, $Na_2O \cdot Al_2O_3 \cdot 6SiO_2$	99.09	$Na_2O \cdot Al_2O_3$ 6SiO2	35.80 60.00	96.80	1.0237	1.0187	98.61	0.48	0.49
Mcl, $K_2O \cdot Al_2O_3 \cdot 6SiO_2$	102.27	$K_2O \cdot Al_2O_3$ $6SiO_2$	40.90 60.00	100.90	1.0136		102.79	-0,52	0.51
Calculation of $C_{P,298}$, cal/mol·K									
Ab, $Na_2O \cdot Al_2O_3 \cdot 6SiO_2$	97.31	$Na_2O \cdot Al_2O_3$ $6SiO_2$	33.80 63.84	97.64	0.9966	0.9840	96.08	1.23	1.27
Mcl, $K_2O \cdot Al_2O_3 \cdot 6SiO_2$	97.35	$K_2O \cdot Al_2O_3$ $6SiO_2$	36.38 63.84	100.22	0.9714		98.62	-1.26	1.28

Table 4. Calculation of Thermodynamic Parameters of Framework Silicates (Plagioclases)

Symbol, Compound Formula	SMTP, Etalon (A)	Formula and SMTP, SI			$K_t=A/A'$	$K_n=\Sigma K_t/n$	$B= K_n \cdot A$	Deviation	
		Formula	SMTP, SI	Σ SMTP, (A′)				Δ=A-B	%
Calculation of $\Delta H^{o}_{f,298}$, kcal/mol									
Ab, $Na_2O \cdot Al_2O_3 \cdot 6SiO_2$	-1879.38	$Na_2O \cdot 3SiO_2$ Al_2O_3 $3SiO_2$	-809,65 -400,46 -653,19	-1863.30	1.0086	1.0057	-1873.92	-5,46	0.29
An, $CaO \cdot Al_2O_3 \cdot 2SiO_2$	-1011,29	$CaO \cdot SiO_2$ Al_2O_3 SiO_2	-390,27 -400,46 -217,73	-1008,46	1.0028		-1014.21	2.92	0.29
Calculation of $\Delta G^{o}_{f,298}$, kcal/mol									
Ab, $Na_2O \cdot Al_2O_3 \cdot 6SiO_2$	-1772.62	$Na_2O \cdot 3SiO_2$ Al_2O_3 $3SiO_2$	-766,05 -377,46 -614,25	-1757,76	1.0085	1.0083	-1770,59	-2.03	0.11
An, $CaO \cdot Al_2O_3 \cdot 2SiO_2$	957.67	$CaO \cdot SiO_2$ Al_2O_3 SiO_2	-370.01 -377.01 -204,75	-951,97	1.0060		-958,92	1.23	0.13
Calculation of S^{o}_{298} , cal/mol·K									
Ab, $Na_2O \cdot Al_2O_3 \cdot 6SiO_2$	99.09	$Na_2O \cdot Al_2O_3$ $6\ SiO_2$ _	36.80 60.00	96.80	1.0237	1.0185	98.59	0.50	0.50
An, $CaO \cdot Al_2O_3 \cdot 2SiO_2$	47.93	$CaO \cdot Al_2O_3$ $2SiO_2$ _	27.30 20.00	47.30	1.0133		48.18	-0.24	0.50
Calculation of $C_{P,298}$, cal/mol·K									
Ab, $Na_2O \cdot Al_2O_3 \cdot 6SiO_2$	97.31	$Na_2O \cdot Al_2O_3$ $6\ SiO_2$ _	33.80 63.84	97.64	0.9966	0.9973	97.38	-0,07	0.07
An, $CaO \cdot Al_2O_3 \cdot 2SiO_2$	49.96	$CaO \cdot Al_2O_3$ $2SiO_2$ _	28.78 21.28	50.06	0.9980		49.85	0.14	0.08

Table 5. Calculation of Thermodynamic Parameters of Framework Silicates (Nepheline Group)

Symbol, Compound Formula	SMTP, Etalon (A)	Formula and SMTP, SI			$K_i=A/A'$	$K_n=\Sigma K_i/n$	$B= K_n \cdot A$	Deviation	
		Formula	SMTP, SI	Σ SMTP, (A′)				Δ=A-B	%
Calculation of $\Delta H^{o}_{f,298}$, kcal/mol									
Kf, $K_2O \cdot Al_2O_3 \cdot 2SiO_2$	-1013,68	$K_2O \cdot 2SiO_2$ Al_2O_3	-597,27 -400,46	-997,73	1.0159	1.0139	-1011,60	-2.08	0.21
Ne, $Na_2O \cdot Al_2O_3 \cdot 2SiO_2$	-1002,94	$Na_2O \cdot 2SiO_2$ Al_2O_3	-590,81 -400,46	-991,27	1.0118		-1005.05	2.11	0.21
Calculation of $\Delta G^{o}_{f,298}$, kcal/mol									
Kf, $K_2O \cdot Al_2O_3 \cdot 2SiO_2$	-958,41	$K_2O \cdot 2SiO_2$ Al_2O_3	-562,30 -377,46	-939,76	1.0198	1.0173	-9563.02	-2.39	0.25
Ne, $Na_2O \cdot Al_2O_3 \cdot 2SiO_2$	-948.14	$Na_2O \cdot 2SiO_2$ Al_2O_3	-556,94 -377,46	-934,40	1.0147		-950,57	2.43	0.26
Calculation of S^{O}_{298} , cal/mol·K									
Kf, $K_2O \cdot Al_2O_3 \cdot 2SiO_2$	63.47	$K_2O \cdot Al_2O_3$ 2SiO2(tri)	40.90 20.80	61.70	1.0267	1.0574	65.24	-1,77	2.79
Ne, $Na_2O \cdot Al_2O_3 \cdot 2SiO_2$	59.41	$Na_2OAl_2O_3$ $2SiO_2$(tri)	33.80 20.80	54.60	1.0881		57.73	1.68	2.83
Calculation of $C_{P,298}$, cal/mol·K									
Kf, $K_2O \cdot Al_2O_3 \cdot 2SiO_2$	57.30	$K_2O \cdot 2SiO_2$ Al_2O_3	40.07 18.82	58.89	0.9730	0.9833	57.91	-0,61	1.06
Ne, $Na_2O \cdot Al_2O_3 \cdot 2SiO_2$	55.90	$Na_2O \cdot 2SiO_2$ Al_2O	37.44 18.82	56.26	0.9936		55.32	0.58	1.04

Table 6. Calculation of Thermodynamic Parameters of Framework Silicates (Feldspathoids)

Symbol, Compound Formula	SMTP, Etalon (A)	Formula and SMTP, SI			$K_t=A/A'$	$K_n=\Sigma K_t/n$	$B= K_n \cdot A$	Deviation	
		Formula	SMTP, SI	Σ SMTP, (A′)				Δ=A-B	%
Calculation of $\Delta H^{o}_{f,298}$, kcal/mol									
Ne, $Na_2O \cdot Al_2O_3 \cdot 2SiO_2$	-1002,94	$Na_2O \cdot 2SiO_2$ Al_2O_3	-590.81 -400,46	-991,27	1.0118	1.0129	-1004.06	1.12	0.11
Kf, $K_2O \cdot Al_2O_3 \cdot 2SiO_2$	-1013,68	$K_2O \cdot 2SiO_2$ Al_2O_3	-597,27 -400,46	-997,73	1.0159		-1010,60	-3.08	0.30
Lc, $K_2O \cdot Al_2O_3 \cdot 4SiO_2$	-1451.05	$K_2O \cdot 4SiO_2$ Al_2O_3	-1035.00 -400,46	-1435,46	1.0109		-1453,98	2.93	0.20
Calculation of $\Delta G^{o}_{f,298}$, kcal/mol									
Ne, $Na_2O \cdot Al_2O_3 \cdot 2SiO_2$	-948.14	$Na_2O \cdot 2SiO_2$ Al_2O_3 _	-556,94 -377,46	-934,40	1.0147	1.0157	-949.07	0.93	0.10
Kf, $K_2O \cdot Al_2O_3 \cdot 2SiO_2$	-958,41	$K_2O \cdot 2SiO_2$ Al_2O_3	-562,30 -377,46	-939,76	1.0198		-954,51	-3,90	0.41
Lc, $K_2O \cdot Al_2O_3 \cdot 4SiO_2$	-1373,57	$K_2O \cdot 4SiO_2$ Al_2O_3	-978,22 -377,46	-1356,28	1.0127		-1377,57	4.00	0.29
Calculation of S^{o}_{298} , cal/mol·K									
Ne, $Na_2O \cdot Al_2O_3 \cdot 2SiO_2$	59.41	$Na_2O \cdot Al_2O_3$ $2SiO_2$(tri)	33 , 80 20.80	54.60	1.0881	1.0609	57.93	1.48	2.49
Kf, $K_2O \cdot Al_2O_3 \cdot 2SiO_2$	63.47	$K_2O \cdot Al_2O_3$ $2SiO_2$(tri)	40.90 20.80	61.70	1.0267		65.46	-1,99	3.14
Lc, $K_2O \cdot Al_2O_3 \cdot 4SiO_2$	88.1*	$K_2O \cdot Al_2O_3$ $4SiO_2$(tri)	40.90 41.60	82.50	1.0679		87.52	0.58	0.66
Calculation of $C_{P,298}$, cal/mol·K									
Ne, $Na_2O \cdot Al_2O_3 \cdot 2SiO_2$	55.90	$Na_2O \cdot Al_2O_3$ $2SiO_2$(tri)	37.44 18.44	56.26	0.9936	0.9865	55.50	0.40	0.71
Kf, $K_2O \cdot Al_2O_3 \cdot 2SiO_2$	57.30	$K_2O \cdot Al_2O_3$ $2SiO_2$(tri)	40.07 18.82	58.89	0.9730		58.09	-0,79	1.38
Lc, $K_2O \cdot Al_2O_3 \cdot 4SiO_2$	78.45	$K_2O \cdot Al_2O_3$ $4SiO_2$(tri)	36.38 42.64	79.02	0.9928		76.97	1.48	1.89

* – The value is taken as the average of the data provided in [4] and [6]

Table 7. Calculation of Thermodynamic Parameters of Framework Silicates (Feldspars)

Symbol, Compound Formula	SMTP, Etalon (A)	Formula and SMTP, SI			$K_i=A/A'$	$K_n=\Sigma K_i/n$	$B= K_n \cdot A$	Deviation	
		Formula	SMTP, SI	Σ SMTP, (A')				Δ=A-B	%
Calculation of $\Delta H^{o}_{f,298}$, kcal/mol									
Ab, $Na_2O \cdot Al_2O_3\ 6SiO_2$	-1879.38	$Na_2O \cdot 3SiO_2$ Al_2O_3 $3Si0_2$	-809,65 -400,46 -653,19	-1863.30	1.0086	1.0080	-1878.21	-1.17	-0,06
An, $CaO \cdot Al_2O_3 \cdot 2SiO_2$	-1011,29	$CaO \cdot SiO_2$ Al_2O_3 SiO2	-390,27 -400,46 -217,73	-1008,46	1.0028		-1016,53	5.24	0.52
Mcl, $K_2O \cdot Al_2O_3 \cdot 6SiO_2$	-1894.64	$K_2O \cdot 3SiO_2$ Al_2O_3 $3SiO_2$	-1035.00 -400,46 -435,46	-1870.92	1.0127		-1885.88	-8,75	-0,46
Calculation of $\Delta G^{o}_{f,298}$, kcal/mol									
Ab, $Na_2O \cdot Al_2O_3\ 6SiO_2$	-1772.62	$Na_2O \cdot 3SiO_2$ Al_2O_3 $3Si0_2$	-766,05 -377.01 -614,25	-1757,76	1.0085	1.0093	-1774.11	1.49	0.08
An, $CaO \cdot Al_2O_3 \cdot 2SiO_2$	-957,67	$CaO \cdot SiO_2$ Al_2O_3 SiO2	-370.01 -377.01 204.75	-951,97	1.0060		-960,82	3.15	0.32
Mcl, $K_2O \cdot Al_2O_3 \cdot 6SiO_2$	-1788.74	$K_2O \cdot 3SiO_2$ Al_2O_3 $3SiO_2$	-978,22 -377.01 -409,50	-1765.18	1.0138		-1781,60	-7.14	-0,40
Calculation of S^{o}_{298} , cal/mol·K									
Ab, $Na_2O \cdot Al_2O_3\ 6SiO_2$	99.09	$Na_20 \cdot Al_2O_3$ $6SiO_2$	36.80 60.00	96.80	1.0237	1.0161	98.36	0.73	0.74
An, $CaO \cdot Al_2O_3 \cdot 2SiO_2$	47.82	$Ca0 \cdot Al_2O_3$ $2SiO_2$	27.30 20.00	47.30	1.0110		48.06	-0.24	-0,50
Mcl, $K_2O \cdot Al_2O_3 \cdot 6SiO_2$	102.27	$K_20 \cdot Al_2O_3$ $6SiO_2$	40.90 60.00	100.90	1.0136		102.52	-0,25	-0.24
Calculation of $C_{P,298}$, cal/mol·K									
Ab, $Na_2O \cdot Al_2O_3\ 6SiO_2$	97.31	$Na_20 \cdot Al_2O_3$ $6SiO_2$	33.80 63.84	97.64	0.9966	0.9887	965.4	0.77	0.79
An, $CaO \cdot Al_2O_3 \cdot 2SiO_2$	49.96	$Ca0 \cdot Al_2O_3$ $2SiO_2$	28.78 21.28	50.06	0.9980		49.49	0.47	0.90
Mcl, $K_2O \cdot Al_2O_3 \cdot 6SiO_2$	97.35	$K_20 \cdot Al_2O_3$ $6SiO_2$	36.38 63.84	100.22	0.9714		99.08	-1,73	-1,79

Table 8. Dependence of Differences in Thermodynamic Parameter Values on the Specific Mineral Group

Compound Formula	SMTP (B), kcal/mol		SMTP (B), kcal/mol		Group Affiliation
	$-\Delta H^{o}_{f,298}$	$-\Delta G^{o}_{f,298}$	S^{o}_{298}	$C_{p,298}$	
$Na_2O{\cdot}Al_2O_3{\cdot}6SiO_2$	1883.23	1776.39	98.61	98.08	Alkali Fsp
	1873.92	1770.59	98.59	97.38	Plagioclases (Pla)
	1878.21	1774.11	98.39	96.54	Generalized Fsp
$K_2O{\cdot}Al_2O_3{\cdot}\ 6SiO_2$	1890.93	1783.89	102.79	98.62	Alkali Fsp
	1894.64	1788.74	102.52	99.08	Generalized Fsp
$CaO{\cdot}Al_2O_3{\cdot}2SiO_2$	1014.21	959.92	48.86	49.92	Plagioclases (Pla)
	1016.53	960.82	48.06	49.49	Generalized Fsp
$K_2O{\cdot}Al_2O_3{\cdot}2SiO_2$	1011.60	956.02	65.24	57.73	Nepheline
	1010.60	954.51	65.46	58.09	Generalized
$Na_2O{\cdot}Al_2O_3{\cdot}2SiO_2$	1005.05	950.57	57.73	55.32	Nepheline
	1004.06	949.07	57.93	55.50	Generalized
$K_2O{\cdot}Al_2O_3{\cdot}4SiO_2$	1451.11	1373.50	88.10	78.45	Individual
	1453.98	1377.57	87.52	76.97	Generalized

(B) – Thermodynamic parameters calculated using the additive method of structural ingredients

3. CONCLUSION

Using the proposed additive method of structural ingredients, the standard molar thermodynamic parameters of alkali feldspars, plagioclases, the nepheline group, feldspathoids, and feldspars have been calculated. The deviations from the reference minerals are, in the case of $\Delta H°_{f,298}$ - 0.20–0.52%, and for $\Delta G°_{f,298}$ - 0.1–0.4%. For $S°_{298}$ and $C°_{p,298}$, the deviations are 0.24 - 1.99 and 0.07 - 1.73 entropy units, respectively. These values are fully acceptable for the calculation of standard molar thermodynamic parameters of thermodynamically unknown anhydrous silicate minerals.

In the cases of $Na_2O{\cdot}Al_2O_3{\cdot}6SiO_2$ and $K_2O{\cdot}Al_2O_3{\cdot}6SiO_2$, the differences in thermodynamic parameter values arise from the fact that solid solutions formed with alkali compounds include the monoclinic modifications of feldspars, namely adularia and barbiturite, rather than microcline and albite. In contrast, in the albite–microcline system, the participants forming solid solutions are of triclinic modifications, which is reflected in the energetic parameters.

These circumstances appear to be responsible for the “scatter” observed in the standard molar thermodynamic parameters of feldspars. The differences between modifications are so small

that they cannot be determined experimentally; however, they are still energetically significant.

The same factors may also cause differences in the thermodynamic parameters of minerals in the nepheline group.

REFERENCES

1. Sarukhanishvili, A., Gordeladze, V., Eristavi, D., & Gogishvili, A. (2019). Method of additivity of structural constituents for determining the thermodynamic properties of anhydrous silicates. Tbilisi: Publishing House of Technical University, 216 p.
2. Yokokawa, H. (1983). Tables of Thermodynamic Properties of Inorganic Compounds. J. Nat. Chem. Lab. Ind., 83, 121 p.
3. Glushko, V.P. (Ed.). (1961–1981). Thermodynamic constants of substances. Moscow: AN SSSR, VINTI, Vols. I–X.
4. Bulakh, A.G. (1974). Methods of thermodynamics in mineralogy. Leningrad: Nedra, pp. 155–169.
5. Babushkin, V.N., Matveev, G. M., & Mchedlov-Petrosyan, O.P. (1986). Thermodynamics of silicates. Moscow: Stroyizdat, 406 p.
6. Karpov, I.E., Kashchik, S.A., & Pampura, V.D. (1968). Constants of substances for thermodynamic calculations in geochemistry and petrology. Moscow: Nauka, pp. 10–65.
7. Saxena, S.K., et al. (1993). Thermodynamic Data on Oxides and Silicates. New York/Berlin/ Heidelberg: Springer-Verlag, 428 p.
8. Deer, W.A., Howie, R.A., & Zussman, J. (1966). Rock-forming minerals (Vol. 4). Moscow: Mir, 288 p.

უაკ 546.284.636.7

უწყლო კარკასული სილიკატების თერმოდინამიკური პარამეტრების სტანდარტული მოლური მნიშვნელობების გაანგარიშება

ვლ. გორდელაძე, თ. ლოლაძე

1საქართველოს ტექნიკური უნივერსიტეტი. აგრარული მეცნიერებების და ქიმიური ტექნოლოგიის ფაკულტეტი. თბილისი, საქართველო

2ტრანსპორტის სისტემებისა და მექანიკის ინჟინერიის ფაკულტეტი. თბილისი, საქართველო

E-MAIL: v.gordeladze@gtu.ge

რეზიუმე: მიზანი. სტრუქტურული ინგრედიენტების ადიტიურობის მეთოდით, უწყლო კარკასული სილიკატების თერმოდინამიკური პარამეტრების სტანდარტული მოლური მნიშვნელობების გაანგარიშება.

მეთოდი. შემოთავაზებული მეთოდით შესაძლებელია როგორც ცალკეული მინერალების, ისე მათი კომბინაციით მიღებული ნაერთების თერმოდინამიკური პარამეტრების განსაზღვრა.

შედეგები. ჯგუფობრივად არის განხილული მინდვრის შპატები, ნეფელინის ჯგუფი, ტუტე ფელდშპატები, ფელდშპატიდები და პლაგიოკლაზები. სტრუქტურული ინგრედიენტების ადიტიურობის მეთოდის რეალიზებისას, ეტალონის სახით გამოსაყენებლად, მათთვის შერჩეულია მინერალები.

დასკვნა. $Na_2O{\cdot}Al_2O_3{\cdot}6SiO_2$-ის და $K_2O{\cdot}Al_2O_3{\cdot}6SiO_2$-ის შემთხვევაში თერმოდინამიკური პარა-მეტრების მნიშვნელობების განსხვავება გამოწვეულია იმ გარემოებით, რომ ტუტე ნაერთებით წარმოქმნილ მყარ ხსნარებში შედის მინდვრის შპატების მონოკლინიკური სახესხვაობები. სახელდობრივ, ადულიარი და ბარბიერიტი, მაშინ როდესაც, სისტემაში ალბიტი – მიკროკლინი, მყარი ხსნარების ფორმირებაში "მონაწილეები" წარმოადგენს ტრიკლინიკურ სახესხვაობებს. რაც, ენერგეტიკული პარამეტრებით აისახება. ცდომილებები ეტალონებთან მიმართებაში $\Delta H^{o}_{f,298}$-ს შემთხვევაში 0.20-0.52%-ია, $\Delta G^{o}_{f,298}$-ს შემთხვევაში – 0.1-0.4%. S^{o}_{298}-ს და $C_{p,298}$-ს შემთხვევებში, შესაბამისად 0.24-1.99 და 0.07-1,73 ენტროპიული ერთეული.

საკვანძო სიტყვები: სილიკატი, კარკასული, სტრუქტურული ინგრედიენტი, თერმოდი-ნამიკური პარამეტრი, მინდვრის შპატი, ფელდშპატი, ფელდშპატიდი. პლაგიოკლაზი, ნე-ფელინი.

UDC 544.2

OBTAINING OF NITRIDE ON THE SURFACE OF SINGLE-CRYSTALLINE GERMANIUM FOR PHOTOCATALYTIC RESEARCH

G.Kakhniashvili[1], Z.Adamia[2,3], I.Nakhutsrishvili[1]

[1]Georgian Technical University, 77 Kostava st., 0171 Tbilisi, Georgia

[2]University of Georgia, 77a Kostava st., 0171 Tbilisi, Georgia

[3]Tbilisi State University, 1 Chavchavadze av., 0128 Tbilisi, Georgia

E-mail: iraklinakhutsrishvili52@gmail.com

Resume: ***Goal.*** The paper presented here examines the decomposition of hydrazine on the surface of single-crystalline germanium at 650°C, the kinetics of the nitride formation process at ≥650°C was studied using a microgravimetric method and the question of the possibility of using α-Ge_3N_4 and mixtures of α- and β-Ge_3N_4 as a photocatalyst was considered. ***Method.*** We used the X-ray method to determine the phase composition of germanium nitride, IR spectra analysis to determine the dynamics of the catalytic decomposition of hydrazine, and the microgravimetric method to study the interaction between hydrazine vapor and the surface of single-crystalline germanium. ***Result.*** The kinetic curves of the accumulation of hydrogen and ammonia at 650°C. It can be seen that the amount of ammonia is constant in the absence of germanium, and in its presence gradually decreases. The hydrogen content in the presence of Ge increases sharply, and in its absence it first increases and then decreases. The resulting ammonia corresponds to an equimolar amount of chemisorbed hydrazine. As a result, the total change of pressure is determined only by the decomposition reaction. The study of high-temperature decomposition of hydrazine was also carried out using IR absorption spectra. These spectra indicate that the decomposition of hydrazine at 650°C occurs mainly during the first 15 minutes and is completely completed within 30 minutes. At temperatures >650°C, nitride Ge_3N_4 is formed in hydrazine vapor on the surface of germanium. By registration mass change of the sample using the microgravimetric method, the following processes are observed: first, an increase of mass occurs due to the accumulation of hydrazine and its decomposition products on the surface, then the mass of the sample decreases due to etching of Ge with contained in hydrazine water vapors, and then observes its gradual increase due to formation of Ge_3N_4. ***Conclusion.*** It is established that at ≥650°C hydrazine decomposes on the surface of single-crystalline germanium according to the scheme: $2N_2H_4 \rightarrow 2NH_3+N_2+H_2$. A sharp increase in the amount of hydrogen and a decrease in the amount of ammonia in the presence of germanium is observed. This is due to a heterogeneous reaction: $3Ge+4NH_3 \rightarrow Ge_3N_4+6H_2$. The phase composition of solid product of this reaction is an indicator of the degree of humidity of hydrazine: in pure hydrazine vapors, β-Ge_3N_4 is formed on the

surface of germanium, and as water is added, a mixture of α- and β-modifications is formed until pure α-Ge_3N_4 is formed. The question of the possibility of using α-Ge_3N_4 and mixtures of α- and β-Ge_3N_4 as a photocatalyst was considered.

Key words: Germanium, hydrazine, nitride, catalysis, mass change.

1. INTRODUCTION

Germanium nitride Ge_3N_4 finds application in micro- and nanoelectronics, photoluminescence, energy storage, photocatalysis [1-10] and others. Usually Ge_3N_4 is obtained by interaction of ammonia with elemental germanium at (650-700)°C or its dioxide (GeO_2) at (700-750)°C:

$$3Ge+4NH_3 \longrightarrow Ge_3N_4+6H_2 \quad (1)$$

$$3GeO_2+4NH_3 \longrightarrow Ge_3N_4+6H_2O \quad (2)$$

Germanium nitride exists in the form of several crystal modifications: α-, β-, γ-, δ- Ge_3N_4 [11-13]. The t-, m-, o-modifications of nitride are also theoretically discussed [14, 15] (α, β, δ – hexagonal, γ – cubic, t – tetragonal, m – monoclinic, o – orthorhombic syngony). At normal temperatures and pressures, only the α- and β-modifications are stable. According to reaction (1), the α-modification of nitride is formed, and according to reaction (2), the β-modification.

Bot modifications consist of $Ge(N_4)$ tetrahedra and crystallize in hexagonal syngonia. The difference between them lies in the arrangement of $Ge(N_4)$ tetrahedra along the "c" axis (Fig. 1). The values of elementary cell parameters from various literature data are given in Table 1. Fig. 2 shows their elementary cells.

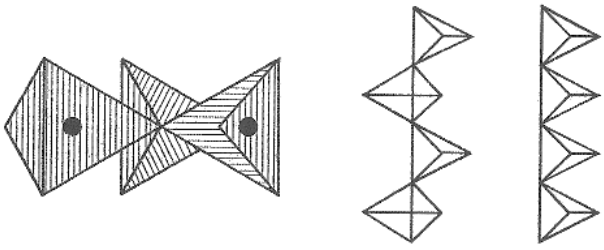

α-Ge_3N_4 (a) β-Ge_3N_4 (b)

Fig. 1. (a) - Triplets of $Ge(N_4)$ tetrahedra (in the center - Ge, on the peaks - N) and (b) - arrangement of tetrahedra along the "c" axis (vertical direction)

Table 1

Parameters of elementary cells of α- and β-Ge_3N_4

modif. / par.,Å	α-Ge_3N_4	β- Ge_3N_4
a	8.202 [11], 7.985 [12]	8.038 [11], 7.826 [12] , 8.119 [13]
c	5.94 [11], 5.786 [12]	3.074 [11], 3.993 [12], 3.104 [13]

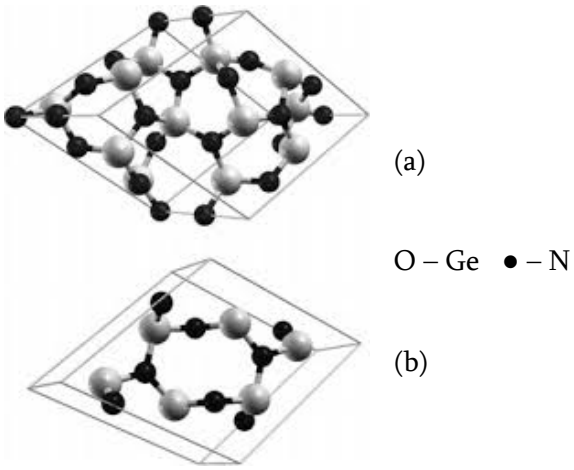

Fig. 2. Elementary cells of germanium nitride:
(a) α-Ge_3N_4, (b) β-Ge_3N_4

Below it will be shown that at 650°C hydrazine in the presence of germanium decomposes according to the scheme:

$$2N_2H_4 \rightarrow 2NH_3+N_2+H_2 \quad (3)$$

It is known that at experimentally achievable temperatures and pressures, nitrogen does not interact with germanium, and the Ge-H bond is broken below 650°C. Therefore, in hydrazine vapors, nitride is actually formed according to scheme (1). Since germanium is an active catalyst for the decomposition reaction of hydrazine, this issue will be discussed in detail.

2. MAIN PART

Commertial hydrazine-hydrate containing 50 mol.% (36 wt.%) water was distilled using the Raschig's method with improvement. In particular, before distillation, it was boiled with NaOH in an inert atmosphere of nitrogen at a temperature of 120°C for two hours. Hydrazine purified in this way had a density of ρ ≅1.0024

g/cm^3 and a refractive index of $n_D^{20} \cong 1.4705$. According to the literature, this latter value corresponds to 100% N_2H_4. However, this can be considered not entirely correct.

Plates of single-crystalline germanium doped with antimony (charge carrier concentration $n \cong 2 \cdot 10^{14} cm^{-3}$) had a resistivity of ≅35 Ohm·cm. The crystallographic orientation of Ge plates are (111) or (100). They were previously degreased in boiling toluene, etched in liquid etchant $HF:HNO_3:CH_3COOH$=1:15:1 for 4-5 minutes and washed in running distilled water.

3. RESULTS AND DISCUSSION

3.1. Decomposition of hydrazine on the surface of single-crystalline germanium

Hydrazine is one of the most chemically active substances - a strong reducing agent. He has wide application in various fields of industry, technology, medicine, etc. and has been intensively studied both previously and currently [14-25]. Liquid N_2H_4 is very hygroscopicand has a noticeable ability to absorb oxygen and carbon dioxide from the air. It is called “high purity” when the water content does not exceed 1 wt.% and “ultrapure” - with a maximum of 0.5 wt.% H_2O. The concentration of water in hydrazine is estimated by the density, melting point, or refractive index of the mixture. However, literature data on these parameters are different, due to the difficulty of accurately determining the physical characteristics of pure hydrazine (*).

Hydrazine is easily decomposed by heat and radiation, especially in the presence of catalysts [35-38]. The general form of this reaction is given by the equation:

$$3N_2H_4 \rightarrow 4(1-x)\ NH_3 + (1+2x)\ N_2 + 6xH_2 \qquad (4)$$

Depending on external conditions (temperature, pressure, catalyst, electromagnetic radiation, electric discharge, etc.) $0 \leq x \leq 1$(**). The catalytic decomposition of hydrazine on the surface of germanium has been studied relatively little and there is data when carrying out the reaction up to 80°C. In early work [32], powders of Ge of n- and p-type conductivity were used. It was found that the decomposition products were ammonia and nitrogen:

$$3N_2H_4 \rightarrow NH_3 + N_2 \qquad (5)$$

The type of conductivity did not affect the catalytic properties.

Figure 3a shows the kinetic curves of the accumulation of hydrogen and ammonia at 650°C. It can be seen that the amount of ammonia is constant in the absence of germanium, and in its presence gradually decreases. The hydrogen content in the presence of Ge increases sharply, and in its absence it first increases and then decreases. The resulting ammonia corresponds to an equimolar amount of chemisorbed hydrazine. As a result, the total change of pressure (Fig. 3b) is determined only by the decomposition reaction.

(*) According to various authors, the density of liquid hydrazine at 25°C is 1.0045, 1.0036 and 1.0024, 1.008 g/cm^3 at 23°C. The melting point of the system N_2H_4/H_2O: 1, 1.4, 1.53, 1.6-1.7, 1.8, 1.85 and 2°C [26-28].

(**) On alkaline catalysts x=1, on some semiconductor catalysts (Ga, Ga_2Se_3 and others), as well as on some metals (Te, Pt) x=0, on some semiconductors (V_2O_5, Ga_2Te_3 and others), as well as on acid catalysts $0<x<1$, during decomposition using a spark x = 0.38, and during bombardment with α-particles x = 0.12-0.22 [29-31].

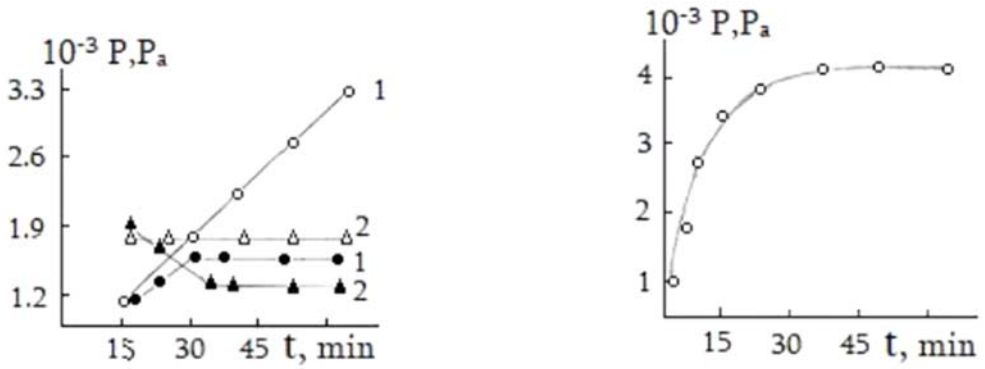

(a) (b)

Fig. 3. (a) Kinetic curves of hydrogen (1) and ammonia (2) accumulation during the decomposition of hydrazine in the presence of germanium (●, ▲) and without it (o, Δ); (b) kinetic curve of the total change of pressure of gaseous products at 650°C

Thermodynamic calculation of the change of free energy showed that reaction (5) at x = 0.25 (i.e. reaction (4)) has almost the same probability as reaction (6): change in Gibbs free energy ΔG≅220.5 and ≅222.6 kJ/mol respectively (*). However, the discovered fact of hydrogen evolution gives preference to reaction (4).

A sharp increase of the amount of hydrogen and a decrease of the amount of ammonia in the presence of germanium can be associated with a heterogeneous reaction (1).

The study of high-temperature decomposition of hydrazine was also carried out using IR absorption spectra. Figure 4 shows the IR spectra of N_2H_4 vapor, demonstrating the dynamics of its decomposition at 650°C. Curve 1 corresponds to hydrazine vapor, curves 2 and 3 to hydrazine heated for 15 and 30 minutes, and curve 4 to pure ammonia. These spectra indicate that the decomposition of hydrazine at 650°C occurs mainly during the first 15 minutes and is completely completed within 30 minutes.

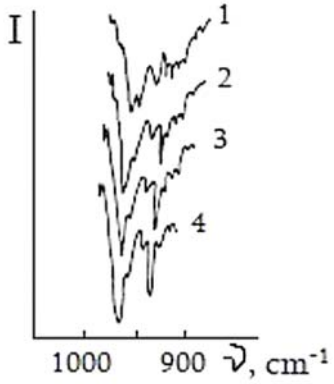

Fig. 4. Dynamics of hydrazine decomposition at 650°C in presence of germanium

(*) The estimate of ΔG should be considered approximate since a change in pressure occurs in the reaction area.

3.2. Formation of nitride on germanium surface in hydrazine vapor

At temperatures >650°C, nitride Ge_3N_4 is formed in hydrazine vapor on the surface of germanium. By registration mass change of the sample using the microgravimetric method, the following processes are observed [16]: first, an increase of mass occurs due to the accumulation of hydrazine and its decomposition products on the surface, then the mass of the sample decreases due to etching of Ge with contained in hydrazine water vapors, and then observes its gradual increase due to formation of Ge_3N_4.

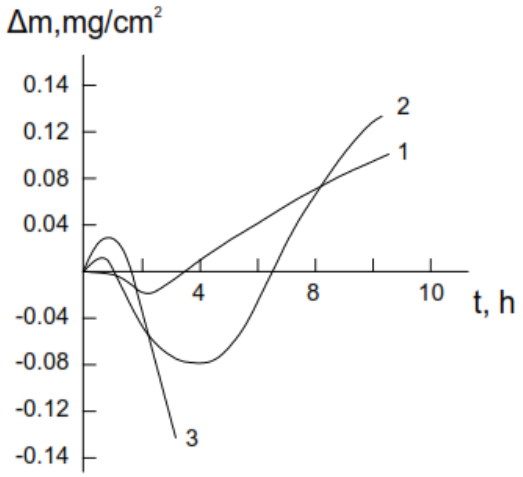

Fig. 5. The kinetic curves of the interaction of hydrazine vapors with germanium at 700°C: 1 - the process carried out immediately after distillation, 2 - after two weeks, 3 - after a month

It should be noted that when freshly distilled hydrazine was stored in a special ampoule under vacuum, over fairly long periods of time (two weeks, a month), we did not detect any change in determining of the refractive index within the measurement accuracy. However, a significant difference in the nitridation kinetics was observed (Fig. 5). From this figure, in particular, one can see the difference in the etching rates of the germanium surface at the same temperature [33]. This can be attributed to the gradual humidization of hydrazine, despite precautions. Really, under the above conditions, the following occurs: first, β-Ge_3N_4 is formed, and then traces of α-modification are observed in the nitride. When hydrazine is specially hydrated, the amount of α-Ge_3N_4 increases and it is finally possible to obtain it in pure form [34].

It should also be noted that the initial increase of mass (Fig.5) is 2-3 orders of magnitude greater than is typical for physical adsorption. This can be associated with the accumulation of polar molecules of hydrazine and water with high dipole moments (~2 D [35,36]) on the germanium surface.

One can also take into account the existence of hydrazine in the imide tautomeric form:

$$H_2N\text{-}NH_2 \leftrightarrow N^-H\text{-}N^+H_3.$$

The bipolar imide form of hydrazine is characterized by a pronounced ability to associate molecules and a strong donor property to atoms with unfilled d- and f-shells, especially in substances with a small band gap (for example, germanium).

The above can be confirmed by the results of supplementary experiments on the interaction of germanium with ammonia, as with a molecule of the amine form. At the initial stage of this reaction at (500-700) °C, we observed an increase in the sample by (2-4) μg/cm², which is characteristic of the process of physical adsorption of neutral molecules.

3.3. The possibility of using of germanium nitride as a photocatalyst in the conversion of carbon monoxide to dioxide

The role of photocatalysis in natural photosynthesis, energy, biotechnology, ecology, other fields of science and technology, or in solving household problems is widely known. Among the compounds that are studied to achieve the catalytic effect by visible or ultraviolet radiation, non-oxide materials occupy an important place. Among them are simple (binary) nitrides: C_3N_4 [37-41], GaN [42-44], TiN [45,46], Ta_3N_5 [47,48], HfN [49,50], Si_3N_4 [51,52], Ge_3N_4.

The essence of photocatalysis is to increase of the rate or excitation of chemical reactions under the influence of light in the presence of substances that absorb light quanta and participate in the chemical transformations of these substances, repeatedly entering into intermediate interactions with them and regenerating their chemical composition after each cycle. (A simplified diagram of the process is shown in Fig.6.) All this became possible after the fundamental works of A. Fujishima [53-57].

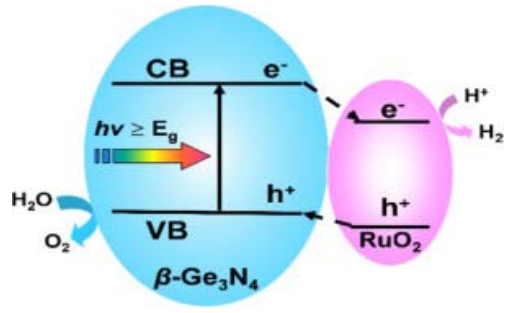

Fig. 6. Schematic representation of the photocatalytic process of water splitting [10]

As noted in the introduction, germanium nitride was successfully tested using photoradiation in the process of water splitting. The authors of the cited works used β-Ge_3N_4 doped with RuO_2.

The authors of this paper are currently conducting experiments to determine the photocatalytic activity of Ge_3N_4 for converting CO into CO_2. We use α-Ge_3N_4 and mixtures of α- and β-modifications doped with platinum or palladium. It is evident from the Fig. 2 that this modification of the nitride is capable of dissolving the dopant in itself more effectively.

The problem of converting toxic CO into harmless CO_2 is a very urgent task [58-66]. Purification of atmospheric air from harmful substances is of great importance for human health. One of the main sources of air pollution are internal combustion engines, namely cars. The most toxic component of their exhaust gases is precisely carbon monoxide. CO is especially dangerous because, due to its physical properties, it enters people's homes or workplaces more easily than other toxic exhaust gas components. It is odorless and cannot be detected by the senses. The most effective means of protecting residential and workplaces of people from carbon dioxide are cleaning devices containing photocatalysts, which, under the conditions of the use of an appropriate catalyst and natural air convection, will effectively purify them from CO.

4. CONCLUSION

At ≥650°C hydrazine decomposes on the surface of single-crystalline germanium according to the scheme: $2N_2H_4 \rightarrow 2NH_3+N_2+H_2$. A sharp increase in the amount of hydrogen and a decrease in the amount of ammonia in the presence of germanium is observed. This is due to a heterogeneous

reaction: $3Ge+4NH_3 \rightarrow Ge_3N_4+6H_2$. The phase composition of solid product of this reaction is an indicator of the degree of humidity of hydrazine: in pure hydrazine vapors, β-Ge_3N_4 is formed on the surface of germanium, and as water is added, a mixture of α- and β-modifications is formed until pure α-Ge_3N_4 is formed. The question of the possibility of using α-Ge_3N_4 and mixtures of α- and β-Ge_3N_4 as a photocatalyst was considered.

REFERENCES

1. K. Mallem, S.V. Jagadeesh Chandra, M. Ju et al. "Influence of ultra-thin Ge_3N_4 passivation layer on structural, interfacial, and electrical properties of HfO_2/Ge Metal-Oxide–Semiconductor devices," Nanosci. Nanotechn. 2020, 20, 1039 (2020)
2. Okamoto, G.; Kutsuki, K.; Hosoi, T. et al. 2011. Electrical characteristics of Ge-based metal-insulator-semiconductor devices with Ge_3N_4 dielectrics formed by plasma nitridation. Nanosci. Nanotechn. 2020, 11, 2856.
3. Huang, Z.; Su, R.; Yuan, H. et al. Synthesis and photoluminescence of ultra-pure α-Ge_3N_4 nanowires. Ceramics Intern. 2018, 4, 10858.
4. Kim, Sh.; Hwang, G.; Jung, J.-W. et al. Fast, scalable synthesis of micronized Ge_3N_4 @C with a high tap density for excellent lithium storage. Adv. Funct. Mater. 2017, 7, 1605975.
5. Maggoini, G.; Carturan, S.; Fiorese, L. et al. Germanium nitride and oxynitride films for surface passivation of Ge radiation detectors. Appl. Surface Sci. 2017, 393, 119.
6. Yayak, Y. O.; Sozen, Y.; Tan, F. et al. First-principles investigation of structural, Raman and electronic characteristics of single layer Ge_3N_4. Appl. Surface Sci. 2022, 572, 15136.
7. Sato, J.; Saito, N.; Yasmada, Y. et al. RuO_2-loaded β-Ge_3N_4 as a non-oxide photocatalyst for overall water splitting. Amer. Chem. Soc. 2005, 127, 572, 4150.
8. Lee, Y.; Watanabe, T.; Takata, T. et al. Effect of high-pressure ammonia treatment on the activity of Ge_3N_4 photocatalyst for overall water splitting. Phys. Chem. B 2006, 110, 17563.
9. K. Maeda and K. Domen. "New non-oxide photocatalysts designed for overall water splitting under visible light," Phys. Chem. C, 111, 7851 (2007)
10. Y. Ma, M. Wang and X. Zhou. "First-principles investigation of β-Ge_3N_4 loaded with RuO_2 cocatalysts for photocatalytic overall water splitting," Energy Chem., 44, 24-32 (2020)
11. S. Ruddlesden and D. Popper. "On the crystal structures of the nitrides of silicon and germanium," Acta Cryst., 11, 465-469 (1958)
12. C. Sevic and C. Bulutay. "Theoretical study of the insulating oxides and nitrides," Mater. Sci., 42, 6555 (2007)
13. Y. Luo, Y. Cang and D. Chen. "Determination of the finite temperature anisotropic elastic and thermal properties of Ge_3N_4: A first principle study," Computat. Condens. Matt., 1, 1 (2014)
14. Y. Cang, D. Chen, F. Yang and H. Yang. "Theoretical studies of tetragonal, monoclinic and orthorhombic distortions of germanium nitride polymorphs," Chem. Chinese Univ., 37, 674 (2016)

15. Cang, Y.; Yao, X.; Chen, D. et al. First-principles study on the electronic, elastic and thermodynamic properties of tree novel germanium nitrides. Semiconduct. 2016, 37, 072002.
16. I. Nakhutsrishvili. "Study of growth and sublimation of germanium nitride using the concept of Tedmon's kinetic model," Oriental J. Chem., 36, 850-854 (2020)
17. L.F. Audrieth and P.F. Mohr. "The chemistry of hydrazine," Chem. Eng. News, 26, 3746 (1948)
18. L.F. Audrieth and B.A. Ogg. "The chemistry of hydrazines," John Wiley & Sons: New York, USA, 1951, 256.
19. Schmidt, E. W. One hundred years of hydrazine chemistry. Proceedings of 3rd Conference on Environmental Chemistry of Hydrazine Fuels: 15-17 September 1987, Florida, USA, 4-16.
20. Krishnadasan, A.; Kennedy, N.; Zhao, Y.; Morgenstern, H. Nested case-control study of occupational chemical exposures and prostate cancer in aerospace and radiation workers. Amer. Industrial Medic. 2007, 50, 383.
21. Turner, J. L. Rocket and spacecraft propulsion: Principles, practice and new developments. Springer Praxis Books. Prax. Publ. LTD: New York, USA, 2009, 390.
22. E.W. Schmidt and M.S. Gordon. "The decomposition of hydrazine in the gas phase and over an iridium catalyst," Zeitsch. Phys. Chem., 227, 1301 (2013)
23. Chen, Y.; Zhao, Ch.; Liu, X. et al. Multi-scene visual hydrazine hydrate detection based on a dibenzothiazole derivative. Analyst 2022, 148, 856.
24. Yan, K.; Yan, L.; Kuang, W. et al. Novel biosynthesis of gold nanoparticles for multifunctional applications: Electrochemical detection of hydrazine and treatment of gastric cancer. Environm. Res. 2023, 238, 117081.
25. Zhang, G, Zhu, Z.*; Chen, Y. et al. Direct hydrazine borane fuel cells using non-noble carbon-supported polypyrrole cobalt hydroxide as an anode catalyst.* Sustain. Energy Fuels, 7, 2594 (2023)
26. Luo, F.; Pan, Ch.; Xie, Y. et al. Hydrazine-assisted acidic water splitting driven by iridium single atoms. Adv. Sci. 2023, 10, 2305058.
27. V.A. Burilov, R.N. Belov, S. *Solovieva and I.S.* Antipin. "Hydrazine-assisted one-pot depropargylation and reduction of functionalized nitro calix [4] arenes," Russ. Chem. Bull., 72, 948 (2023)
28. Rennebaum, T.; van Gerven, D.; Sean, S. et al. Hydrazine sulfonic acid, $NH_3NH(SO_3)$, the bigger sibling of sulfamic acid. Chem. Europe 2024, 30, e202302526.
29. E. Elts, T. Windmann, D. Staak and J. Vrabec. "Fluid phase behavior from molecular simulation: Hydrazine, Monomethylhydrazine, Dimethylhydrazine and binary mixtures containing these compounds," Fluid Phase Equilibr., 322/323, 79 (2012)
30. R.C. Ahlert, G.L. Bauerle and J.V. Lecce. "Density and viscosity of anhydrous hydrazine at elevated temperatures," Chem. Eng. Data, 7, 158 (1962)
31. B. Zhao, J. Song, R. Ran and Z. Shao. "Catalytic decomposition of hydrous hydrazine to hydrogen over oxide catalysts at ambient conditions for PEMFCs," Hydrogen Energy, 1, 1133 (2012)
32. V.M. Frolov. "Catalytic decomposition of hydrazine on germanium," Russ. Kinetics and Catalysis, 6, 149-154 (1965)

33. I. Nakhutsrishvili, Z. Adamia and G. Kakhniashvili. "Gas etching of germanium surface with water vapors contained in nitrogen-containing reagents," Appl. Surface Sci., 2, 1-5 (2024)
34. Z. Vardosanidze, I. Nakhutsrishvili and R. Kokhreidze. « Conditions of formation of α- and β-modifications of Ge_3N_4 and preparation of germanium oxynitride dielectric films," Coating Sci. and Techn., 11, 1-6 (2024)
35. A. Ekong, V.A. Akpan and O. Ebomwonyi. "DMC and VMC calculations of the electric dipole moment and the ground-state total energy of hydrazine molecule using CASINO-code," Lett. Chem. Phys. and Astronomy, 59, 106-110 (2015)
36. O.V. Krylov, V.M. Frolov, E.A. Fokina and Yu.N. Rufov. "Catalytic decomposition of hydrazine," 8th Mendeleev Congress on General and Applied Chemistry - Section of Physical Chemistry: 16-23 March, Moskow, USSR, 172-173 (1958)
37. J. Ye, Y. Wan and Y. Li. "Construction of dual S-scheme heterojunctions g-C_3N_4/CoAl LDH@MIL-53 (Fe) ternary photocatalyst for enhanced photocatalytic H_2 evolution," Appl. Surface Sci., 684, 161862 (2025)
38. M. Wtulich, A. Skwierawska, S. Ibragimov and A. Lisowska–Oleksial. "Exploring the role of carbon nitrides (melem, melon, g-C_3N_4) in enhancing photoelectrocatalytic properties of TiO_2 nanotubes for water electrooxidation," Appl. Surface Sci., 685, 161994 (2025)
39. L. Mohapatra, L. Paramanik, D. Choi and S.H. Yoo. "Advancing photocatalytic performance for enhanced visible-light-driven H_2 evolution and Cr(VI) reduction of g-C_3N_4 through defect engineering via electron beam irradiation," Appl. Surface Sci., 685, 161996 (2025)
40. P. Sharma, D. Mukherjee, S. Sakar et al. "Pd doped carbon nitride (Pd-g-C_3N_4): an efficient photocatalyst for hydrogenation *via* an Al–H_2O system and an electrocatalyst towards overall water splitting," Green Chem., 24, 5535 (2022)
41. J. Chen, S. Fang, Q. Shen et al. "Recent advances of doping and surface modifying carbon nitride with characterization techniques," Catalysts, 12, 962-968 (2022)
42. K. Ohkawa, W. Ohara, D. Ushida and M. Deura. "Highly stable GaN photocatalyst for producing H_2 gas from water," Japan Appl. Phys., 52, 08JH04 (2013)
43. N. Shimosako and H. Sakama. "Quantum efficiency of photocatalytic activity by GaN films," AIP Adv., 11, 025019 (2021)
44. S. Schäfer, A. Wyrzgol, R. Caterino et al. "Platinum nanoparticles on gallium nitride surfaces: Effect of semiconductor doping on nanoparticle reactivity," Amer. Chem. Soc., 134, 12528, (2012)
45. U. Guler, S. Suslov, S.; A. V. Kildishev et al. "Colloidal plasmonic titanium nitride nanoparticles: properties and applications," Nanophotonics, 4, 269-276 (2015)
46. X. Zhou, E.M. Zolnhofer, N. Nguyen et al. "Stable cocatalyst-free photocatalytic H_2 evolution from oxidized titanium nitride nanopowders," Angew. Chem., 54, 13385 (2015)
47. S.S.K. Ma, T. Hisatomi, K. Maeda et al. "Enhanced water oxidation on Ta_3N_5 photocatalysts by modification with alkaline metal alts," Amer. Chem. Soc., 134, 19993 (2012)

48. M. Harb and J.-M. Basset. "Predicting the most suitable surface candidates of Ta_3N_5 photocatalysts for water-splitting reactions using screened coulomb hybrid DFT computations," Phys. Chem. C, 124, 2472 (2020)
49. F. Shirvani and A. Shokri. "Photocatalytic applicability of HfN and tuning it with Mg and Sc alloys: A DFT and molecular dynamic survey," Phys. B: Condensed Matter, 649, 414459 (2023)
50. D.B. O'neill, S.K. Frehan, K. Zhu et al. "Ultrafast photoinduced heat generation by plasmonic HfN nanoparticles," Adv. Opt. Materials, 9, 2100510 (2021)
51. Q. Yang, Z. Chen, X. Yang et al. "Facile synthesis of Si_3N_4 nanowires with enhanced photocatalytic applications," Materials Lett., 212, 41-48 (2018)
52. A. Munif, J. Firas and F.J. Kadhim. "Structural characteristics and photocatalytic activity of TiO_2/Si_3N_4 nanocomposite synthesized via plasma sputtering technique," Iraqi Phys., 22, 99 (2024)
53. A. Fujishima, T.N. Rao and D.A. Tryk. "Titanium dioxide photocatalysis," Photochem. and Photobiol. C: Photochem. Rev., 1, 1-21 (2000)
54. F. Seifikar and A. Habibi-Yangjeh. "Floating photocatalysts as promising materials for environmental detoxification and energy production: A review," Chemosphere, 355, 141686 (2024)
55. F. Mohamadpour and A.M. Amani. "Photocatalytic systems: reactions, mechanism, and applications," RSC Adv., 14, 20609 (2024)
56. S.B. Beil, S. Bonnet, C. Casadevall et al. "Challenges and future perspectives in photocatalysis: Conclusions from an interdisciplinary workshop," JACS, 4, 2746 (2024)
57. A. Chakravorty and S. Roy. "A review of photocatalysis, basic principles, processes, and materials," Sust. Chem. Envir., 8, 100155 (2024)
58. V.M. Haag. "Methods to reduce carbon monoxide levels at the workplace. Preventive Medic.," 8, 369-374 (1979)
59. P. Samadi, M.J. Binczarski, A. Pawlaczyk et al. "CO oxidation over Pd catalyst supported on porous TiO_2 prepared by plasma electrolytic oxidation (PEO) of a Ti metallic carrier," Materials, 15, 4301 (2022)
60. H. Kersell, Z. Hooshmand, G. Yan et al. "CO oxidation mechanisms on CoO_x-Pt thin films," *Amer. Chem. Soc.*, **142**, 8312 (2020)
61. A.A. Rostami, M. Hajaligol, P. Li et al. "Formation and reduction of carbon monoxide," Beiträge zur Tabakforsch Intern., 20, 439-444 (2014)
62. A.G. Antony, K. Radhakrishnan, K. Saravanan and V. Vijayan. "Reduction of carbon monoxide content from four stroke petrol engine by using subsystem," Vehicle Struct. & Systems, 12, 384 (2020)
63. S. Mamilov, S. Yesman, V. Mantareva et al. "Optical method for reduction of carbon monoxide intoxication," Bulg. Chem. Commun., 52, 142-148 (2020)
64. J. Bujak, P. Sitarz and R. Pasela. "Possibilities for reducing CO and TOC emissions in thermal waste treatment plants: A case study," Energies, 14, 2901 (2021)
65. B. Ruqia, G.M. Tomboc, T. Kwon et al. "Recent advances in the electrochemical CO reduction reaction towards highly selective formation of Cx products (X = 1–3)," Chem. Catalysis, 2, 1961 (2022)

66. Sh. Wilbur, M. Williams, R. Williams et al. "Toxicological profile for carbon monoxide. Agency for Toxic Substances and Disease Registry," Atlanta, USA, 2012. Bookshelf ID: NBK153696.

უაკ 544.2

ნიტრიდის მიღება მონოკრისტალური გერმანიუმის ზედაპირზე ფოტოკატალიზური კვლევისთვის

გ.კახნიაშვილი[1], ზ.ადამია[2,3], ი.ნახუცრიშვილი[1]

[1]საქართველოს ტექნიკური უნივერსიტეტი, კოსტავას ქ. 77, 0171, თბილისი, საქართველო

[2]საქართველოს უნივერსიტეტი, კოსტავას ქ. 77ა, 0171, თბილისი, საქართველო

[3]თბილისის სახელმწიფო უნივერსიტეტი, ჭავჭავაძის გამზ. 1, 0128, თბილისი, საქართველო

E-MAIL: iraklinakhutsrishvili52@gmail.com

რეზიუმე: ნაშრომში განხილულია ჰიდრაზინის ორთქლის დაშლა მონოკრისტალური გერმანიუმის ზედაპირზე 650°C ტემპერატურაზე. ნიტრიდის წარმოქმნის პროცესის კინეტიკა ≥650°C ტემპერატურაზე შესწავლილი იქნა მიკროგრავიმეტრიული მეთოდით და განხილული იქნა α-Ge_3N_4-ისა და α- და β-Ge_3N_4-ის ნარევების ფოტოკატალიზატორად გამოყენების შესაძლებლობის საკითხი.

გერმანიუმის ნიტრიდის ფაზური შემადგენლობის დასადგენად გამოყენებულია რენტგენული ანალიზი, ჰიდრაზინის კატალიზური დაშლის დინამიკის დასადგენად - ინფრაწითელი სპექტრომეტრია, ხოლო ჰიდრაზინის ორთქლსა და მონოკრისტალური გერმანიუმის ზედაპირს შორის ურთიერთქმედების შესასწავლად - მიკროგრავიმეტრიული მეთოდი.

ექსპერიმენტებმა უჩვენა, რომ ამიაკის რაოდენობა მუდმივია გერმანიუმის არარსებობისას, ხოლო მისი თანაარსებობისას თანდათან მცირდება. წყალბადის შემცველობა Ge-ს თანაარსებობისას მკვეთრად იზრდება, ხოლო მისი არარსებობისას ჯერ იზრდება და შემდეგ მცირდება. შედეგად მიღებული ამიაკი შეესაბამება ქემისორბირებული ჰიდრაზინის ექვიმოლარულ რაოდენობას. შედეგად, წნევის სრული ცვლილება განისაზღვრება მხოლოდ დაშლის რეაქციით. ინფრაწითელი შთანთქმის სპექტრები მიუთითებს, რომ ჰიდრაზინის დაშლა 650°C-ზე ძირითადად ხდება პირველი 15 წთ=ის განმავლობაში და სრულად სრულდება 30 წთ-ში. მიკროგრავიმეტრიული მეთოდით ნიმუშის მასის ცვლილების რეგისტრაციისას შეინიშნება შემდეგი პროცესები: ჯერ ხდება მასის ზრდა ჰიდრაზინის და მისი დაშლის პროდუქტების ზედაპირზე დაგროვების გამო, შემდეგ ნიმუშის მასა მცირდება ჰიდრაზინში შემავალი წყლის

ორთქლით Ge-ს ზედაპირის გაზური ამოჭმის გამო, შემდეგ კი შეინიშნება მისი თანდათანობითი ზრდა.

დადგენილია, რომ ≥650°C ტემპერატურებზე ჰიდრაზინი იშლება გერმანიუმის ზედაპირზე შემდეგი სქემის მიხედვით: $2N_2H_4 \rightarrow 2NH_3+N_2+H_2$. საბოლოოდ მიიღება ნიტრიდი შემდეგი რეაქციით: $3Ge+4NH_3 \rightarrow Ge_3N_4+6H_2$. ამ რეაქციის მყარი პროდუქტის ფაზური შემადგენლობა ჰიდრაზინის ტენიანობის ხარისხის მაჩვენებელია: სუფთა ჰიდრაზინის ორთქლში გერმანიუმის ზედაპირზე წარმოიქმნება β-ფაზა, ხოლო წყლის ორთქლის დამატებისას წარმოიქმნება α- და β-მოდიფიკაციების ნარევი სუფთა α-ფაზის წარმოქმნამდე. განხილულია α-Ge_3N_4-ის და α- და β-Ge_3N_4-ის ნარევების ფოტოკატალიზატორად გამოყენების შესაძლებლობის საკითხი.

საკვანძო სიტყვები: გერმანიუმი, ჰიდრაზინი, ნიტრიდი, კატალიზი, მასის ცვლილება.

UDC 666.762.93

PREPARATION AND STUDY OF HIGH-STRENGTH HETEROMODULAR NANOCOMPOSITE IN THE SYSTEM OF OXYGENATED AND OXYGEN-FREE COMPOUNDS

Z. Kovziridze, T. Loladze, N. Nizharadze, G. Tabatadze, N. Darakhvelidze, M. Balakhashvili

Institute of Bionanoceramics and Nanocomposite Technology, Georgian Technical University, Tbilisi 0175, Georgia, 69 Kostava Street

E-mail: kowsiri@gtu.ge

Abstract: ***Objective.*** The aim of this work is the synthesis of a high-strength heteromodular nanocomposite in the SiC–SiAlON–Al_2O_3 system, intended for application in armored vehicles, aviation, and rocket engineering, as well as for components of jet engines and high-temperature gas turbines.

Method. The nanocomposite was synthesized via a metallothermal process in a technical nitrogen atmosphere, using the reactive sintering method, resulting in a material with 15% open porosity. The resulting product was milled in a ball mill for 10 hours and then ground in an attritor for 10 minutes to achieve a particle size of 1–3 μm. Finally, the material was sintered under hot pressing at 1620 °C, producing a high-density product with enhanced mechanical and operational properties.

Results. The formation of β-SiAlON via reactive sintering at such relatively low temperatures (around 1800 °C) is facilitated both by the composition of the starting materials - aluminum, silicon, SiC, geopolymer, and perlite, and by the shift of water and gas dehydration/deaeration from the glassy perlite to relatively higher temperatures (1000–1050 °C) instead of the 860 °C indicated in perlite thermograms. This shift promotes structural opening and activates diffusion processes. As a result, SiAlON formation proceeds more intensively at 1250–1300 °C, owing to the prior activation of processes in the geopolymer-perlite composition at 1000–1050 °C.

The formation of SiAlON is such a strong physico-chemical process that the relatively high nitrogen pressure in this temperature range, combined with metallothermy, drives it to consume mullite oxides generated from internal molecular rearrangements of the geopolymer. Consequently, at the final high-temperature synthesis (1620 °C), mullite is no longer present in the phase composition. SiAlON becomes the predominant phase in the structure, accounting for 57 wt.%.

Conclusion

The progression of the process is facilitated by the release of glassy dopant-Aragats perlite, which, through eutectic interactions with the geopolymer at low temperatures, provides favorable conditions for the intensive development of diffusion processes with the other components. The study presents the results of electron microscopy, X-ray structural, and X-ray spectral analyses, as well as mathematical modeling of the physicochemical processes, which

confirm our theoretical conclusions based on practical experimental evidence.

Keywords: Composite; Hot pressing; Microstructure; Phase composition; High-strength heteromodular nanocomposite.

1. Introduction

It is well known that carbides, borides, nitrides, silicides, and similar materials possess superior operational properties compared to other materials, including high refractory resistance, excellent thermal shock resistance, corrosion resistance in aggressive media, hardness exceeding 9 on the Mohs scale, favorable macro- and micromechanical properties, specific electrical and thermophysical characteristics, and others [1–6]. Materials with such properties include SiAlONs. SiAlONs are ceramics containing multiple phases in the Si–Al–O–N system and belong to the class of silicon–aluminum oxynitride ceramics. Due to their outstanding operational properties, SiAlONs are often referred to as superceramics [7]. Their structural unit is the (Si,Al)(ON_4) tetrahedron, similar to the SiN_4 tetrahedron in silicon nitride (Si_3N_4) and the SiN_3O unit in silicon oxynitride. SiAlONs contain structural types and phases based on apatite, aluminum nitride, silicon α- and β-nitride, silicon oxynitride, spinels, and others. As mentioned above, reactively sintered SiAlON is obtained at approximately 1800 °C, while hot-pressed SiAlON is formed at 1750 °C and higher, and in a neutral atmosphere, at around 1600 °C. Therefore, the innovative technology presented in this study provides significant energy savings. According to established methods, the raw mixtures typically include aluminum nitride, silicon nitride, aluminum oxide, silicon dioxide, and silicon oxynitride. In rare cases, lithium–aluminum or magnesium–aluminum spinels are used. Single-phase SiAlON can exist in a narrow compositional range with the formula:

$$Si_{(6-x)}AlxOxN_{(8-x)}$$

$$0 \le x \le 5$$

SiAlON exhibits its best properties in the $Si_3Al_2O_3N_4$ system, which is structurally and mechanically close to silicon nitride and chemically similar to aluminum oxide. Its technological versatility allows it to be widely used across multiple engineering fields [7].

It should also be noted that SiAlON demonstrates optimal cutting properties when the glass phase content reaches 20–25% [7]. In terms of thermal stability, SiAlONs are superior to almost all other ceramic materials. KYON [7] is regarded as one of the most effective materials for cutting applications. Several types of SiAlONs exist [8–9].

2. Main Section

Based on the raw materials used, Table 1 was compiled, showing the variation in compositions. From these compositions, sample CH-7 was selected, which undergoes reactive sintering at 1450°C, due to its superior physicochemical and technical properties compared to other compositions: flexural strength σ = 258 MPa, chemical resistance to water – 99.79%, and resistance to acid (H_2SO_4, ρ=1.84) – 99.25%. Subsequent investigations focused on studying the properties of this sample.

The chemical composition of kaolin (wt.%): SiO_2-46.45; TiO_2-0.33; Al_2O_3-38.70; Fe_2O_3-0.46; MgO – trace, CaO-0.36; Na_2O-0.45; K_2O-0.60; heat loss - 13.63; refractoriness: - 1770 °C. The chemical composition of Polohy clay (wt.%): SiO_2-47.92;

Al_2O_3-35.20; Fe_2O_3-2.06; TiO_2-O.28; CaO-0.40; MgO-0.30; K_2O-O.65; Na_2O-O.42; heat loss - 12.24. refractoriness:– 1760^{0}C.

To obtain a dense, high-hardness material, the reactively sintered powder was first milled in a ball mill for 10 h and subsequently ground in an attritor for 10 min. The precursor for hot pressing was prepared using a hydraulic press with a disk 70 mm in diameter and 5 mm thick and a cylinder 15 mm in diameter, under a pressure of 20 MPa. Hot pressing was carried out in vacuum at 1620 °C under 30 MPa, with a vacuum level of 10^{-3} Pa and a 10 min dwell at the final temperature.

The sintering regime was as follows: 20–500 °C for 70 min, 500–1400 °C for 150 min, and 1400–1620 °C for 10 min, followed by cooling for 10 min. The hot-pressed samples exhibited an open porosity of 0.18%, total porosity of 2.58%, σ=1910 MPa, and σ_b of=470 MPa. Notably, the material was so hard that several disks were damaged during diamond cutting. Attempts to cut the disks using a water jet at 3000 atm were unsuccessful, indicating that laser machining is the only feasible method. The samples were subsequently tested on a Rockwell hardness tester, yielding HRA=94. The dynamic microhardness and modulus of elasticity of the obtained materials were determined according to ISO 14577, using a DUN-211 S dynamic ultramicrohardness tester. The results are presented in Table 2 and Figure 1.

Table 1

Composition of the mixtures

Composite index	Initial component content, wt. %								
	Kaolin prosianaia (Ukraine)	Al	Al_2O_3	SiC	Si	Perlite from Aragats (Armenia)	Y_2O_3	MgO	Polohy clay (Ukraine)
SN-1	80,00	20.00							
SN-2	20.00	10.00		70.00					
SN-3	20.00	10.00	70.00						
SN-6	18.52	18.52	18.52	18.52	20.37	2.78	1.85	0.92	
SN-7	13.89	23.15		27.78	25.00	3.0	1.85	0.92	4.41
SN-8	13,89	23,15	27,78		25,00	2,78	1,85	0,92	4,63

Table 2

Technical properties of the CN-7 composite under 1 N load

<<Testcondition-SiAlon-100 >>

Testmode	Load-unload		
Samplename	SiAlon-zv	SampleNo.	#1
Testforce	100.000[gf]	Minimumforce	0.200[gf]
Loadingspeed	1.0(7.1448[gf/sec])	Holdtimeatload	5[sec]
Holdtimeatunload	3[sec]	Testcount	23
Parametername	Temp	Parameter	20
Comment	20.06.17-SiAlon-zv-100;DHV5-3		
Poisson'sratio	0.190		
Cf-Ap, As Correction	ON	Indentertype	Vickers
Readtimes	2	Objectivelens	50

Indenter elastic 1.140e+006[N/mm2] Indenter poisson's ratio 0.070

<Testresult>

SEQ	Fmax	hmax	hp	hr	DHV-1	DHV-2	Eit	Length	HV	Dataname
	[gf]	[um]	[um]	[um]			[N/mm2]	[um]		
1	100.753	2.0927	1.0353	1.3623	1124.606	4595.143	2.023e+005	12.133	1269.108	SiAlon-100(1)
2	100.862	2.1408	1.1973	1.4454	1075.849	3439.729	2.028e+005	10.673	1641.878	SiAlon-100(2)
3	100.954	2.1185	1.0085	1.3472	1099.608	4852.203	1.911e+005	11.989	1302.427	SiAlon-100(3)
4	100.844	2.1300	0.9980	1.3526	1086.598	4949.256	1.881e+005	11.623	1384.295	SiAlon-100(4)
5	100.935	2.1822	1.1183	1.4290	1036.181	3945.265	1.855e+005	12.721	1156.721	SiAlon-100(5)
6	100.624	2.0945	1.0240	1.3135	1121.301	4691.482	1.921e+005	11.843	1330.428	SiAlon-100(6)
7	100.551	2.1229	1.0193	1.3350	1090.715	4731.042	1.868e+005	11.551	1397.624	SiAlon-100(7)
8	100.826	2.1357	1.0016	1.3362	1080.626	4912.610	1.834e+005	11.550	1401.679	SiAlon-100(8)
9	100.826	2.1173	0.9846	1.2881	1099.473	5084.458	1.815e+005	11.404	1437.730	SiAlon-100(9)
10	100.825	2.1761	1.0974	1.4160	1040.858	4092.733	1.848e+005	11.697	1366.620	SiAlon-100(10)
11	100.807	2.1566	1.0491	1.3859	1059.580	4477.130	1.857e+005	-----	-----	SiAlon-100(11)
Average	100.801	2.1334	1.0485	1.3646	1083.218	4524.641	1.895e+005	11.718	1368.851	
Std.Dev.	0.120	0.029	0.064	0.049	28.966	502.835	7155.469	0.529	125.730	

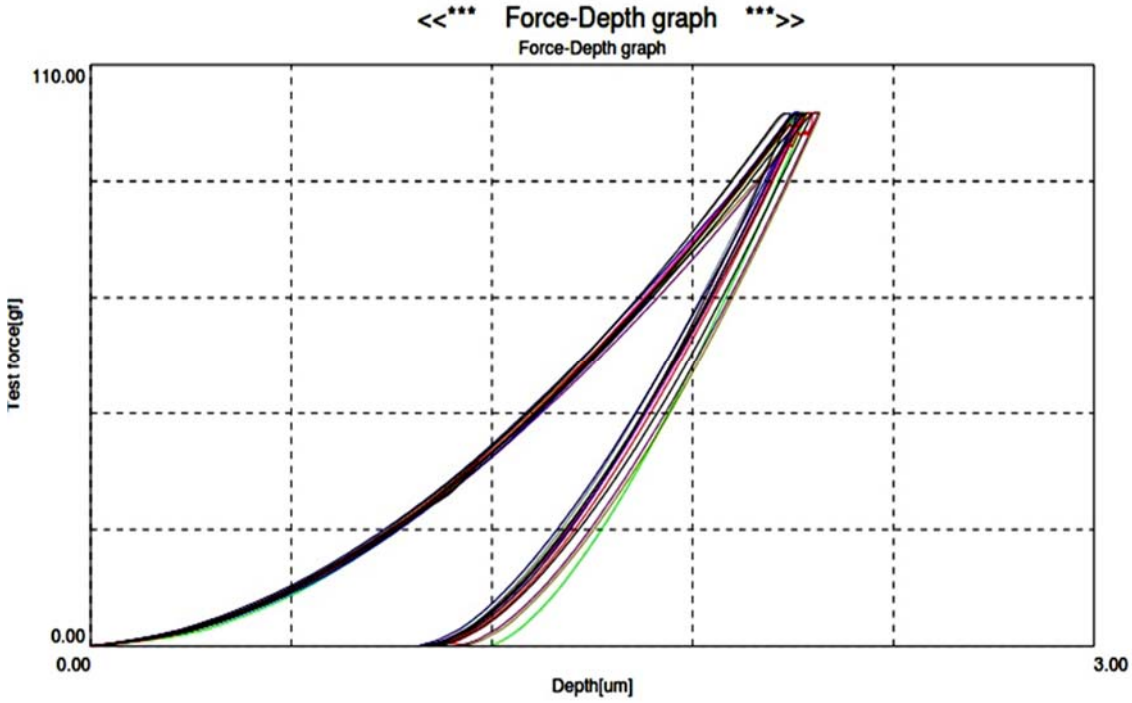

a)

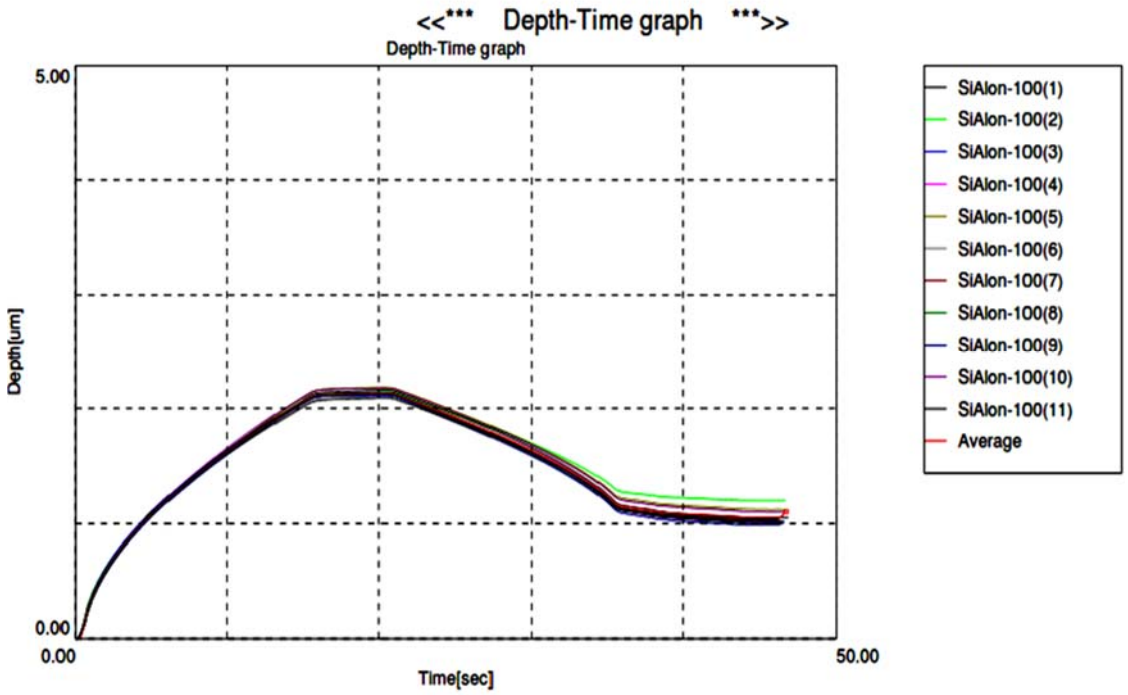

b)

Figure 1. Micromechanical properties of the CH-7 composite under 1 N load: (a) Dependence of indenter penetration on time; (b) Dependence of indenter load on imprint depth

As shown in Table 2 and Figure 1, the imprints in the matrix, which are SiAlON-based, exhibit nearly the same depth under a 1 N (100 g) load. From this, it can be concluded that the optimal load for SiC–SiAlON–Al_2O_3 phase composition is 1 N. The hardness, measured by the Vickers method, was 13.68 GPa, the average imprint depth (Figure 1) was 2.13 μm, the dynamic hardness was DHV = 10.83 GPa, the elastic modulus was E = 189 MPa, and the imprint diagonal was 11.72 μm. The table and graphical data in the figure indicate that the composite matrix is homogeneous and does not exhibit significant variations in properties, despite the imprints being taken from different locations within the matrix.

Figure 2 shows the phase composition of the material. The X-ray diffraction (XRD) pattern was recorded using a DRON-3 diffractometer. Phase analysis indicates the presence of SiAlON, silicon carbide (SiC), and aluminum oxide formed from the clay component. Phase analysis indicates the presence of aluminum oxide, which is formed from SiAlON, silicon carbide (SiC), and the clay component.

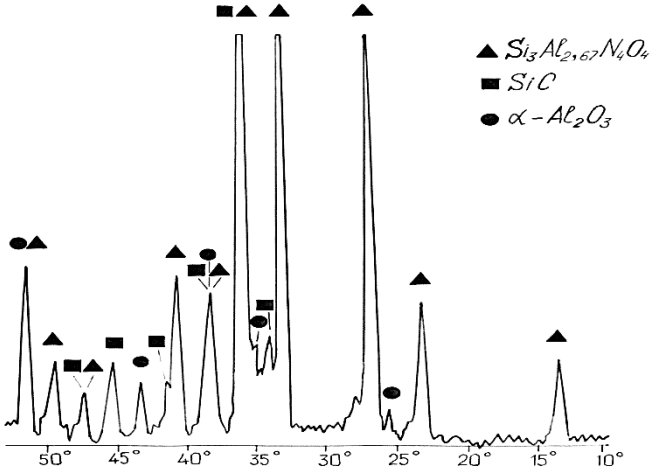

Figure 2. X-ray diffraction (XRD) pattern of the CN-7 composite

The structural–morphological characteristics and elemental composition of the samples were investigated using a JEOL JSM-6510LV scanning electron microscope (Japan) equipped with an X-Max^N energy-dispersive X-ray spectrometer manufactured by Oxford Instruments (UK). Surface electron images were obtained using both secondary electron imaging (SEI) and backscattered electron signals (BES) at an accelerating voltage of 20 kV. In certain cases, to reduce surface charging, the samples were coated with an approximately 10 nm thick Pt layer using a JEOL JEC-3000FC vacuum coating system.

For the structural investigation, electron microscopic morphological images acquired at different magnifications were used in order to more accurately determine the sizes of crystals and pores during the phase analysis. The pores are predominantly rounded, indicating complete densification of the material (Fig. 3). The total volume fraction of closed pores is 2.4%, and their average

diameter is 1.7 μm. These results are fully consistent with Budworth's findings regarding pore volume fraction and its influence on the technical properties of materials within a matrix [10]. Other types of pores, such as open or partially open pores, were not observed in the structure.

For the morphological analysis of the crystalline phases, electron microscopic images obtained at different magnifications were used, allowing assessment of the structure and spatial distribution of each phase. At low magnifications (×100 and ×270), the presence of sialon is not clearly discernible in the images, most likely due to its poorly defined morphology. In this case, the dominant phase observed in the micrographs is SiC.

As for aluminum oxide, whose presence is also confirmed by X-ray diffraction analysis, it is mainly formed from the geopolymer component, which constitutes 18% of the mixture. A minor contribution may also originate from aluminum powder; since the nitrogen used is technical grade, its content, determined through crystalline phase analysis and grain-counting methods, was found to be 5.7%. The SiC content in the structure remains nearly constant at approximately 27.78%.

At a magnification of ×2700, the contours of the sialon phase begin to emerge, and its morphology becomes more apparent, although it is still not well defined. A distinctly different picture is observed at ×5500 magnification, where the structure can be characterized as sialon-based, and this phase becomes visually dominant within the matrix. Its content, calculated to be 56.7%, remained the same in all previous morphological analyses; however, it was not visually evident at lower magnifications. Consequently, for the sialon-based SiC–SiAlON–Al_2O_3 materials obtained in this study, the minimum magnification required for reliable visual morphological analysis is ×5500.

At ×10,000 magnification, the lamellar structure of sialon and its dominant role in the morphology are clearly observed. This represents the classical sialon morphology. Other constituents, such as SiC, despite its relatively high content of 27.78 wt.%, are less visible due to coverage by sialon lamellae; nevertheless, its contribution to the functional performance of the material remains significant.

The role of the glassy phase, which was calculated to constitute 7.4%, is also substantial and is further addressed below through mathematical modeling of the material formation process. Although a 3% perlite dopant was added, its melting at a relatively low temperature of 1240 °C leads to the formation of eutectic melts with geopolymer components, particularly with alkali oxides. As a result, the glassy phase content in the material increases at 1620 °C.

A comprehensive X-ray spectroscopic analysis was performed (Figs. 4–10), enabling the determination of trace amounts of most chemical elements present in the investigated object, down to the level of thousandths of a percent. X-ray spectroscopic analysis is based on the dependence of the characteristic X-ray emission line frequencies of elements on their atomic numbers, as well as on the relationship between the intensities of these lines and the number of atoms involved in their generation.

Figure 4 presents micro–X-ray spectroscopic image #1 of the material obtained by hot pressing at 1620 °C. Four spectra were acquired from the sample. The figure and the corresponding table

show the elemental distribution and their percentage contents, from which it is evident that the principal constituent of the material is sialon, in agreement with our calculations.

In Figure 4, the percentage contents of the elements constituting sialon—silicon, aluminum, oxygen, and nitrogen—are nearly identical in all four spectra. Spectrum 4 shows a slightly higher nitrogen content and a lower aluminum content; however, this variation is minimal and does not affect the morphological uniformity of the image. Carbon is detected in almost equal amounts in all four spectra, confirming the significant presence of SiC in the composite. According to our calculations, its content is 27.78 wt.%.

In addition to sialon, the substantial oxygen contribution indicates a minor presence of Al_2O_3, amounting to 5.7 wt.%. In this case, the majority of the oxygen is consumed by the sialon phase.

Based on the analysis of the fifth electron micrograph, spectra 25 and 26 reveal the presence of iron at 21.9 and 22 wt.%, respectively. This indicates that, according to the X-ray spectroscopic analysis, the detected iron originates from the geopolymer component of the material. Consequently, the sialon and aluminum oxide contents in these two spectra are likely lower.

The remaining four spectra demonstrate the presence of sialon, SiC, and Al_2O_3. Minor elements, such as Mg and Y, were intentionally introduced as dopants to act as crystal growth inhibitors, while Ca, Zr, Mn, and Fe originate from the chemical composition of the geopolymer. Given their very low concentrations, these elements are unlikely to significantly affect the functional properties of the material. Their presence may only account for slight deviations from theoretical calculations, which are typical in any material.

Analysis of the sixth electron micrograph shows that iron is present only in spectra 31 and 35, at 5.5 and 4.2 wt.%, respectively, which we also attribute to the geopolymer component of the material. In the remaining spectra, the phase composition of the material is largely preserved, with only minor deviations from the calculated mass percentages of the phases, which is a common occurrence.

Analysis of the ninth electron micrograph indicates that all spectra exhibit a phase composition of SiAlON, SiC, and Al_2O_3. It should be noted that SiC is not fully represented in terms of atomic percentages; apparently, the sialon phase overlaps it, and carbon is detected at only 8% in the spectra. The remaining elements—Ca, Zr, Mg, and Fe—are present in negligible amounts.

The thirteenth electron micrograph is particularly noteworthy. Spectra 74 and 76 show iron contents of 26.3 and 38 wt.%, respectively, which originate from the geopolymer component. Spectra 77, 78, and 79 display only the presence of SiC, suggesting that these spectra were taken from SiC grains. Spectra 80 and 81 are predominantly sialon, while spectrum 82 shows a minor iron content of 6%, again originating from the geopolymer. The other elements introduced by the geopolymer are present only in negligible amounts.

The seventeenth electron micrograph shows that, according to spectra 104–107, the phase composition consists solely of silicon carbide, indicating that these spectra were acquired from SiC grains. The remaining spectra demonstrate the phase composition of the composite within the SiC–SiAlON–Al_2O_3 system.

The lamellar structure of sialon is clearly visible in the eighteenth electron micrograph, captured at a magnification of ×10,000. Spectra 111 and 113 show only the presence of silicon carbide, indicating that these spectra were obtained from SiC grains. In the remaining spectra, the phase composition of the resulting composite within the SiC–SiAlON–Al_2O_3 system is observed.

The micro–X-ray spectroscopic analyses presented in the figures provide a detailed representation of the elemental composition at the measured points, showing the percentage content of the main phases containing sialon, silicon carbide, and corundum. In a few spectra, only the presence of silicon carbide is detected, which is a common occurrence in X-ray spectroscopic analysis. Apart from these exceptions, the percentage ratios across all areas are nearly uniform, indicating a homogeneous structure of the investigated composite. The phase composition, as determined from our calculations, is as follows (wt.%): 56.7 – sialon, 27.78 – silicon carbide, 5.7 – aluminum oxide, 7.4 – glassy phase, 2.4 – porous phase, and the remainder from the geopolymer component (Figs. 4–10).

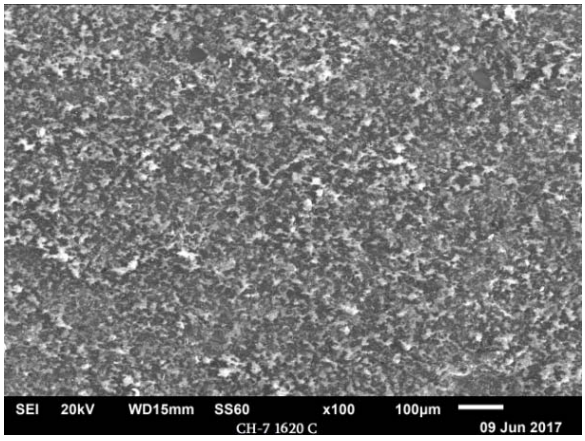

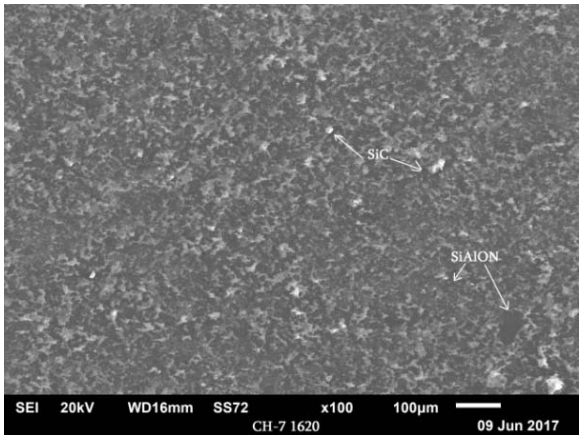

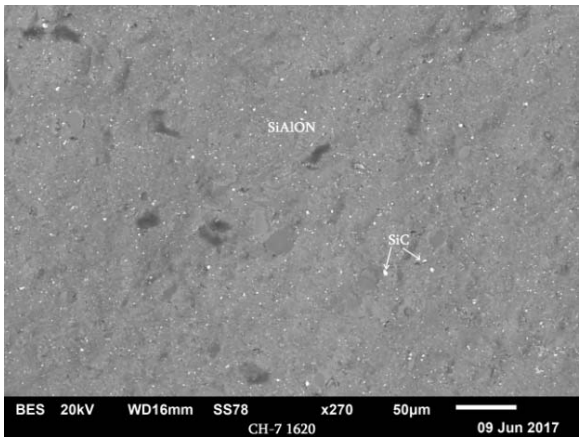

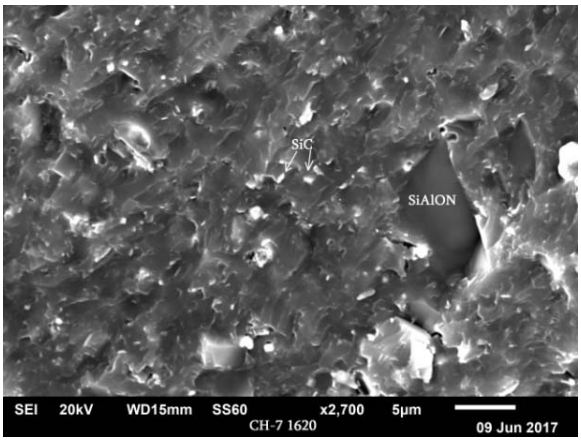

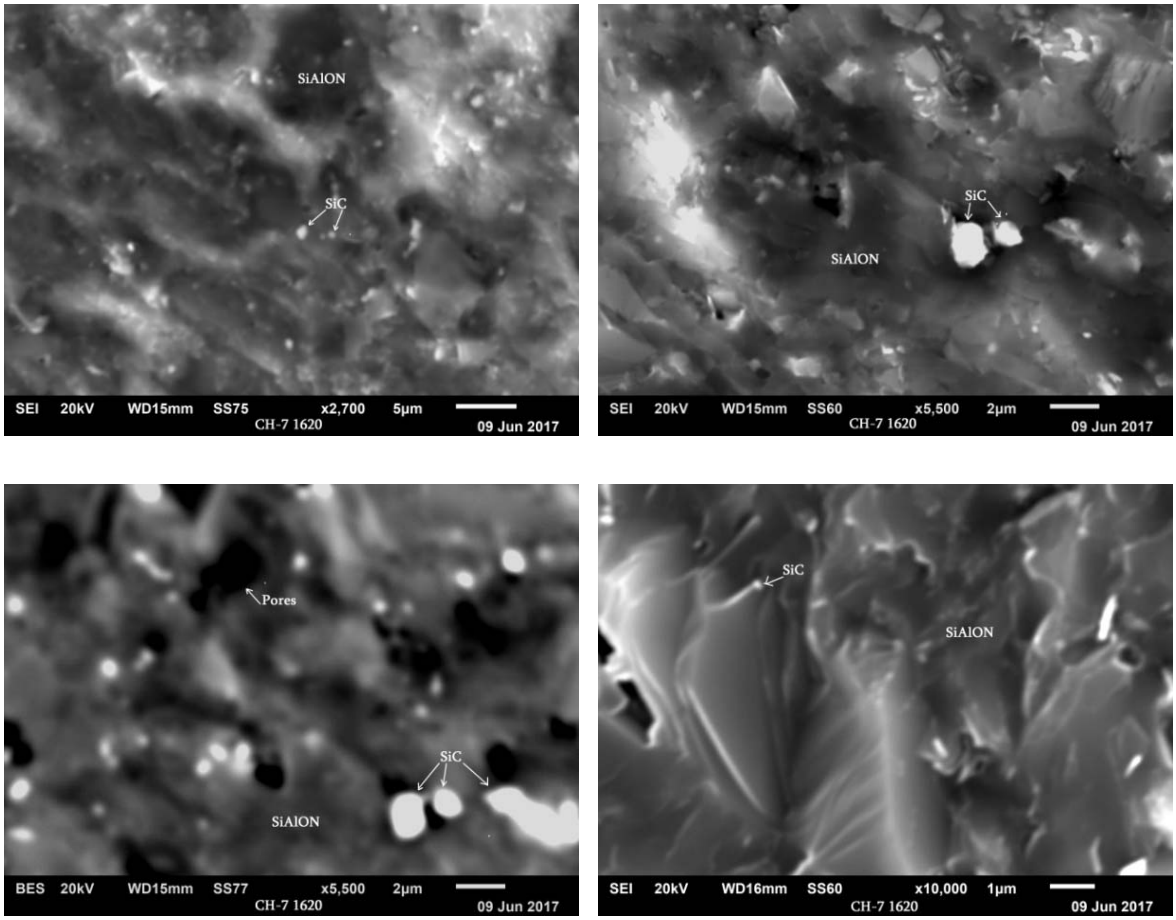

Figure 3. Scanning electron microscopy (SEM) images
of the CH-7 sample at different magnifications

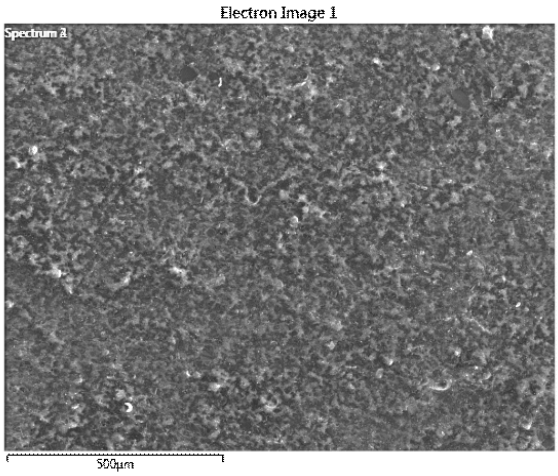

Click here to enter text.

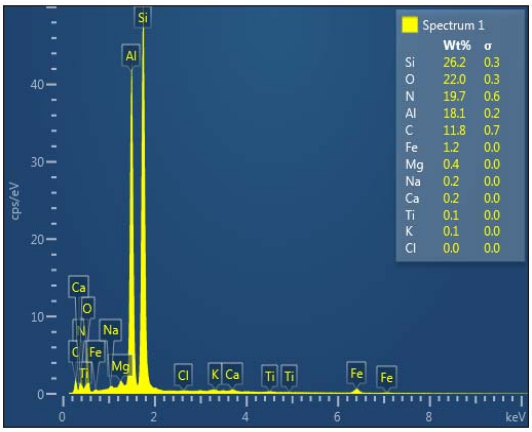

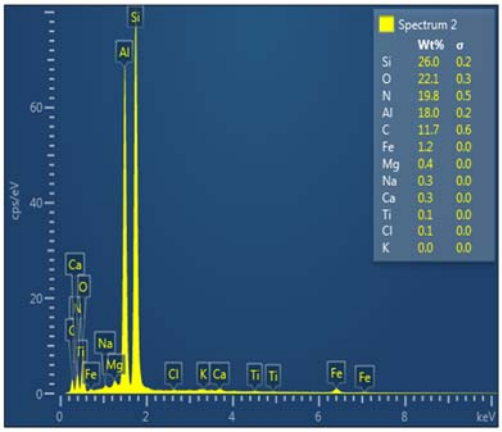

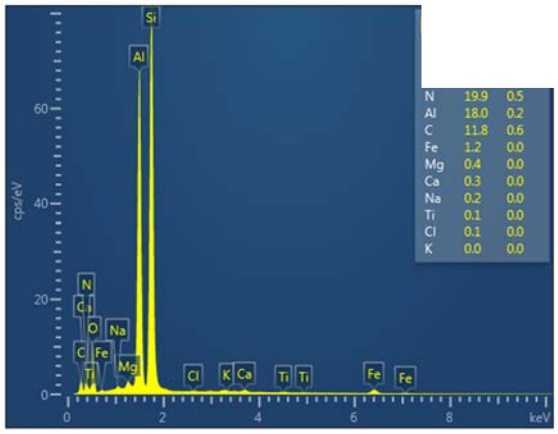

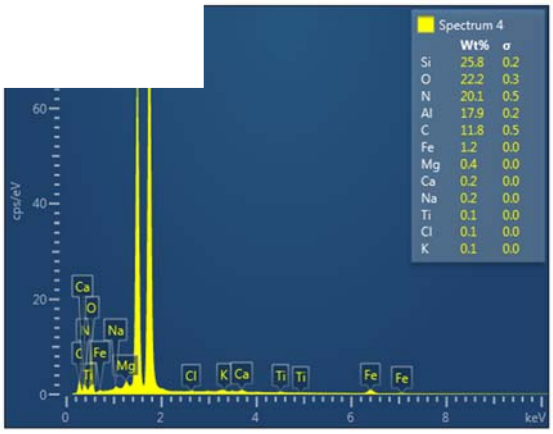

Figure 4. X-ray spectroscopic images of the CH-7 sample.

Electron micrograph 1; four points were analyzed.

Table 3

Elemental composition

Result Type	Atomic %			
Spectrum Label	Spectrum 4	Spectrum 1	Spectrum 2	Spectrum 3
C	17.99	18.17	18.01	18.02
N	26.34	25.91	26.01	26.16
O	25.52	25.34	25.50	25.46
Na	0.18	0.18	0.21	0.19
Mg	0.28	0.28	0.29	0.28
Al	12.19	12.35	12.32	12.26
Si	16.88	17.19	17.07	17.04
Cl	0.04	0.02	0.04	0.03
K	0.03	0.03	0.02	0.01
Ca	0.11	0.10	0.12	0.12
Ti	0.05	0.04	0.04	0.04
Fe	0.39	0.40	0.38	0.38
Total	100.00	100.00	100.00	100.00

Statistics	C	N	O	Na	Mg	Al	Si	Cl	K	Ca	Ti	Fe
Max	18.17	26.34	25.52	0.21	0.29	12.35	17.19	0.04	0.03	0.12	0.05	0.40
Min	17.99	25.91	25.34	0.18	0.28	12.19	16.88	0.02	0.01	0.10	0.04	0.38
Average	18.05	26.10	25.46	0.19	0.28	12.28	17.05	0.03	0.02	0.11	0.04	0.39
Standard Deviation	0.08	0.19	0.08	0.01	0.00	0.07	0.13	0.01	0.01	0.01	0.00	0.01

EDS CH-7 1620^{0}C

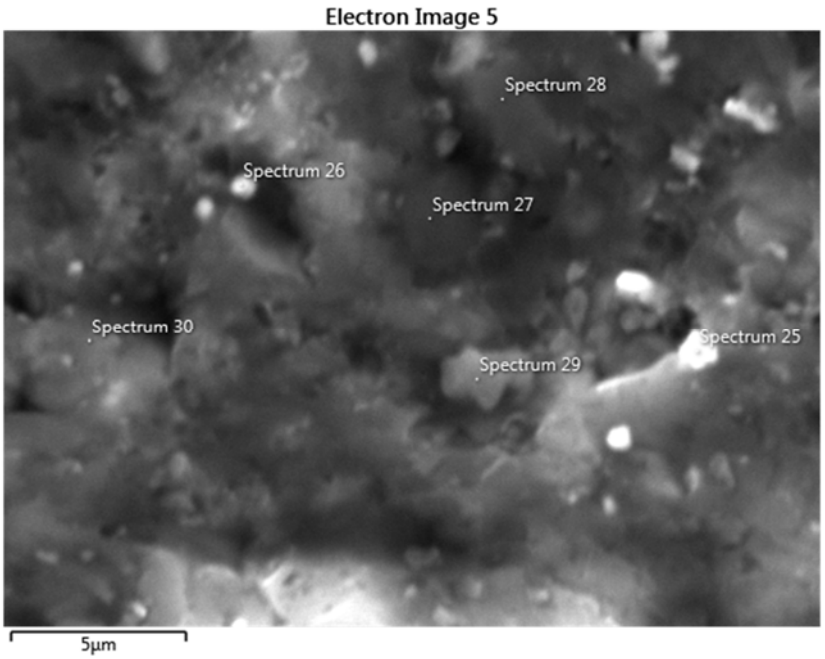

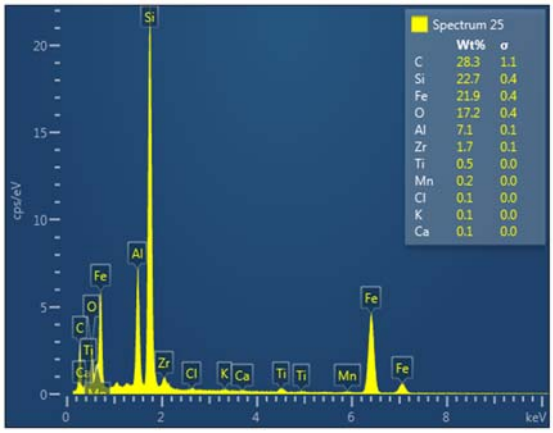

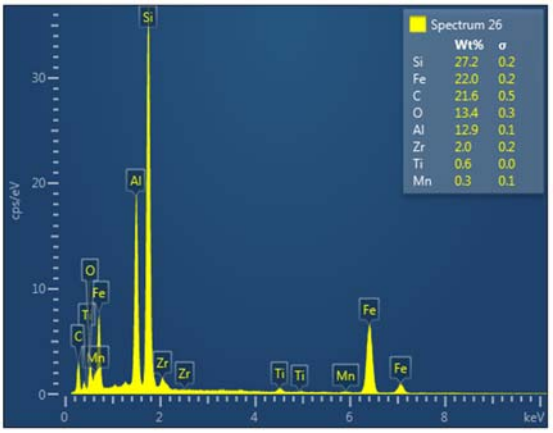

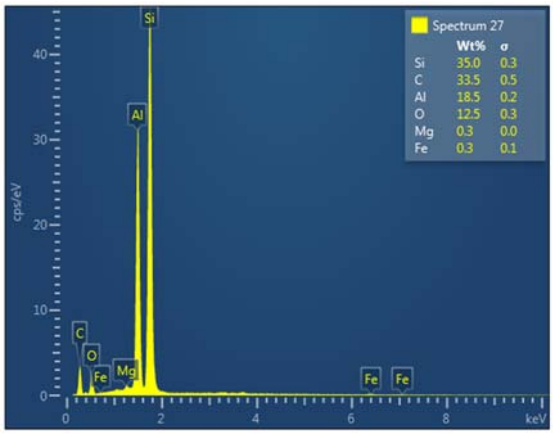

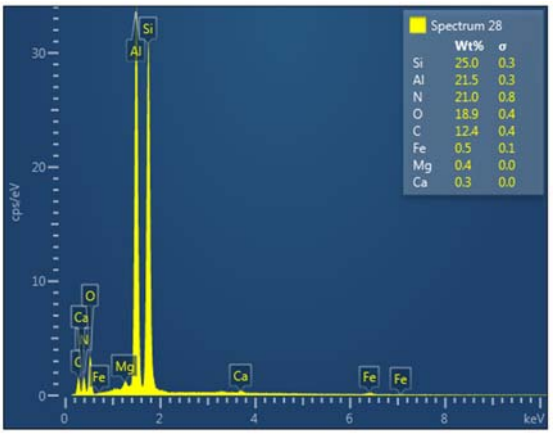

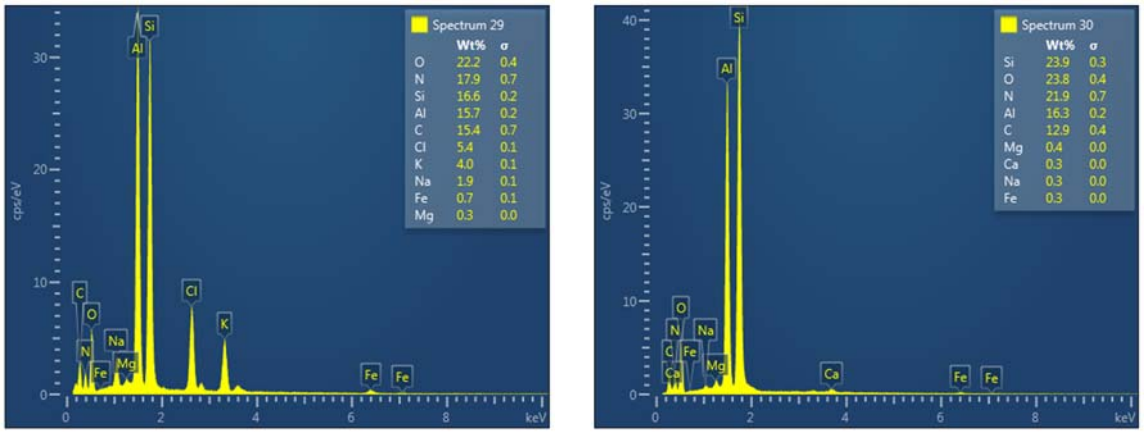

Figure 5. X-ray spectroscopic images of the CH-7 sample.

Electron micrograph 5; six points were analyzed, with results presented in Table 4 showing the elemental composition.

Table 4

Elemental composition

Result Type	Weight %					
Spectrum Label	Spectrum 30	Spectrum 25	Spectrum 26	Spectrum 27	Spectrum 28	Spectrum 29
C	12.87	28.31	21.58	33.47	12.44	15.39
N	21.89				20.99	17.91
O	23.80	17.17	13.37	12.53	18.95	22.22
Na	0.26					1.92
Mg	0.42			0.27	0.42	0.25
Al	16.29	7.11	12.93	18.46	21.49	15.66
Si	23.91	22.68	27.21	35.01	25.00	16.58
Cl		0.15				5.42
K		0.14				3.95
Ca	0.31	0.13			0.26	
Ti		0.52	0.57			
Mn		0.23	0.31			
Fe	0.26	21.91	21.99	0.26	0.46	0.69
Zr		1.66	2.04			
Total	100.00	100.00	100.00	100.00	100.00	100.00

Statistics	C	N	O	Na	Mg	Al	Si	Cl	K	Ca	Ti	Mn	Fe	Zr
Max	33.47	21.89	23.80	1.92	0.42	21.49	35.01	5.42	3.95	0.31	0.57	0.31	21.99	2.04
Min	12.44	17.91	12.53	0.26	0.25	7.11	16.58	0.15	0.14	0.13	0.52	0.23	0.26	1.66
Average	20.68		18.01			15.32	25.06						7.59	
Standard Deviation	8.71		4.57			4.94	6.04						11.12	

EDS CH-7 1620^{0}C

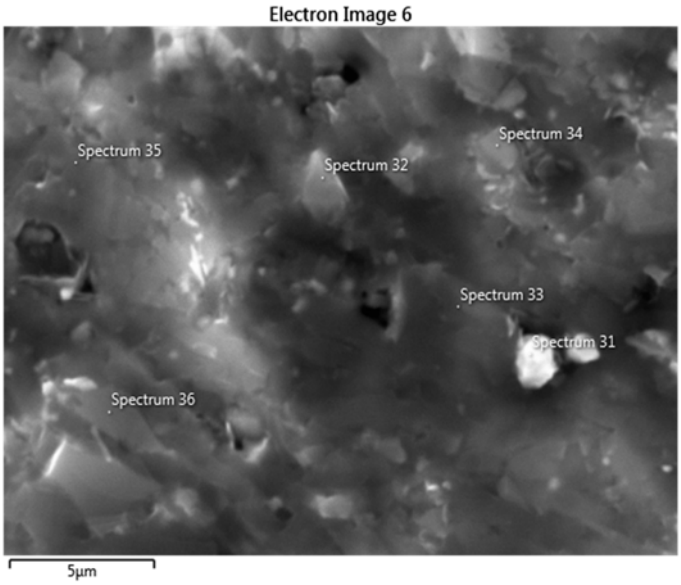

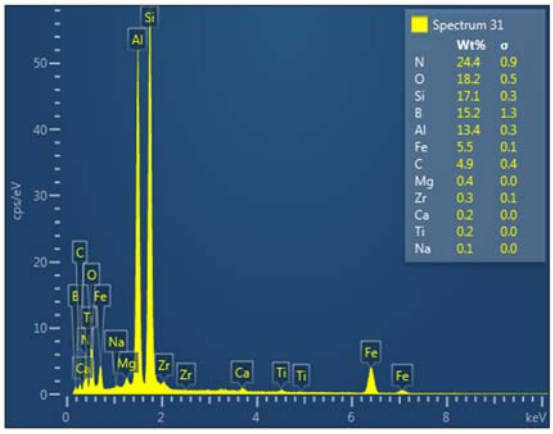

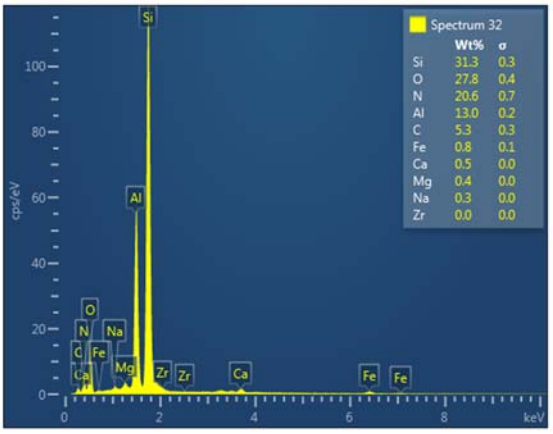

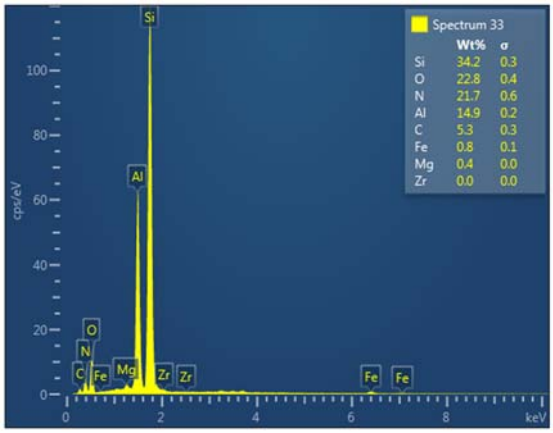

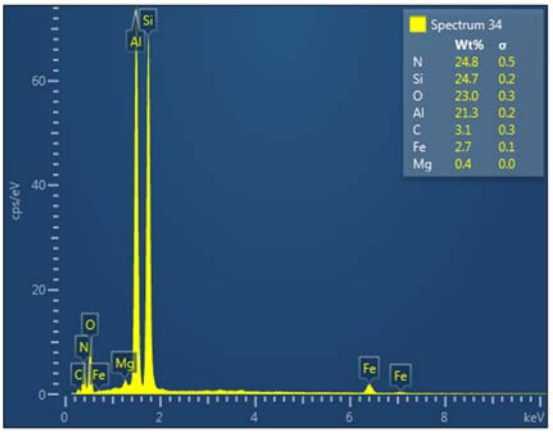

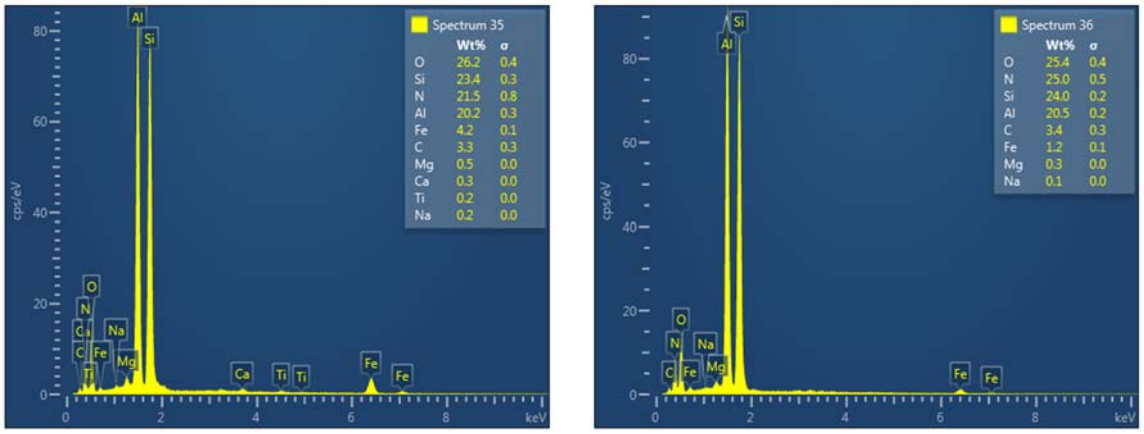

Figure 6. X-ray spectroscopic images of the CH-7 sample.

Electron micrograph 6; six points were analyzed.

Table 5

Elemental composition

Result Type	Weight %					
Spectrum Label	Spectrum 36	Spectrum 31	Spectrum 32	Spectrum 33	Spectrum 34	Spectrum 35
B		15.23				
C	3.42	4.88	5.25	5.28	3.08	3.32
N	25.03	24.44	20.59	21.66	24.79	21.45
O	25.39	18.15	27.82	22.82	23.04	26.19
Na	0.09	0.14	0.34			0.20
Mg	0.35	0.35	0.43	0.36	0.44	0.54
Al	20.50	13.43	12.97	14.87	21.27	20.18
Si	23.99	17.09	31.32	34.20	24.67	23.38
Ca		0.24	0.51			0.29
Ti		0.23				0.20
Fe	1.23	5.49	0.76	0.80	2.71	4.25
Zr		0.34	0.00	0.00		
Total	100.00	100.00	100.00	100.00	100.00	100.00

Statistics	B	C	N	O	Na	Mg	Al	Si	Ca	Ti	Fe	Zr
Max	15.23	5.28	25.03	27.82	0.34	0.54	21.27	34.20	0.51	0.23	5.49	0.34
Min	15.23	3.08	20.59	18.15	0.09	0.35	12.97	17.09	0.24	0.20	0.76	0.00
Average		4.20	22.99	23.90		0.41	17.20	25.78			2.54	
Standard Deviation		1.04	1.97	3.40		0.07	3.84	6.12			1.98	

EDS CH-7 1620^{0}C

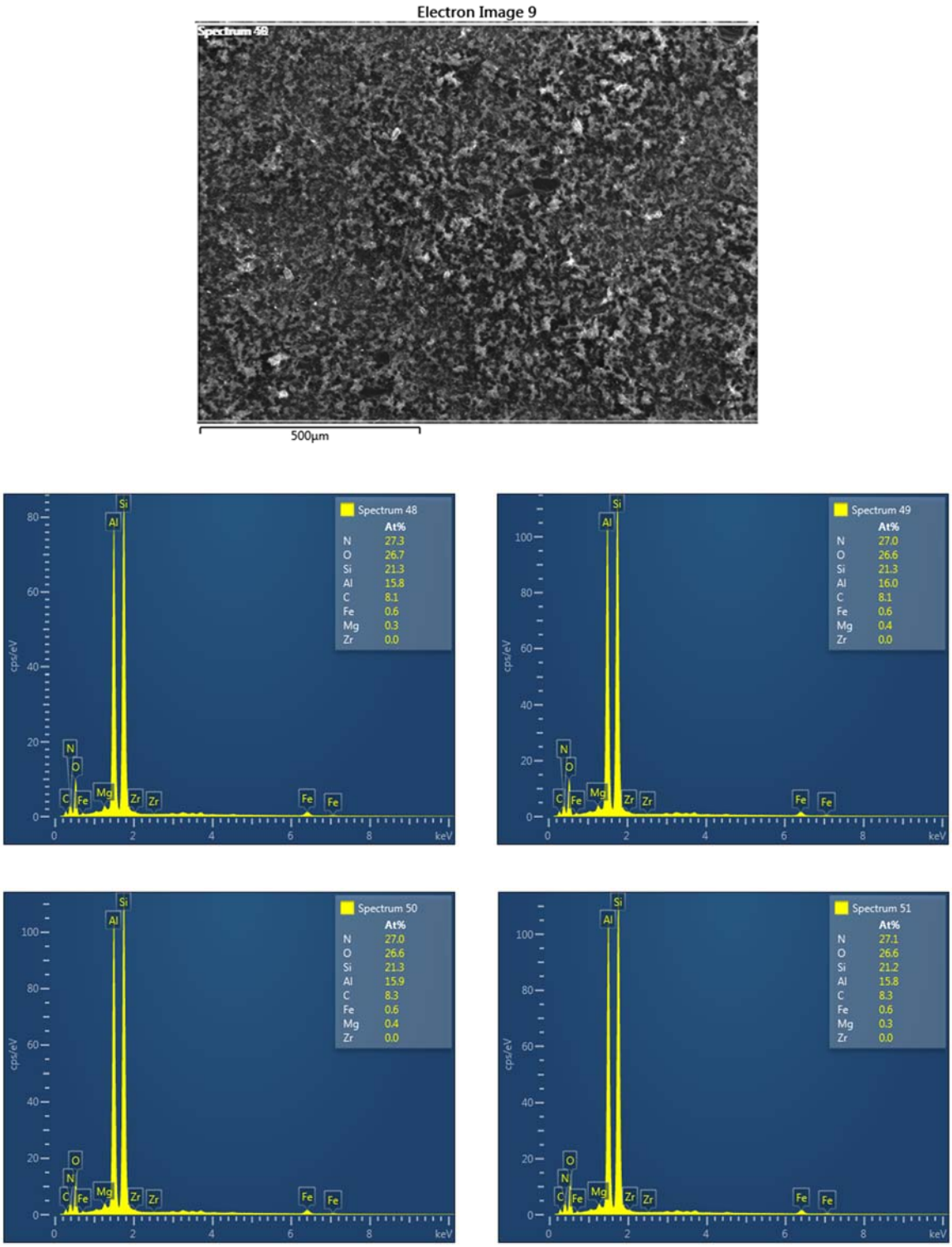

Figure 7. X-ray spectroscopic images of the CH-7 sample.

Electron micrograph 9; four points were analyzed.

Table 6

Elemental composition

Result Type	Atomic %			
Spectrum Label	Spectrum 48	Spectrum 49	Spectrum 50	Spectrum 51
C	8.07	8.13	8.30	8.30
N	27.26	27.02	27.03	27.14
O	26.69	26.64	26.55	26.63
Mg	0.34	0.36	0.35	0.34
Al	15.78	15.96	15.93	15.84
Si	21.31	21.34	21.28	21.21
Fe	0.56	0.55	0.55	0.55
Zr	0.00	0.00	0.00	0.00
Total	100.00	100.00	100.00	100.00

Statistics	C	N	O	Mg	Al	Si	Fe	Zr
Max	8.30	27.26	26.69	0.36	15.96	21.34	0.56	0.00
Min	8.07	27.02	26.55	0.34	15.78	21.21	0.55	0.00
Average	8.20	27.11	26.63	0.35	15.88	21.28	0.55	0.00
Standard Deviation	0.12	0.11	0.06	0.01	0.08	0.06	0.00	0.00

DS CH-7 1620^{0}C

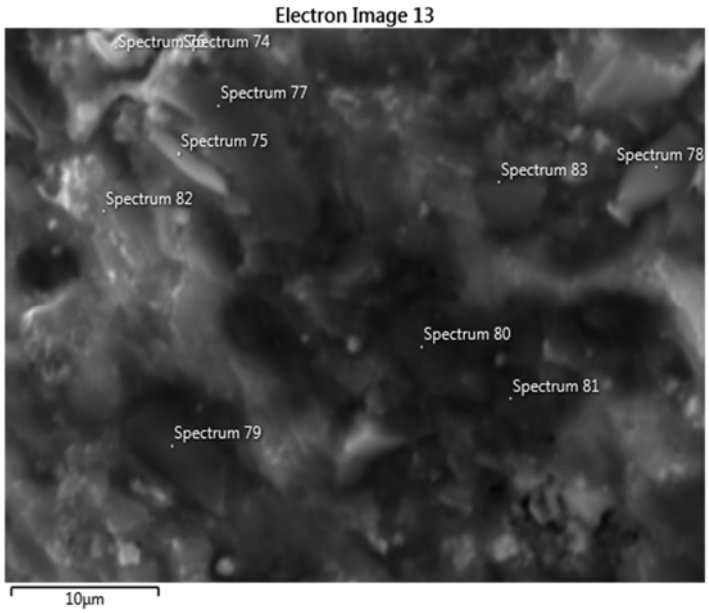

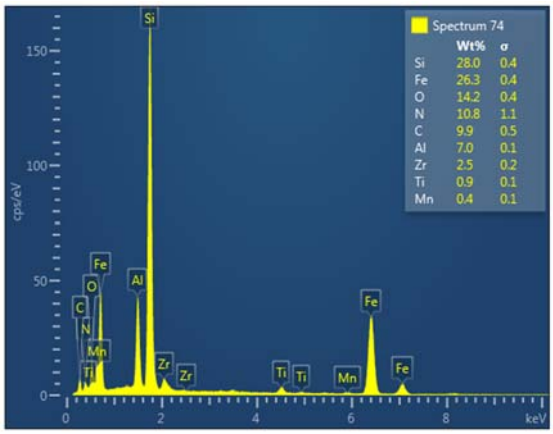

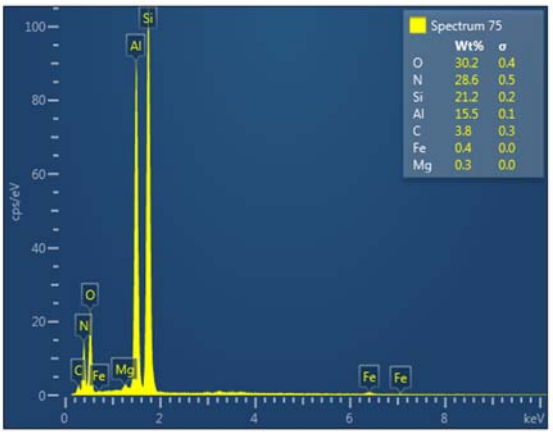

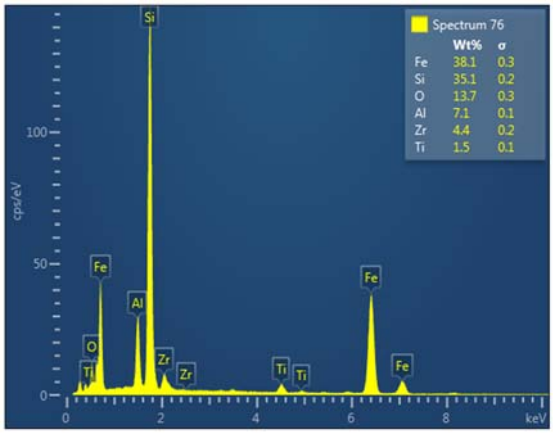

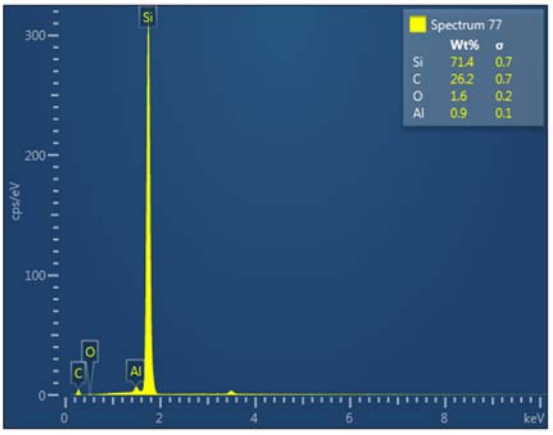

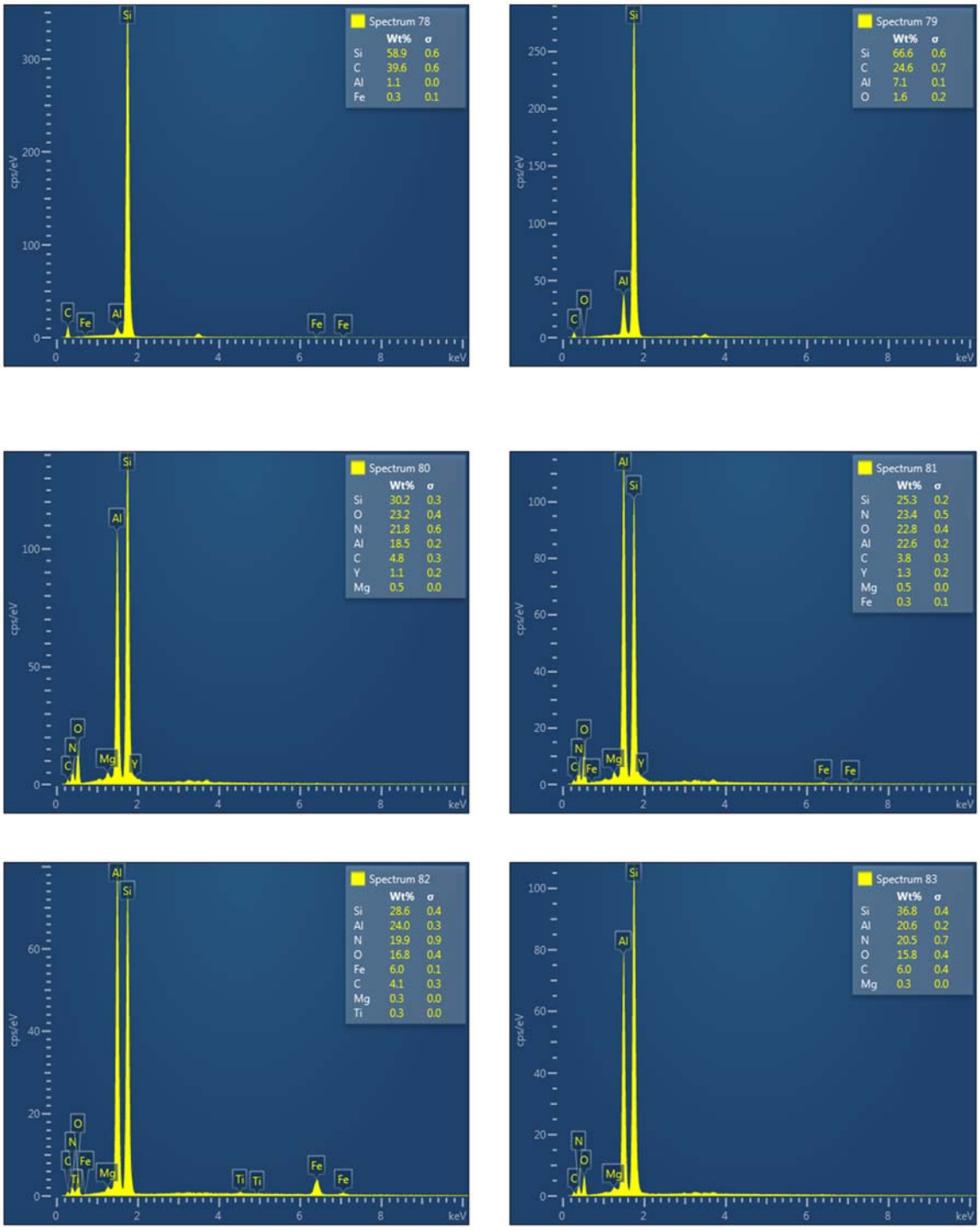

Figure 8. X-ray spectroscopic images of the CH-7 sample.

Electron micrograph 13; ten points were analyzed.

Table 7

Elemental composition

Result Type	Weight %									
Spectrum Label	Spectrum 83	Spectrum 74	Spectrum 75	Spectrum 76	Spectrum 77	Spectrum 78	Spectrum 79	Spectrum 80	Spectrum 81	Spectrum 82
C	5.98	9.90	3.82		26.19	39.64	24.60	4.76	3.77	4.09
N	20.48	10.75	28.59					21.79	23.44	19.87
O	15.80	14.24	30.18	13.70	1.58		1.64	23.18	22.76	16.81
Mg	0.32		0.28					0.51	0.54	0.34
Al	20.59	7.01	15.53	7.09	0.86	1.15	7.13	18.53	22.56	24.00
Si	36.83	28.03	21.17	35.15	71.37	58.92	66.63	30.15	25.31	28.60
Ti		0.94		1.54						0.28
Mn		0.35								
Fe		26.32	0.44	38.09		0.29			0.28	6.00
Y								1.08	1.33	
Zr		2.45		4.43						
Total	100.00	100.00	100.00	100.00	100.00	100.00	100.00	100.00	100.00	100.00

Statistics	C	N	O	Mg	Al	Si	Ti	Mn	Fe	Y	Zr
Max	39.64	28.59	30.18	0.54	24.00	71.37	1.54	0.35	38.09	1.33	4.43
Min	3.77	10.75	1.58	0.28	0.86	21.17	0.28	0.35	0.28	1.08	2.45
Average					12.44	40.21					
Standard Deviation					8.80	18.33					

EDS CH-7 1620^{0}C

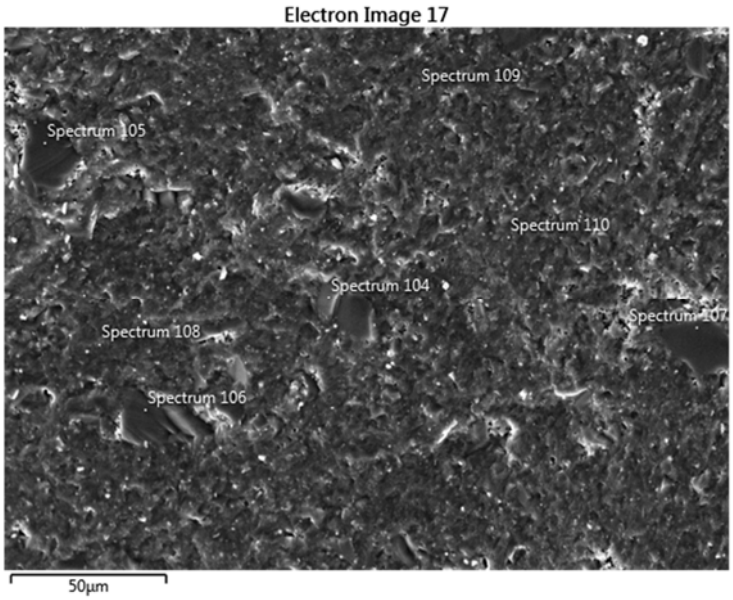

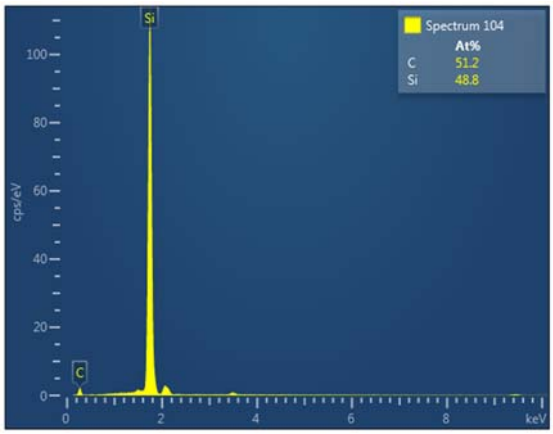

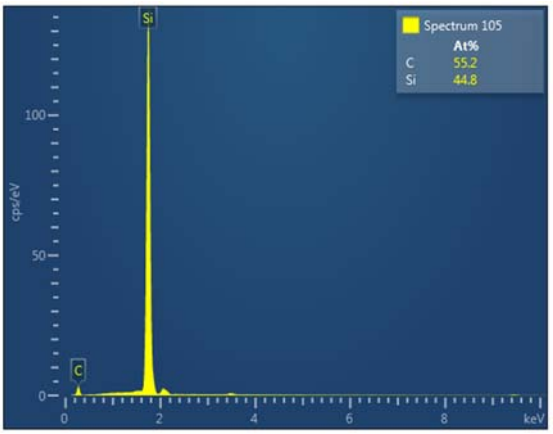

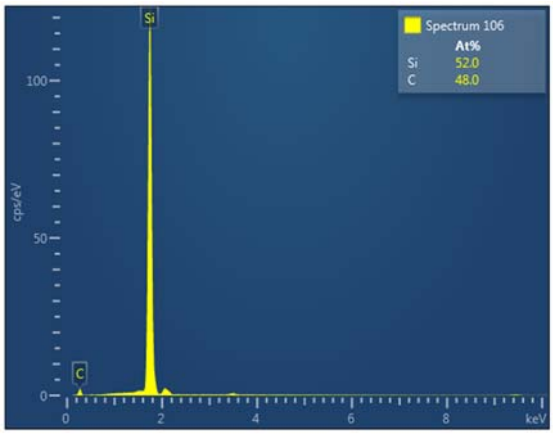

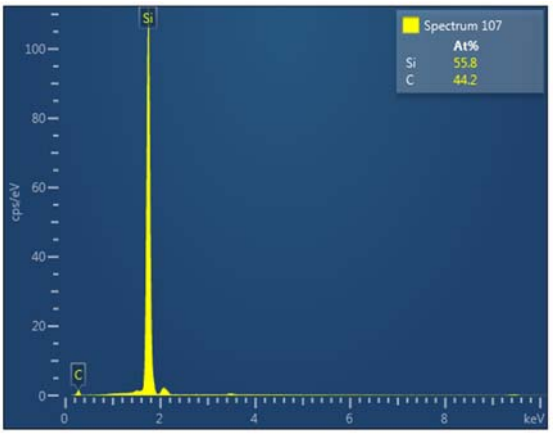

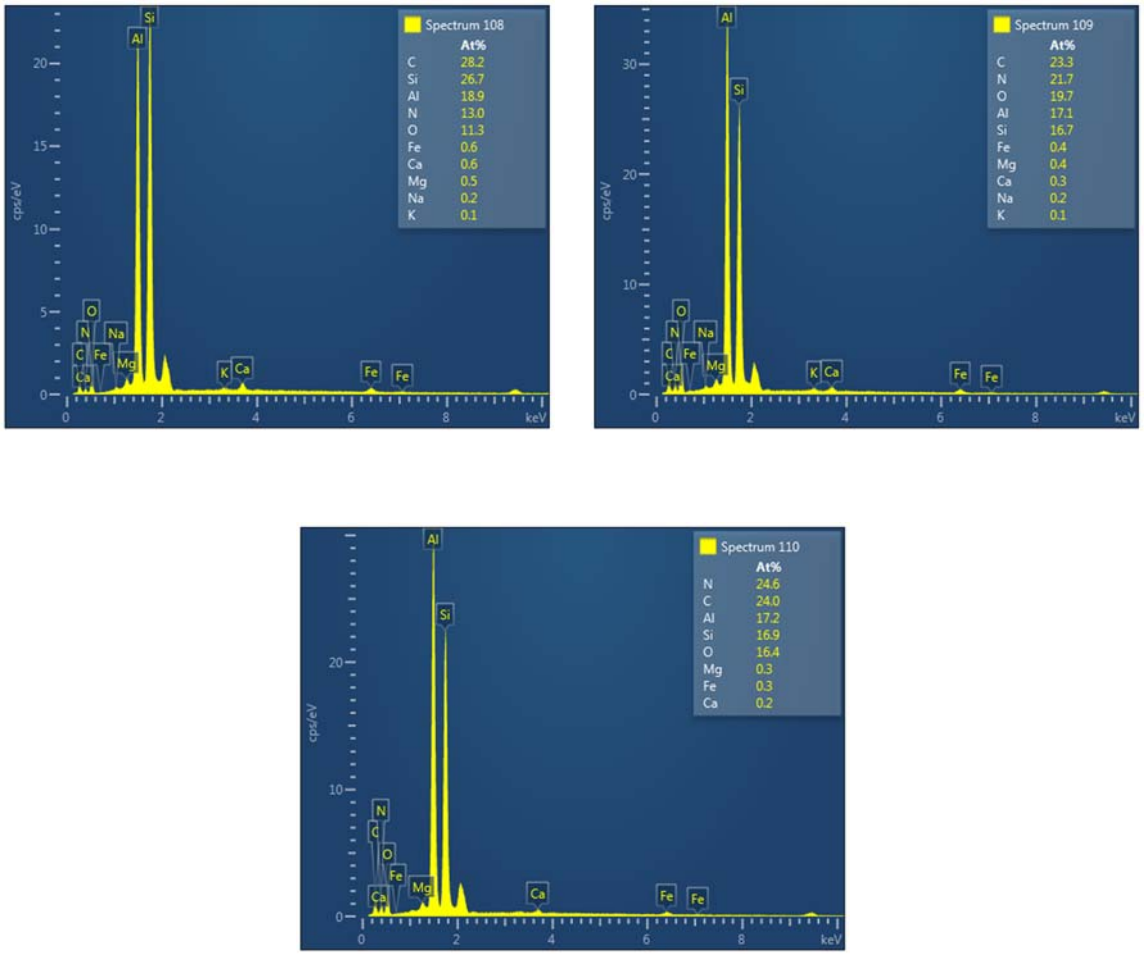

Figure 9. X-ray spectroscopic images of the CH-7 sample.
Electron micrograph 17; seven points were analyzed.

Table 8

Elemental composition

Result Type	Atomic %						
Spectrum Label	Spectrum 110	Spectrum 104	Spectrum 105	Spectrum 106	Spectrum 107	Spectrum 108	Spectrum 109
C	23.99	51.17	55.21	48.04	44.16	28.17	23.34
N	24.58					12.97	21.72
O	16.44					11.28	19.72
Na						0.21	0.22
Mg	0.35					0.51	0.39
Al	17.17					18.86	17.09
Si	16.90	48.83	44.79	51.96	55.84	26.66	16.71
K						0.14	0.13
Ca	0.23					0.59	0.25
Fe	0.33					0.60	0.43
Total	100.00	100.00	100.00	100.00	100.00	100.00	100.00

Statistics	C	N	O	Na	Mg	Al	Si	K	Ca	Fe
Max	55.21	24.58	19.72	0.22	0.51	18.86	55.84	0.14	0.59	0.60
Min	23.34	12.97	11.28	0.21	0.35	17.09	16.71	0.13	0.23	0.33
Average	39.15						37.38			
Standard Deviation	13.58						16.84			

EDS CH-7 1620^{0}C

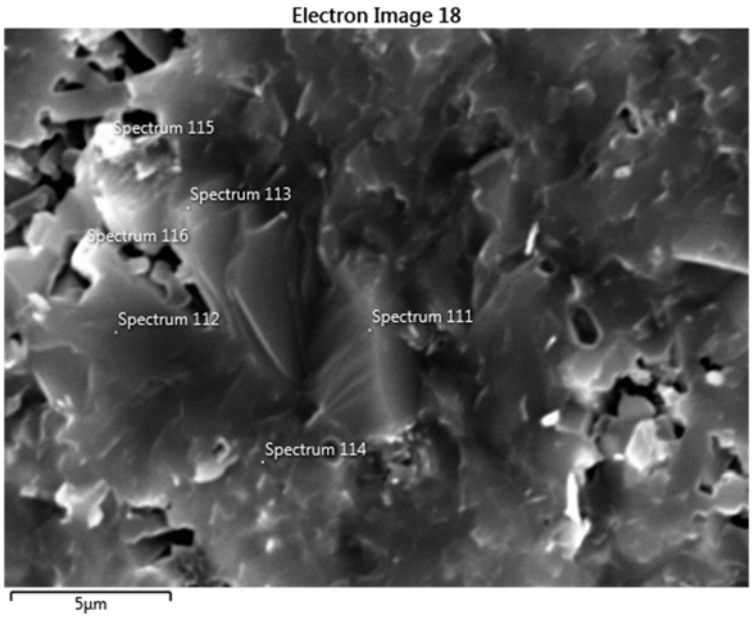

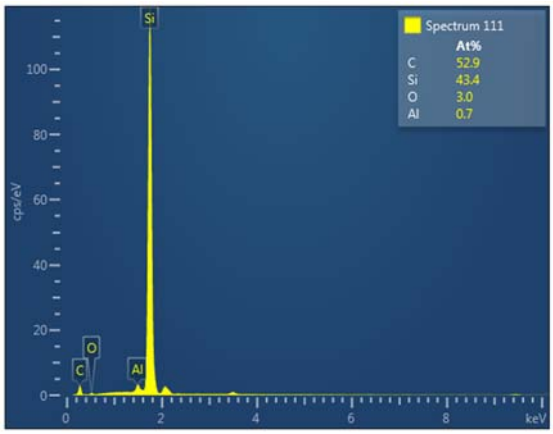

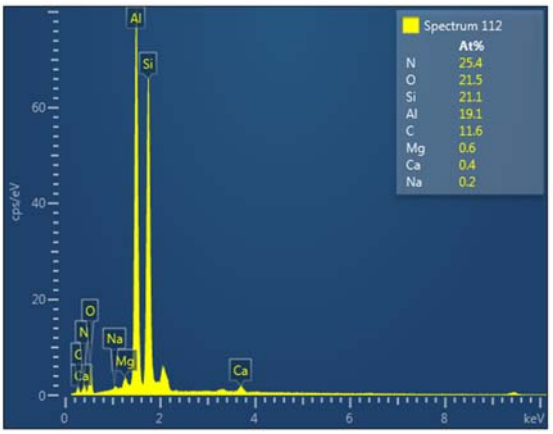

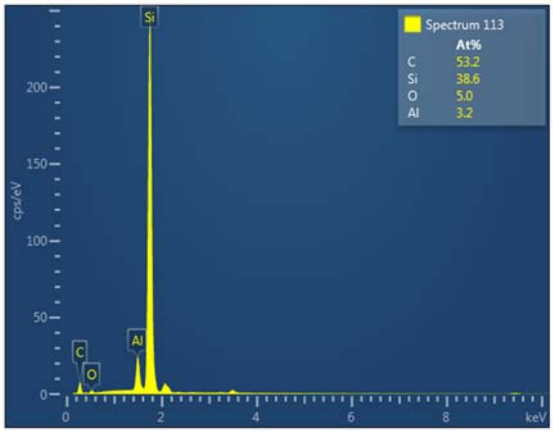

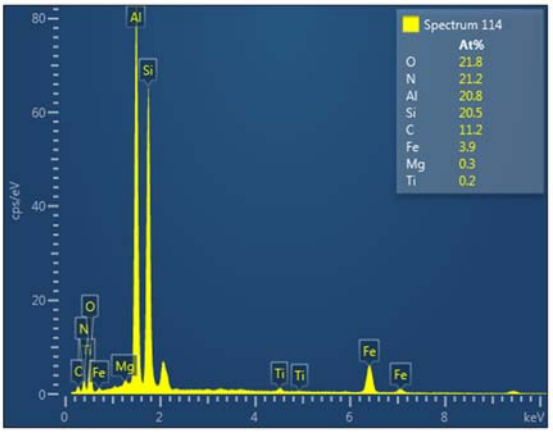

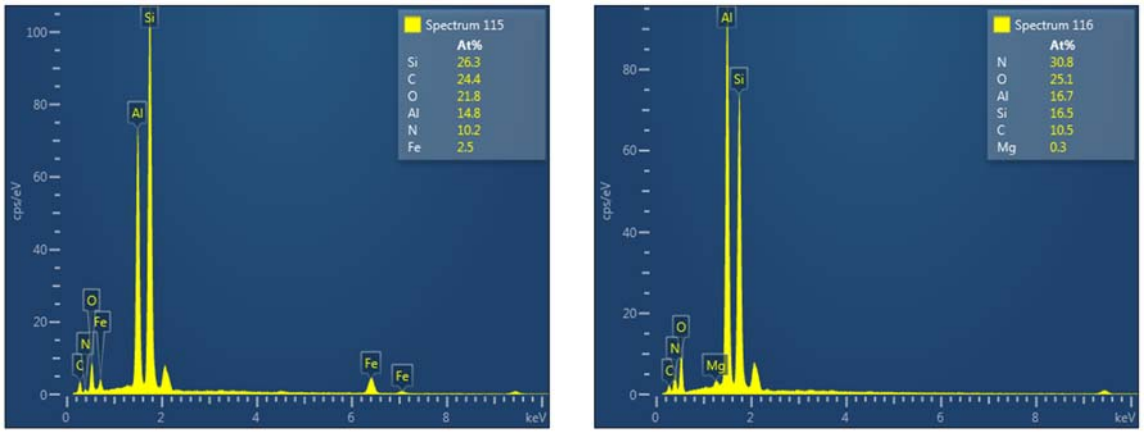

Figure 10. X-ray spectroscopic images of the CH-7 sample.
Electron micrograph 18; six points were analyzed.

Table 9

Elemental composition

Result Type	Atomic %					
Spectrum Label	Spectrum 116	Spectrum 111	Spectrum 112	Spectrum 113	Spectrum 114	Spectrum 115
C	10.55	52.90	11.58	53.22	11.22	24.45
N	30.82		25.41		21.21	10.17
O	25.10	2.98	21.54	4.97	21.81	21.76
Na			0.24			
Mg	0.32		0.57		0.30	
Al	16.68	0.71	19.15	3.22	20.80	14.82
Si	16.53	43.41	21.07	38.59	20.52	26.34
Ca			0.43			
Ti					0.24	
Fe					3.90	2.47
Total	100.00	100.00	100.00	100.00	100.00	100.00

Statistics	C	N	O	Na	Mg	Al	Si	Ca	Ti	Fe
Max	53.22	30.82	25.10	0.24	0.57	20.80	43.41	0.43	0.24	3.90
Min	10.55	10.17	2.98	0.24	0.30	0.71	16.53	0.43	0.24	2.47
Average	27.32		16.36			12.56	27.74			
Standard Deviation	20.60		9.70			8.50	10.84			

The Formula for the Fracture Stress Energy

When discussing the properties of ceramic materials and composites, integrating the concept of fracture stress is a particularly challenging task due to the complex and overlapping processes occurring within the material. Therefore, we deemed it necessary to introduce a characteristic of fracture stress that encompasses all conditions and properties that may arise during the critical loading of a specimen, when failure becomes inevitable. This may occur as a result of external energy input and the consequent accumulation of energy within the specimen, either due to thermostructural changes or the development of external mechanical stresses. The formula for the fracture stress energy, as proposed by Z. Kovziridze [11–13], is as follows:

$$E_{td}=m \cdot a_{c.p.} \quad (1)$$

Where:

- E_{td}– fracture stress energy (energy of tension of decomposition), kJ;
- m– mass of the specimen, g;
- $a_{c.p.}$– crack propagation speed, 2000 m/s.

A rod-shaped test specimen was fabricated from the SiC–SiAlON–Al_2O_3 material, with dimensions: length $l = 110$mm, width $b = 20$mm, and height $a = 10$mm. After firing at 1620 °C, the mass of the rod was 49.3 g. The specimen was fully consolidated, exhibiting nearly zero open porosity.

Assuming that, during the fracture process, the crack propagation velocity depends on the stress intensity factor (critical condition) and lies on the third segment of the v - k curve (Fig. 11), where the velocity increases due to tip separation and reaches approximately 2000 m/s [7], the energy expenditure for fracture stress can be calculated using our formula as follows:

$$E_{td} = 49.3 \text{x} 2000 = 98.6 \text{ kJ}$$

Thus, by establishing a universal relationship between the total energy of the specimen and its mass, we obtain the fracture stress energy formula proposed in this work.

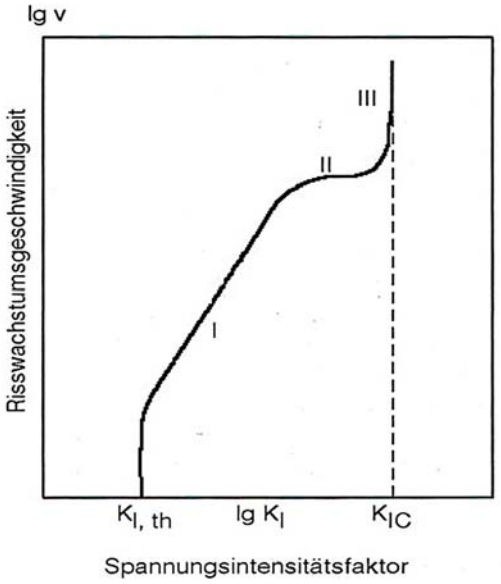

Fig. 11. Typical graph of crack propagation velocity as a function of the stress intensity factor during the development of the pre-critical crack growth state (v–k curve). The horizontal axis represents the stress intensity factor, and the vertical axis represents the crack growth velocity.

Material Fabrication Process and Its Mathematical Modeling

In studying the synthesis processes of the materials, we aimed to theoretically generalize the possible processes occurring in perlite containing a significant amount of glassy phase [14–18], which has a strong influence on the consolidation of the mixture during material fabrication. To this end, we performed a mathematical calculation of the consolidation process and attempted to represent the

physical essence of sialon formation at the early temperature stage, as well as the role of glassy perlite in these complex physicochemical processes.

As is well known, perlite is a volcanic rock consisting of 96 wt.% glassy material, 2–4 wt.% crystallites, and gases (CO_2, CO, N_2, Ar, Cl_2, F_2, and water) in the range of 2–5%. Water accounts for 80–85% of the volatiles, serving as the main foaming agent [19].

As is well known, water in volcanic glasses serves not only as a source of the gaseous phase but also as a mineralizer. It promotes the mobility of the melt generated during thermal treatment [20]. For illustration, Figure 3 shows a variation in the composition of geopolymer and perlite: 50 wt.% geopolymer and 50 wt.% perlite; the melting temperature of perlite is 1240 °C, and that of the geopolymer is 1740 °C. Both components are part of the CH-7 base composition: perlite at 3 wt.% and geopolymer at 18.5 wt.%.

The chemical composition of perlite is as follows (wt.%): SiO_2 – 73.70; Al_2O_3 – 14.06; Fe_2O_3 – 0.84; CaO – 0.70; MgO – 0.45; R_2O – 6.55; SO_3 – 0.20; heat loss – 3.60.

By correlating the description of the settling kinetics with the experimental data, one can consider the case where a liquid phase forms due to the melting of an easily fusible component, under the assumption that the refractory component is partially soluble in the melt. Energetically, the formation of a liquid phase is favored when two particles are separated by the liquid phase while in direct contact. The process requires the following condition:

$$2\alpha_{solid.liquid.} x \cos f < \alpha_2. \quad 2$$

The condition is satisfied for any value of the angle:

$$f = f_0 + 2\theta, \text{if } \alpha_{sl} < \frac{\alpha_2}{2},$$

where $\alpha_{sl}$is the surface energy at the solid–liquid interface, α_2 is the surface energy at the interface between two particles, f_0 is the contact area between the surfaces of two particles at the interface, and θ is the wetting angle [21].

During thermal treatment, the liquid phase formed from the melting of perlite fills the voids in the mixture between the solid SiC and Al_2O_3 particles. The presence of this liquid meniscus under certain conditions generates forces that draw the particles toward one another, thereby promoting densification of the material and influencing the sintering kinetics. This movement is accompanied by a reduction in the free surface area of the liquid phase, which occurs under the influence of pressure arising from surface curvature. Evidently, the mechanism involved is volume diffusion, where the excess vacancies formed near the surface of protruding particle asperities act as sinks at the particle surfaces. In this case, an increase in the contact area must be accompanied by a reduction in the distance between particle centers.

As is well known, volume diffusion is characterized by a high activation energy and predominantly occurs near the Tamman temperature (0.52 Tm, where Tm is the melting temperature in °C). The Tamman temperature corresponds to the onset of atomic or ionic motion in the lattice and is therefore a highly significant parameter when considering interactions between solid bodies.

In the mixture, the Tamman temperature range for the primary mineral of the geopolymer, kaolinite, coincides with the first exothermic peak (925–940 °C), during which its structural layers

undergo significant destruction. For the chemistry of kaolinite ($Al_2O_3 \cdot 2SiO_2 \cdot 2H_2O$), the distribution of bonds within the tetrahedra $[SiO_4]^{4-}$ and octahedra $[AlO_6]^{6-}$ is of fundamental importance. The sp^3 configuration provides stability to the electronic structure of silicon atoms in silicates [22].

However, the manifestation of these bonds within tetrahedral and octahedral units is heterogeneous: p-bonds are significantly stronger than s-bonds, thereby ensuring a relatively prolonged morphological correspondence between the silicate crystal structure and the liquid phase. At such relatively low temperatures, high-temperature components in the mixture, such as SiC and Al_2O_3, do not participate significantly in diffusion processes.

The breaking of bonds, structural fragmentation of the material, and the relatively intense progression of diffusion processes are facilitated within this temperature range by the release of gaseous substances (2–4 wt.%) from perlite [23]. As a result, the p-bonds within tetrahedral and octahedral units are disrupted, the structural Si–O–Al sequence is broken, and Al and Si ions are released, creating the conditions for their diffusion in the melt. Due to the structural degradation, viscosity decreases significantly.

Simultaneously, the minerals in the raw mixture undergo decomposition, accompanied by the release of water vapor and other gaseous products. At this stage, internal molecular transformations occur within the primary geopolymer mineral kaolinite, including the cleavage of hydrogen bonds (H_2O and OH^-), while the release of water from perlite partially delays the formation of crystalline nuclei from Al_2O_3 and SiO_2 particles. This process shifts to higher temperatures.

Following this temperature interval, intensive interactions occur between the geopolymer and perlite, which are significantly facilitated by the shift of the endothermic peak of perlite to the right (1000–1050 °C; Fig. 12). Being a readily fusible component, it accelerates the formation of a liquid phase and, in combination with perlite, excess amorphous silicon dioxide, and decomposition products of kaolinitic geopolymer, leads to the formation of a perlite–glass melt. According to our calculations, the content of this melt in the final product is 7.4 wt.% [23].

Within the perlite and glassy liquid phase, two main refractory oxides, SiO_2 and Al_2O_3, undergo energetic interactions.

This results in the formation of a compound that crystallizes from the melt into new crystalline formations - mullite ($3Al_2O_3 \cdot 2SiO_2$). While this would seemingly contribute to the creation of the material's skeleton within the mixture, the physico-chemical transformations proceed differently due to the formation of sialon at 1250–1300 °C.

Only after these temperatures, when the free SiO_2 and Al_2O_3 particles, whose chemical bonds are absent due to the prior decomposition of kaolinit, are in a relatively high-energy, chemically active state, does the chemical reaction forming mullite proceed at an increased rate, thereby promoting the nucleation of crystals (Fig. 12).

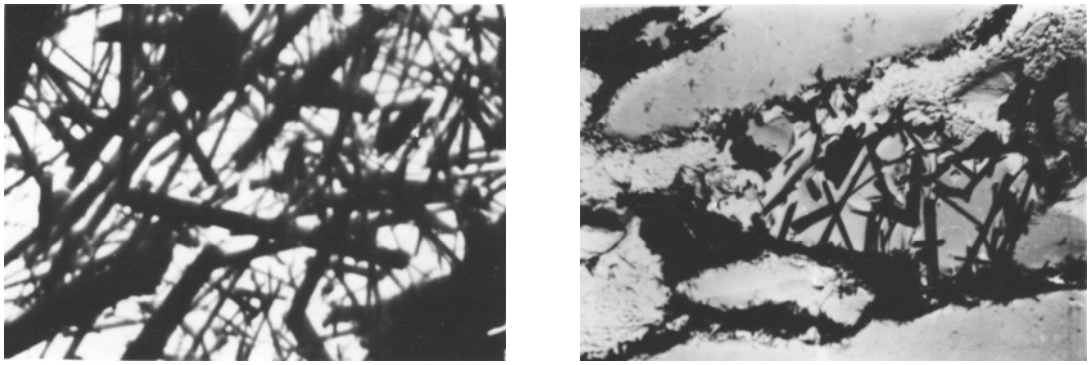

a b

Figure 12. Fragment of ceramic material – clay–perlite (50:50 wt.%), sintered at 1050 °C. (a) Network of large needle-like mullite crystals; (b) Glassy phase reinforced with fine needle-like mullite crystals, X 5400.

The resulting liquid phase hinders the release of volatile components from perlite by entraining the particles within the liquid layer. As the temperature increases, the pressure in the closed pores rises, causing them to expand and release gases from the material. The degassing of perlite begins above 860 °C, coinciding with the first exothermic peak of kaolinite. Due to the overlap of these processes, degassing continues and becomes more pronounced at higher temperatures, in the range of 1000–1050 °C. The process shifts from shrinkage to apparent "growth," as observed in the specimens (Figs. 13–14). This phenomenon significantly contradicts the conventional laws of shrinkage; however, we believe that the processes occurring within this temperature interval exert a decisive influence on the densification of the ceramic material. This is because water, acting both as a gas-forming and fluxing agent, is released during thermal treatment and exhibits a mineralizing effect. It leads to loosening of the ceramic structure and, overall, to a weakening of the crystalline framework, resulting in a reduction in the viscosity of the silicate melt. This, in turn, promotes the full and intensive development of diffusion processes [21, 23].

Figure 13. Thermogram of perlite

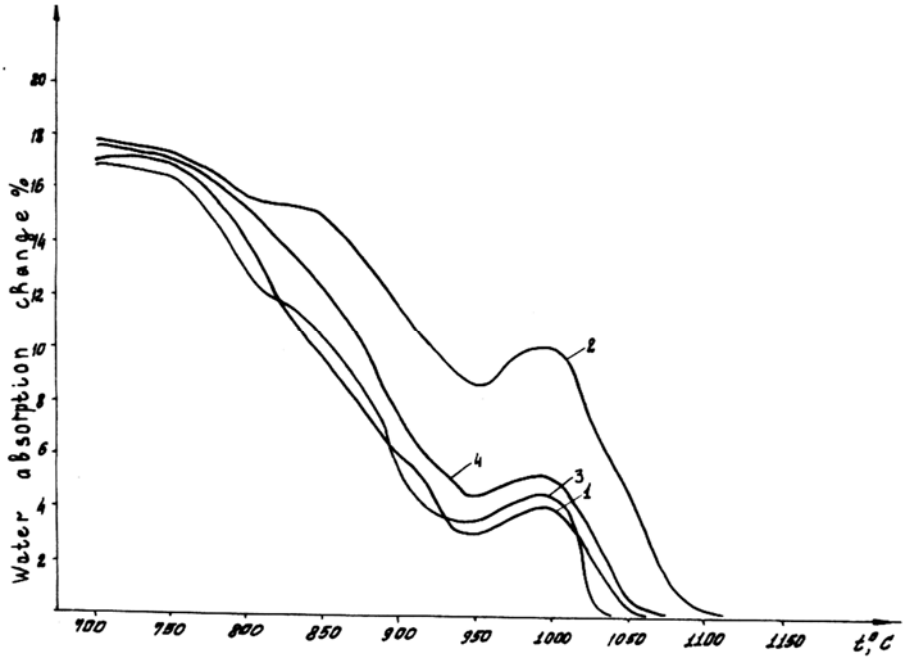

Figure 14. Temperature-dependent changes in water absorption of ceramic materials. Compositional variations (wt.%): fireclay 50–35, perlite 50–65.

Figure 12 shows that the formation of mullite crystals becomes possible already at temperatures of 1050–1100 °C. However, in the CN-7 composition, due to the occurrence of complex physicochemical processes and the overlap of several reactions, mullite crystals cannot yet be considered fully developed, since the Si–O–Al bonds are not sufficiently strong at this stage. Within this temperature range, the release of water and gases from perlite (Fig. 14), which leads to structural loosening, hinders the structural formation of mullite crystals.

The formation of silicon nitride begins at approximately 1250 °C and consumes the oxides associated with mullite. The viscosity of the melt decreases to approximately 10^7–10^9 Poise [24–34], and the action of surface forces at phase boundaries becomes more pronounced. As a result, crystalline grains approach one another, the material densifies, and water absorption decreases in accordance with the reduction in porosity. The material thus acquires high functional (service) properties, as confirmed by experimental studies [23].

When considering sintering kinetics, it is important to account for cases in which solid particles are partially or completely soluble in the liquid layer between grains. This phenomenon is confirmed by structural investigations, which reveal partially melted grains of quartz and perlite. The finer particles of the latter are completely molten and assimilated into the bulk matrix. Thus, several physicochemical processes characteristic of solid–liquid-phase sintering occur simultaneously.

In this case, the interaction forces between grains are governed by:

1. the presence of curvature of the liquid surface

$$F_1 = a_e(1/r_1 - 1/r)S; \quad 9$$

2. the tendency of the free surface of the liquid component to decrease, which is independent of its curvature

$$F_2 = La_{eo}\Psi(V,\theta)\,, \quad 10$$

where L is the length of the wetting perimeter, and $\Psi(V,\theta)$ is a function dependent on the wetting contact angle θ, the volume of liquid confined between the grains, and V, which characterizes the geometry of the grains. For spherical grains, the radius R is given by:

$$S = \pi R^2 \sin 2f\,; \quad 3$$

$$\Psi(V,\theta) = \sin x \sin(f+\theta)\,; \quad 4$$

$$F = F^1 + F^2 = a_{eo}[\pi R^2 \sin^2 f(\tfrac{1}{r_1} + 1/r) + 2\pi r \sin f x sin(f+\theta), \quad 5$$

Where:

$$r_1 = R\sin f - [R(1-\cos f)\lambda/2]1 - \sin(\theta + f); \quad 6$$

$$R = 2R(1-\cos f) + \lambda/2/2\cos(f+\theta)\,, \quad 7$$

where $\lambda$is the gap between the grains.

The formula is valid under the assumption that distortions of the liquid meniscus caused by gravity can be neglected. Above the optimal temperature range, the wetting angle reaches a critical value:

$$\Theta = \pi - f/2\,. \quad 8$$

The attractive force between the grains becomes neutralized, and in the presence of a substantial amount of liquid phase, a repulsive force arises that drives the grains apart. This, in turn, creates conditions for material deformation and a deterioration of its technical properties. Such effects were observed in laboratory experiments during the firing of specimens under hot-pressing conditions at temperatures above 1620 °C, when the leaching of aluminum oxide from the material occurred.

Based on the considerations presented above, we developed a mathematical calculation for the consolidation process of materials in cases where solid–liquid-phase sintering occurs with a liquid-phase content of 7.4 wt.%. Considering that sintering processes in materials of this composition begin above 1050 °C due to the formation of a certain amount of liquid phase, we recommend terminating hot-press firing at the early stage of densification, i.e., at 1620 °C, rather than waiting for complete elimination of open porosity. This is particularly reasonable since the material, even with 0.18 % residual porosity, exhibits high functional properties.

Furthermore, the coexistence of oxygen-free and oxidized compounds in the composition is complex and can lead to incompatibilities. Due to the wide melting range of perlite and the high viscosity of the resulting melt, the ceramic specimen does not deform during the firing stage. As a result, at temperatures of 1250–1300 °C, sialon formation proceeds more intensively in the geopolymer–perlite composition, facilitated by the processes that occurred at 1000–1050 °C.

The formation of sialon is a highly intensive physicochemical process, promoted in this temperature interval by relatively high nitrogen pressure and metallothermic effects. The sialon formed consumes the mullite oxides generated during internal molecular transformations of the geopolymer, so that at high synthesis temperatures (1620 °C), mullite is no longer present in the phase composition. Sialon thus becomes the dominant phase in the structure, comprising 57 wt.%, while SiC accounts for 27 wt.% and Al_2O_3 for 5.7 wt.%.

3. Conclusion

Thus, the presence of a certain amount of finely dispersed aluminum oxide nanoparticles, which reinforces the material, combined with 7.4 wt.% of glassy phase formed by perlite in the geopolymer–perlite composition, which facilitates grain attraction, binding, and the formation of a glassy nano-layer on their surfaces, together with the covalently bonded silicon carbide and the 57 wt.% content of sheet-like sialon, clearly observed in electron microscopy images, contributes to the enhancement of the mechanical properties of the composite.

Optimal quartz grain sizes, the low solubility of these grains, which promotes the development of tangential stresses, the high silicon content in perlite (~74 wt.%), and the proportion of aluminum oxide in the acidic glassy phase all favor the formation of Si–O–Al bonds. These factors, in our view, underlie the material's high functional properties.

Chemical resistance is 99.9 % to water and 98.7 % to 35 % NaOH. Mechanical properties include flexural strength of 470 MPa and compressive strength of 1910 MPa. The firing temperature is 1620 °C, with water absorption of 0.18 %.

References

1. Kovziridze, Z., Aneli, J., & Sarukhanishvili, A. (2008). *Resistance of materials to aggressive media* (pp. 51–99). Tbilisi, Georgia: Georgian Technical University.
2. Kovziridze, Z., Aneli, J., Nijaradze, N., & Tabatadze, G. (2017). *Ceramic and polymer composites* (pp. 119–209). Saarbrücken, Germany: Lambert Academic Publishing.
3. Friedrich, K. M. (1987). Produktionsverfahren, Anwendungseigenschaften und Einsatzmöglichkeiten von Nitridkeramik, insbesondere von Siliciumnitrid. *Vortragsveröffentlichungen Haus Technische Universität Essen*, (#519), 19–21.
4. Wang, L., He, C., & Wu, J. (1989). Oxidation of sintered silicon nitride materials. In *Ceramic Materials and Components for Engines: Proceedings of the International Symposium* (pp. 604–611). Westerville, OH.
5. Zheng, G., Zhao, J., Gao, Z., & Cao, Q. (2012). Cutting performance and wear mechanisms of SiAlON–Si_3N_4 graded nanocomposite ceramic cutting tools. *The International Journal of Advanced Manufacturing Technology, 58*(1–4), 19–38.
6. Riley, F. L. (2000). Silicon nitride and related materials. *Journal of the American Ceramic Society, 83*(2), 245–265.
7. Shvedkov, E. L., et al. (1991). *Dictionary and reference book on new ceramics* (pp. 183, 269–271). Kyiv, Ukraine: Naukova Dumka.
8. Kovziridze, Z., Nijaradze, N., Tabatadze, G., Cheishvili, T., Mestvirishvili, Z., Mshvildadze, M., & Darakhvelidze, N. (2017). Composite synthesis by metallothermic and nitriding processes in the Si–SiC–Al geopolymer system. *Ceramics and Advanced Technologies, 19* (2), 33–52.
9. Kovziridze, Z., Nijaradze, N., Tabatadze, G., Cheishvili, T., Mestvirishvili, Z., Mshvildadze, M., Nikoleishvili, E., & Darakhvelidze, N. (2014). Formation of sialon by nitro-aluminothermic processes. *Ceramics, 2*(32), 23–32.

10. Budworth, D. W. (1970). Theory of pore closure during sintering. *Transactions of the British Ceramic Society, 69*, 29–31.
11. Kovziridze, Z. (2019). Failure stress energy formula. In *Abstract Book of the XVI ECERS Conference and Exhibition of the European Ceramic Society* (p. 670). Turin, Italy.
12. Kovziridze, Z. (2018). Failure stress energy formula. Journal of Electronics Cooling and Thermal Control, 8(3), 31–47. https://www.scirp.org
13. Kovziridze, Z. (2018). Failure stress energy formula. Ceramics and Advanced Technologies, 20(1), 11–23.
14. Kovziridze, Z., Hennicke, H. W., & Kharitonov, F. (1998). *Thermomechanics of ceramics* (pp. 30–41). Karlsruhe, Germany: Hochschule für Technik.
15. Kovziridze, Z. (2018). Formula of the thermogradient effect. Journal of Electronics Cooling and Thermal Control, 8(4). https://doi.org/10.4236/jectc.2018.84004
16. Ross, G. S., & Smith, R. H. (1955). Water and other volatiles in volcanic glasses. American Mineralogist, 40(11–12), 1071–1083.
17. Kovziridze, Z. (2020). Dependence of mechanical characteristics of materials on crystalline phase composition of the matrix. Advances in Materials Physics and Chemistry, 10(8). https://doi.org/10.4236/ampc.2020.108013
18. Budnikov, P. P., & Gevorkyan, H. O. (1952). On the role of feldspar in the formation of porcelain structure. Glass and Ceramics, 3, 19–20.
19. Polinkovskaya, A. I., Sergeev, N. I., & Chernova, O. A. (1971). Expanded perlite as an aggregate for lightweight concretes (pp. 22–30). Moscow, USSR: Construction Literature Publishing House.
20. Belyankin, D. S. (1928). On water in magmas and magmatic rocks. Geological Bulletin, 6(1–3), 19–27.
21. Avgustinik, A. I. (1957). *Ceramics* (pp. 4–24). Leningrad, USSR: Stroiizdat.
22. Gaprindashvili, G.G., Kharitonov, F. Ya., & Kovziridze, Z. D. (1998). Processes occurring during thermal treatment of low-temperature ceramics. Tbilisi, Georgia: Georgian Technical University.
23. Volarovich, M. P., & Leontieva, A. L. (1937). Investigation of obsidian viscosity in relation to the genesis of pumice. *Doklady Akademii Nauk SSSR, 17*(8), 419–421.
24. Hennicke, H.W., Kharitonov, F.Ya., & Kovziridze, Z. D. (1992). *Barium-containing electroceramics resistant to thermal shock*. Tbilisi, Georgia: Tbilisi Technical University.
25. Yavits, P. N. (1962). Studies of viscosity and fusibility of water-containing volcanic glasses. *Proceedings of ROSNIIMS, 25*, 54–63.
26. Ross, G. S., & Smith, R. H. (1955). Water and other volatiles in volcanic glasses. *American Mineralogist, 40*(11–12), 1071–1083.
27. Polinkovskaya, A. I., Sergeev, N. I., & Chernova, O. A. (1971). *Expanded perlite as an aggregate for lightweight concrete* (pp. 22–30). Moscow, USSR: Construction Literature Publishing House.
28. Belyankin, D. S. (1928). On water in magmas and magmatic rocks. *Geological Bulletin, 6*(1–3), 19–27.
29. Budnikov, P. P., & Gevorkyan, H. O. (1972). *Firing of porcelain* (pp. 12–22). Moscow, USSR: Stroiizdat.

30. Budnikov, P. P., & Gevorkyan, H. O. (1952). On the role of feldspar in the formation of porcelain structure. *Glass and Ceramics, 3*, 19–20.
31. Brindley, G. W., & Kinstzy, H. A. (1924). *Journal of the American Ceramic Society, 44*(10)
32. Kalinina, A. M., & Filipovich, V. N. (1963). On the nature of thermal transformations of kaolinite and aluminosilicate gels. In *Silicates and oxides at high temperatures* (pp. 81–95). Moscow, USSR: Academy of Sciences of the USSR.
33. Geguzin, I. E. (1967). *Physics of sintering* (pp. 55–58, 130–141). Moscow, USSR: Nauka.
34. Manuilova, N. S., Stolovitskaya, M. M., & Weber, S. N. (1962). Influence of structure and texture of perlite rocks on their expandability. *Proceedings of ROSNIIMS, 25*, 45–54.

უაკ 666.762.93

მაღალი სიმძლავრის ჰეტერომოდულური ნანოკომპოზიტის მიღება და კვლევა ჟანგბადიანი და უჟანგბადო ნაერთების სისტემაში.

ზ. კოვზირიძე, თ. ლოლაძე ნ. ნიჟარაძე, გ. ტაბატაძე, ნ. დარახველიძე, მ. ბალახაშვილი

ბიონანოკერამიკისა და ნანოკომპოზიტების ტექნოლოგიის ინსტიტუტი. საქართველოს ტექნიკური უნივერსიტეტი. საქართველო. 0175, თბილისი, კოსტავას 69

E-mail: kowsiri@gtu.ge

რეზიუმე: ***მიზანი.*** მაღალი სიმძლავრის ჰეტერომოდულური ნანოკომპოზიტის მიღება SiC-SiAlON-Al_2O_3 სისტემაში: ჯავშანტექნიკის, ავიაციისა და რაკეტული ტექნიკისათვის, რეაქტიული ძრავებისა და მაღალტემპერატურული აირადი ტურბინების დეტალებისათვის.

მეთოდი. მეტალოთერმული პროცესით ტექნიკური აზოტის მედიაში, რეაქციული შეცხობის მეთოდით, მიღებულია კომპოზიტი 15% ღია ფორიანობით. მასალა გადამუშავდა ბურთულებიან წისქვილში 10 საათის განმავლობაში, შემდეგ 10 წუთი ატრიტორში 1–3 მკმ ზომის დისპერსიულობამდე, ცხელი წნეხით მაღალი სიმკვრივისა და საექსპლუატაციო თვისებების მქონე პროდუქტი 1620^{0}C-ზე სინთეზირდა.

შედეგი. β-SiAlON-ის წარმოქმნას რეაქციული შეცხობით ასეთ დაბალ ტემპერატურებზე (ნაცვლად 1800^{0}C-სა) ხელს უწყობს როგორც საწყისი ნედლეულის – ალუმინის, სილიციუმის, SiC-ს, გეოპოლიმერისა და პერლიტის კომპოზიცია, ისე მინისებრი პერლიტიდან წყლისა და აირების დეჰიდრატაციის და დეაერაციის პროცესის 860^{0}C-ის ნაცვლად, როგორც ეს პერლიტის თერმოგრამაზე ფიქსირდება, შედარებით მაღალ –1000–1050^{0}C ტემპერატურებზე გადანაცვლება, რაც

სტრუქტურას აფაშრებს და დიფუზურ პროცესს აქტიურს ხდის. შედეგად, უკვე 1250–1300^{0}C ტემპერატურებიდან სიალონის წარმოქმნა უფრო ინტენსიურად მიმდინარეობს, გეოპოლიმერ-პერლიტის კომპოზიციაში 1000–1050^{0}C-ზე განვითარებული პროცესების გამო. სიალონის წარმოქმნა იმდენად ძლიერი ფიზიკურ-ქიმიური პროცესია, რასაც ხელს უწყობს ამ ტემპერატურულ ინტერვალში აზოტირების შედარებით მაღალი წნევა და მეტალოთერმია, რომ წარმოქმნილი სიალონი მოიხმარს გეოპოლიმერის შიგა მოლეკულური გარდაქმნების შედეგად წარმოქმნილ მულიტის ოქსიდებს და მაღალ ტემპერატურებზე სინთეზისას, 1620^{0}C-ზე, ფაზურ შედგენილობაში მულიტი აღარ გვხვდება. სიალონი ხდება უპირატესი ფაზა სტრუქტურაში – 57მას.%.

დასკვნა. პროცესის განვითარებას ხელს უწყობს მინისებრი დოპანტ-არაგაცის პერლიტის გამოყენება, რომელიც გეოპოლიმერთან ევტექტიკით დაბალ ტემპერატურებზე კარგ წი-ნაპირობას ქმნის დიფუზური პროცესების ინტენსიურად წარმართვისათვის სხვა დანარჩენ კომპონენტებთანაც. ნაშრომში წარმოდგენილია ელექტრონულ-მიკროსკოპული, რენტგენო-სტრუქტურული და რენტგენოსპექტრული ანალიზების შედეგები, ფიზიკურ-ქიმიური პრო-ცესების მათემატიკური გათვლები, რამაც დაადასტურა ჩვენი თეორიული დასკვნები პრაქ-ტიკული ექსპერიმენტების საფუძველზე.

საკვანძო სიტყვები: კომპოზიტი; ცხელი წნეხა; სტრუქტურა; ფაზური შედგენილობა, მაღალი სიმძლავრის ჰეტერომოდულური.

UDC 666.3

STUDY OF THE POSSIBILITY OF OBTAINING REFRACTORY CERAMIC MATERIALS FROM KAOLINIZED CLAYS OF GEORGIA

T. Petriashvili, E. Shapakidze, I. Kamushadze, L. Gabunia, I. Gejadze, M. Makadze

Ivane Javakhishvili Tbilisi State University, Alexander Tvalchrelidze Caucasian Institute of Mineral Resources. 11 Mindeli str., 0186, Tbilisi, Georgia

E-mail: t.petriashvili25@gmail.com, elena.shapakidze@tsu.ge

Resume: ***Goal.*** The aim of this work is to study kaolinized clays in Georgia and develop a technology for the production of refractory ceramic materials based on them.

Method. Chemical and petrographic analysis methods and physical and mechanical testing were used.

The mineral composition of clays was determined using an Optika B-383POL polarization microscope (Italy).

Physical, mechanical and thermal tests of the developed ceramic materials were carried out on cubes measuring 40x40x40 mm and tiles measuring 50x50x10 mm.

Results. A process technology for producing refractory ceramic materials has been developed, and the key technical and operational parameters have been studied.

Conclusion. Based on the results of the research, it can be concluded that refractory ceramic materials can be produced using kaolinized clays from the *Qobuleti*, *Makhinjauri*, *Brili*, and *Makvaneti* deposits in Georgia.

A process technology for producing refractory ceramic materials has been developed, and the key technical and operational parameters have been studied. The optimal firing temperature has been established at 1200°C.

The developed materials are suitable for use as linings in heating units. They can also be used to manufacture products such as façade (clinker) bricks and tiles for wall and road cladding, as well as chemically resistant tiles.

Key words: kaolinized clay, kaolin, refractory ceramic material, ceramics.

1. INTRODUCTION

More than 4.1–4.6 billion tons of cement are produced globally each year [1], accounting for around 8% of global carbon dioxide emissions, more than all the world's trucks combined, making decarbonization of the cement industry critical to achieving global climate goals.

The primary material for the modern construction industry is cement/concrete, the production of which is associated with high energy and material costs and, most importantly, high CO_2 emissions. Therefore, the development of new energy-efficient building materials as alternatives to Portland cement is of great importance [2].

One way to address this problem could be to make greater use of ceramic building materials, which require less energy to produce and are not

associated with high CO_2 emissions than Portland cement.

For the production of ceramic materials, firing at a temperature of 900-1200°C is required, while for the synthesis of cement clinker - 1450-1500°C.

Conventional construction ceramic materials (bricks, blocks, tiles) are made from low-melting clays (deposits of Metekhi, Sagarejo, Miriani, Gardabani) with an Al_20_3 content of 10-15%. These materials do not withstand high temperatures: 1350°C and above begin to melt and deform. The use of such materials in thermal units or aggressive environments is not allowed. To obtain refractory ceramic materials, it is necessary to use clays with high Al_20_3 content (20-25%), which allows kaolinized clays. Kaolin clays belong to refractory clays. Their melting point is in the range of 1350-1580°C, and they can be used to produce materials such as linings for thermal units, chemically resistant tiles, etc. [3, 4].

There are no deposits of kaolin clays in Georgia, but there are kaolinized clays containing 20-25% Al_2O_3.

Kaolinized clays can also be considered refractory, since their melting temperature ranges from 1350-1580°C, i.e. they can be used to produce materials such as linings for heating units, facade (clinker) bricks and tiles for wall and road cladding, and chemically resistant tiles.

The main mineral of kaolin is the mineral Kaolinite with the theoretical formula $Al_2O_3 \cdot 2SiO_2 \cdot 2H_2O$ or $Al_2Si_2O_5(OH)_4$ with a 1:1 layered structure of $[(Si_2O_5)]2-$ and $[Al_2(OH)_4]_2^+$ molecular sheets and a composition of 39.5 wt.% Al_2O_3, 46.5 wt.% SiO_2 and 14 wt.% H_2O [5-10].

Products made from refractory clays occupy a relatively small part of the market, but are irreplaceable in their niche. There is a stable growth of demand for these materials in Georgia, and they are imported. In total, special-purpose ceramic materials (refractory, intended for thermal units, chemically resistant, etc.) worth 6.140 million GEL were imported to Georgia from abroad in 2021, and in 2022 this amount reached 9.043 GEL [11] and it will grow farther.

If promising local raw materials are identified, it will be possible to create small enterprises that will meet the country's need for appropriate products. The aim of this work is to study kaolinized clays of Georgia and develop technology for the production of refractory ceramic materials based on them.

2. MAIN PART

The studies were conducted on kaolinized clays from various deposits in Georgia, such as: *Qobuleti*, *Makhinjauri*, *Brili* and *Makvaneti*, as well as on ceramic materials obtained from them in laboratory conditions.

Results and discussion

Chemical composition of kaolinized clays of Georgia is shown in the Table 1.

It is known that the refractoriness of clays is negatively affected by the alkali and iron content. However, the clays studied contain only small amounts of alkali. Moreover, iron is found primarily in the form of dehydrated crystals.

When studying process parameters, it is necessary to determine the plasticity index, which is calculated as the difference between the upper and lower moisture content limits. Iron oxide and alkali content have a positive effect on plasticity (Table 2).

Table 1

Chemical composition of kaolinized clays of Georgia, wt.%

Location	*LOI*	*SiO_2*	*Al_2O_3*	*Fe_2O_3*	*FeO*	*CaO*	*MgO*	*SO_3*	*Na_2O*	*K_2O*
Qobuleti	9.40	45.51	21.50	4.74	1.13	7.92	3.72	1.53	2.30	1.50
Makhinjauri	9.68	50.79	22.03	7.42	0.62	2.80	2.03	0.21	1.59	1.44
Brili	5.59	57.18	21.27	1.44	1.69	2.43	2.86	0.32	3.41	2.08
Makvaneti	4.14	57.70	27.80	1.14	1.15	0.99	1.97	0.54	2.01	2.05

Table 2

Plasticity parameters of the studied clays

Location	*Upper limit of humidity, wt.%*	*Lower limit of humidity, wt.%*	*Plasticity number*	*Plasticity*
Qobuleti	28.5	53.2	24.7	High
Makhinjauri	30.61	56.51	26	High
Brili	18.8	41.7	22.9	Middle
Makvaneti	24.36	33.59	9.23	Low

The plasticity of clays is well matched with their chemical composition: the least plastic is *Makvaneti* clay, which is distinguished by its minimal content of iron oxides and alkalis.

The results of softening temperature determination are presented in Table 3.

Table 3

Softening temperatures of clays

Location	*Softening temperature,* °C
Qobuleti	>1500
Makhinjauri	>1500
Brili	1400-1420
Makvaneti	>1550

As Table 3 shows, the low iron oxide (Fe_2O_3 + FeO) and alkaline earth oxide (RO) content of *Makvaneti* clay determines its high softening point. Accordingly, in the case of *Qobuleti* and *Makhinjauri* clays, the softening point is reduced by 50°C.

Further studies were conducted to investigate the thermal properties of ceramic materials.

From clay dough of normal density, tiles measuring 50x50x50 mm were made, which were dried naturally for some time, and then in a drying chamber according to a certain regime.

Well-dried tiles were heat-treated using various modes. The suitability of each mode was determined based on the amount of water absorbed

by the ceramic material. After repeated testing, the optimal mode was selected: 200 and 400°C with a 15-minute hold; 600 and 700°C with a 30-minute hold; and 800, 900, 1000, and 1100°C with a 1-hour hold. Using this modes, the maximum firing temperatures were 1050, 1150, and 1200°C, with a hold time of 1 hour at the maximum temperature (Table 4).

Table 4

Selecting the firing mode

Temperature, °C	*Firing holding time, min.*
200	15
400	15
600	30
700	30
800	60
900	60
1000	60
1100	60
1150	60
1200	60

The tiles were heat-treated in a muffle furnace with an open spiral. After firing, the samples were cooled in a deactivated furnace with the door closed. The cooled tiles were visually inspected for color, cracks, and debris.

The color of the fired tiles, depending on the iron oxide content and the heat treatment temperature, is more or less pinkish. Accordingly, the color of fired *Makvaneti* clay tiles ranges from white to light gray. All fired tiles had a smooth surface and clear edges. The structure is monolithic and finely crystalline, without any unnecessary inclusions or pores.

After visual inspection, the geometric dimensions and linear shrinkage (air and fire), volumetric shrinkage (air and fire), as well as the total shrinkage were determined (Table 5).

The data in Table 5 show how shrinkage values vary depending on the temperature during heat treatment. These data must be taken into account to maintain the initial geometric dimensions. As is evident, increasing the heat treatment temperature by 50°C significantly increases shrinkage values.

A comparison of the data in Tables 1 and 5 shows a direct correlation between shrinkage values and the chemical composition of clays. Here, both high iron and alkali oxide contents and low aluminum and silica oxide contents play a negative role. An example of this is *Makvaneti* clay, which is distinguished by its high softening point and low shrinkage values.

Comparing *Qobuleti* and *Makhinjauri* clays reveals that, despite their different Al_2O_3 and RO contents, their technological properties are nearly identical. Apparently, the iron and alkali oxides of these clays are bound into identical alkali-aluminosilicate minerals.

The performance parameters of ceramic materials were determined according to GOST 27180-2001 and GOST 13996-2019.

Among the performance parameters of ceramic materials, water absorption is a significant parameter, which determines their application.

According to Table 6, as expected, water absorption decreases with increasing firing temperature. This is because the ceramic body becomes more finely crystalline and monolithic,

thereby minimizing the number of micropores that cause water absorption.

According to these parameters, ceramic shards obtained from *Qobuleti* and *Brili* clays are characterized as identical, despite the differences in their chemical compositions.

Table 5

Shrinkage of ceramic tiles

Location	*Linear shrinkage, %*			*Volumetric shrinkage, %*		
	Air, 100°C	*Fire, 1050°C*	*General, 1050°C*	*Air, 100°C*	*Fire, 1050°C*	*General, 1050°C*
Qobuleti	9.4	7.24	17.44	16.64	17.61	34.25
Makhinjauri	*8.32*	4.72	13.32	17.29	14.36	31.64
Brili	5.82	7.04	12.86	6.32	15.82	22.14
Makvaneti	4.62	2.14	7.14	6.1	8.82	14.86
1150°C						
Qobuleti	9.4	11.4	21.6	16.64	36.07	52.71
Makhinjauri	8.32	12.6	21.2	17.29	28.57	45.86
Brili	5.82	10.8	16.6	6.32	29.86	36.18
Makvaneti	4.62	11.8	16.8	6.1	27.14	33.21
1200°C						
Qobuleti	9.4	12.6	22.8	16.64	18.28	49.29
Makhinjauri	8.32	17.2	25.8	17.29	36.18	53.46
Brili	5.82	10.98	16.8	6.32	31.18	37.5
Makvaneti	4.62	9.5	14.5	6.1	30.29	36.36

Table 6

Water absorption indicators

Location	*Water absorption of ceramic shards, %*		
	Temperature, °C		
	1050	1150	1200
Qobuleti	18.42	4.53	2.08
Makhinjauri	28.96	12.28	8.45
Brili	17.12	4.93	1.59
Makvaneti	29.94	10.95	8.15

According to Table 6, the optimal firing temperature can be considered to be 1200°C, at which the water absorption of all ceramic samples remains within the normal range (≤10%).

One of the important parameters of ceramic materials is their mechanical strength, which determines the scope of their application.

To determine mechanical strength, 25 mm diameter cylinders and 40 x 40 x 40 mm cubes were formed from clay dough of normal consistency. The samples were fired at 1200°C using the optimal firing conditions and tested in a hydraulic press. The results are presented in Table 7.

Table 7

Mechanical strength indicators

Location	*Compressive strength (MPa)*
Qobuleti	98
Makhinjauri	94
Brili	134
Makvaneti	444

According to Table 7, the relatively low mechanical strength of ceramic materials obtained from *Qobuleti* and *Makhinjauri* clays may be due to the high content of iron oxides and alkalis.

Makgvaneti-based ceramic material exhibits particularly high mechanical strength, which can be explained by its high silica content.

Refractory ceramic materials operate in a constant heating-cooling mode during operation, which can cause cracking and failure. To prevent this, their heat resistance must be tested in accordance with GOST 27180–2001. Above 800–1000°C, refractory materials acquire the property of residual plastic deformation. At this temperature, stresses arise that can be equalized through plastic displacement within the refractory material. Consequently, fluctuations in heating temperature in the plastic deformation region cannot cause the type of failure observed only in the elastic deformation region, i.e., at low temperatures. Therefore, heat resistance is tested in the elastic deformation region at 150°C [3].

GOST 27180–2001 requires testing five samples: tiles at 150°C for 30 minutes and then rapidly cooling to 18–20°C in running water. A material is considered heat-resistant if the tiles withstand 10 cycles without cracking.

The ceramic materials obtained from the clays we studied fully passed the tests and can be considered heat-resistant.

Frost resistance was determined according to GOST 27180–2001 using the freeze-thaw method. After 48 hours of soaking in water, the tiles were placed in a freezer at temperatures ranging from -15°C to -20°C for 2 hours. They were then thawed in running water at 15–20°C for 1 hour. The number of cycles was 50. All samples passed the tests without visible cracks or damage.

For refractory ceramic materials, chemical resistance to acids and alkalis, depending on the operating conditions, is of significant importance. Acid resistance was determined in a 3% HCl solution, and alkali resistance in a 30% KOH solution for 96 hours. All samples passed the tests without any external changes.

In addition to determining the technological and operational parameters, petrographic studies

were carried out on clays and ceramic materials based on them, fired at 1100, 1150 and 1200°C.

Some clays, such as *Qobuleti* and *Makhinjauri*, contain dehydrated iron oxides (magnetite, hematite, and limonite). Unlike the others, the *Makvaneti* clay contains significant amounts of trachyte lithoclasts in the form of sanidine and plagioclase.

After heat treatment of clays at high temperatures, the main clay minerals are no longer identifiable. All minerals are predominantly vitrified (glazed).

When comparing petrographic analysis data from ceramic materials fired at different temperatures, it is noted that they differ primarily in the degree of vitrification of the main clay mineral: the higher the firing temperature, the greater the degree of vitrification.

The mineral background is primarily represented by mono- and polycrystalline quartz grains. Feldspars, which are also subject to vitrification, are present in small quantities. Transparent ore minerals are found in sufficient quantities as small isotropic iron oxide grains. Mica minerals rich in biotite and iron are rarely observed.

Figures 1 - 4 show micrographs of ceramic materials fired at 1150°C.

1. Ceramic materials based on *Qobuleti* clay

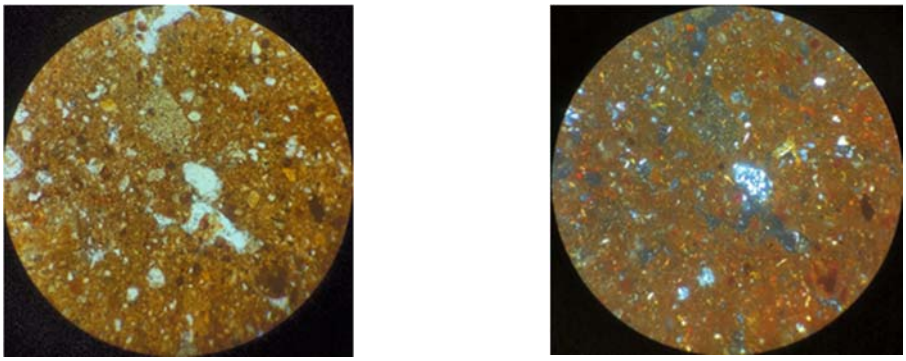

a(II) b(+)

Fig. 1.1. Crystal-lithoclastic material in an isotropic vitrified matrix. 135X

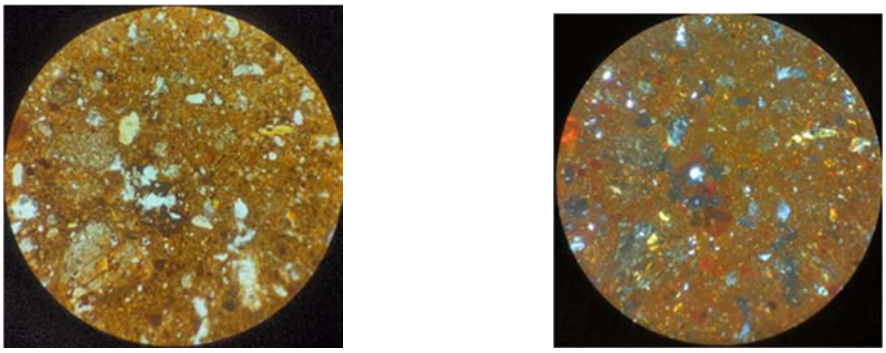

a(II) b(+)

Fig. 1.2. Lithoclastic inclusion enriched in iron oxides. 135X

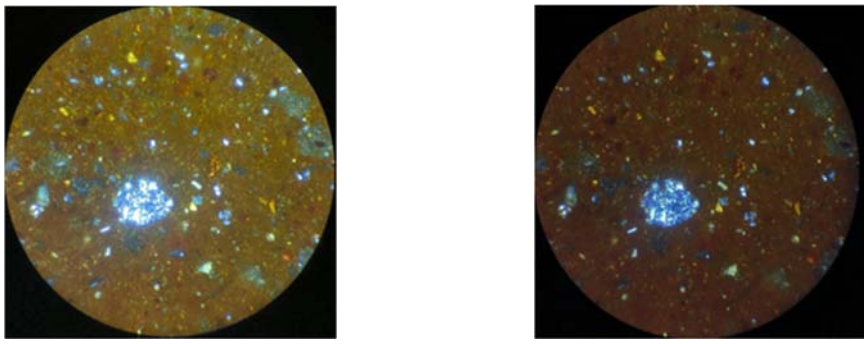

a(II) b(+)

Fig. 1.3. Thermally altered feldspar grain. Inclusions of microcrystals of varying composition are observed in the clay mass. 135X

2. Ceramic materials based on *Makhinjauri* clay

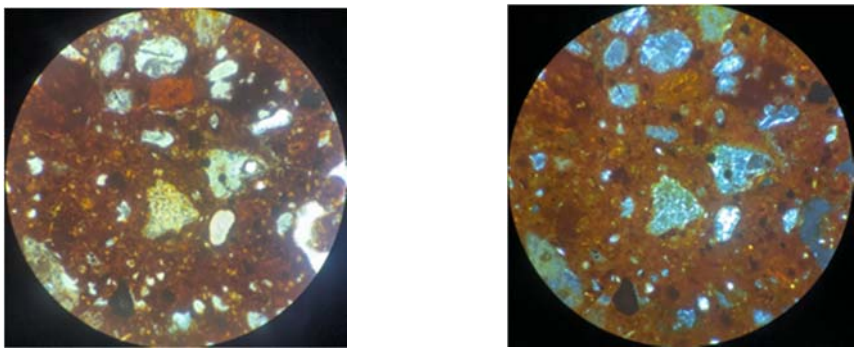

a(II) b(+)

Fig. 2.1. Lithoclastic inclusions of different compositions, associated with a pelitic matrix. 135X

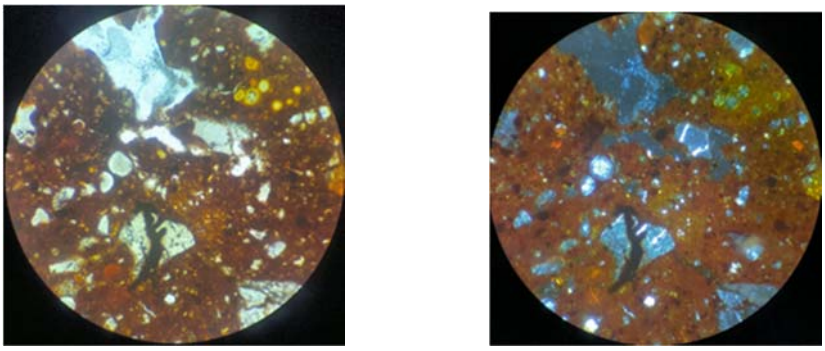

a(II) b(+)

Fig. 2.2. Radiation inclusions of limonite and carbonate compositions in a vitrified matrix. 135X

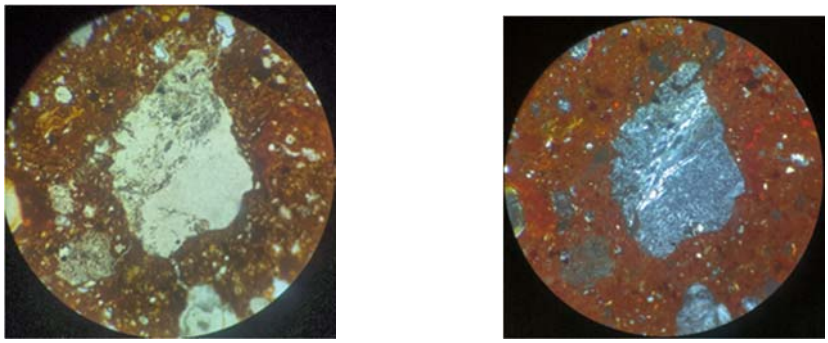

a(II) b(+)

Fig. 2.3. Clast inclusion of highly altered feldspar. 135X

3. Ceramic materials based on *Brili* clay

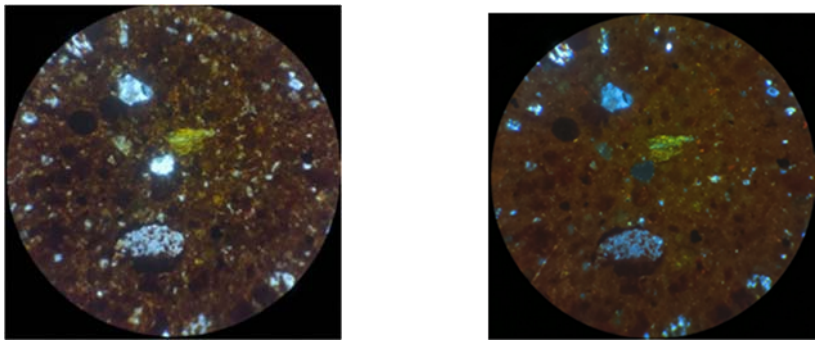

a(II) b(+)

Fig. 3.1. Vitrified feldspar inclusion in a vitrified matrix. 135X

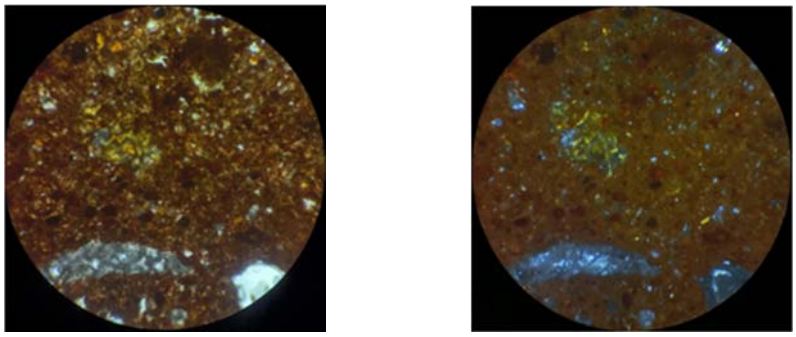

a(II) b(+)

Fig. 3.2. Lithoclastic inclusions altered by iron oxides in a vitrified matrix.

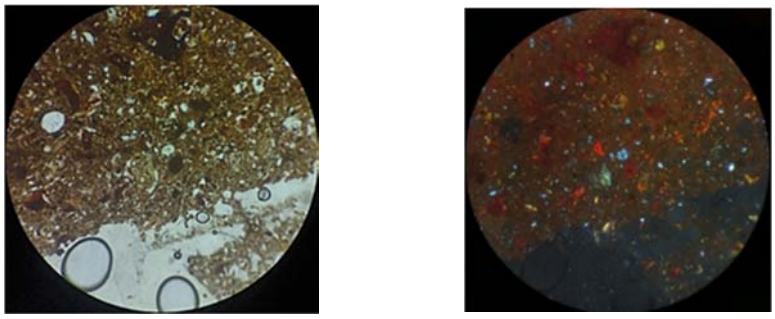

a(II) b(+)

Fig. 3.3. Lithoclastic inclusions altered by iron oxides in a vitrified matrix.

4. Ceramic materials based on *Makvaneti* clay

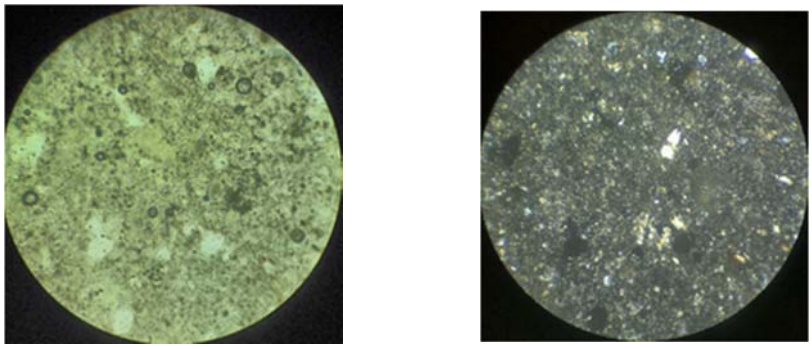

a(II) b(+)

Fig. 4.1. Trachyte-containing lithoclasts
in an isotropic vitrified matrix. 135X

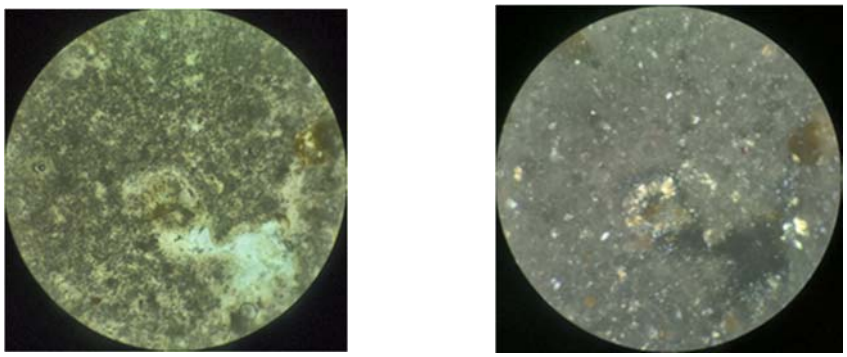

a(II) b(+)

Fig. 4.2. Spherulitic forms in the main vitrified clay mass. 135X

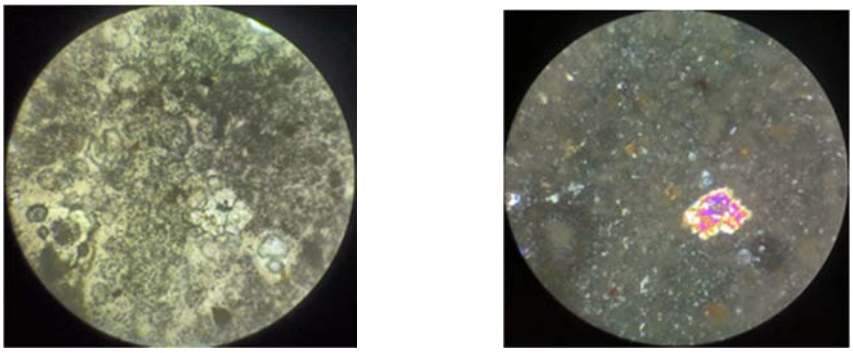

a(II) b(+)

Fig. 4.3. Crystalloclastic quartz grain. Interference colors are caused by the mass of the mineral. 135X

3. CONCLUSION

Based on the results of the research, it can be concluded that refractory ceramic materials can be produced using kaolinized clays from the *Qobuleti*, *Makhinjauri*, *Brili*, and *Makvaneti* deposits in Georgia.

A process technology for producing refractory ceramic materials has been developed, and the key technical and operational parameters have been studied. The optimal firing temperature has been established at 1200°C.

The developed materials are suitable for use as linings in heating units. They can also be used to manufacture products such as façade (clinker) bricks and tiles for wall and road cladding exposed to harsh climates and aggressive environments—chemically resistant tiles.

Acknowledgments

This work was supported by the Shota Rustaveli National Science Foundation of Georgia (SRNSFG) [grant number YS-23-267].

The authors express their gratitude to the Shota Rustaveli National Science Foundation of Georgia.

REFERENCES

1. I. Riley, M. Burbidge. The global cement industry and technology: past, present and future. Cement and its Applications. 2025.
2. M. Schneider. The cement industry on the way to a low-carbon future. Cement and Concrete Research, vol. 124, p. 105792, 2019.
3. P. P. Budnikov, A.C. Berejhnoi, I. A. Bulavin, G. P. Kalliga, G. V. Kukolev, D. N. Poluboyarnikov. Technology of ceramics and refractories. Gosstroyizdat. Moscow. 1972.
4. A.N. Avgustinik. Ceramics, Promstroyizdat. Moscow, 1957, p. 15.
5. P.J. Sánchez-Soto, D. Eliche-Quesada, S. Martínez-Martínez, L. Pérez-Villarejo, E. Garzón. Study of a Waste Kaolin as Raw Material for Mullite Ceramics and Mullite Refractories by Reaction Sintering. Materials 2022, 15(2), 583; https://doi.org/10.3390/ma15020583
6. Pask, J.A.; Tomsia, A.P. Formation of mullite from sol-gel mixtures and kaolinite. J. Am. Ceram. Soc. 1991, 74, 2367–2373.
7. Carty, W.M.; Senapati, U. Porcelain-Raw Materials, Processing, Phase Evolution and Mechanical Behavior. J. Am. Ceram. Soc. 1998, 81, 3–20.
8. Hammas, A.; Lecomte-Nana, G.; Daou, I.; Tessier-Doyen, N.; Peyratout, C.; Zibouche, F. Kaolinite-Magnesite or Kaolinite-Talc-Based Ceramics. Part II: Microstructure and the Final Properties Related Sintered Tapes. Minerals 2020, 10, 1080.
9. Galán, E.; Ferrell, R.E. Genesis of Clays. In Handbook of Clay Science. Developments in Clay Science; Bergaya, F., Lagaly, G., Eds.; Elsevier B.V.: Amsterdam, The Netherlands, 2013; Volume 5, pp. 83–126.
10. V. José da Silvaa, S. K. A. Taveiraa, K. R. Silvaa, G.A. Nevesa, H.L. Liraa, L.N. L. Santanaa. Refractory Ceramics of Clay and Alumina Waste. Materials Research. 2021; 24(2). DOI: https://doi.org/10.1590/1980-5373-MR-2020-0485.
11. www.geostat.ge,

უაკ 666.3

ძნელადდნობადი კერამიკული მასალების მიღების შესაძლებლობის კვლევა საქართველოს კაოლინიზირებული თიხების საფუძველზე

თ. პეტრიაშვილი, ე. შაფაქიძე, ი. ქამუშაძე, ლ. გაბუნია, ი. გეჯაძე, მ. მაქაძე

ივანე ჯავახიშვილის სახელობის თბილისის სახელმწიფო უნივერსიტეტი, ალექსანდრე თვალჭრელიძის სახელობის მინერალური ნედლეულის კავკასიის ინსტიტუტი. საქართველო, 0186, თბილისი, მინდელის 11

E-MAIL: t.petriashvili25@gmail.com, elena.shapakidze@tsu.ge

რეზიუმე: ***მიზანი.*** სამუშაოს მიზანია საქართველოს კაოლინიზირებული თიხების შესწავლა და მათ საფუძველზე ძნელადდნობადი კერამიკული მასალების წარმოების ტექნოლოგიის შემუშავება.

მეთოდი. გამოყენებულ იქნა ქიმიური და პეტროგრაფიული ანალიზის მეთოდები.

მინერალური შედგენილობები შესწავლილ იქნა Optika B-383POL (იტალია) პოლარიზაციული მიკროსკოპის მეშვეობით.

ფიზიკურ-მექანიკური და თერმული თვისებები გამოიცადა 40x40x40მმ ზომის კუბებზე და 50x50x10 მმ ზომის ფილებზე.

შედეგი. შემუშავებულ იქნა ძნელადდნობადი კერამიკული მასალების წარმოების ტექნოლოგია და შესწავლილ იქნა მათი ძირითადი ტექნიკური და საექსპლუატაციო პარამეტრები.

დასკვნა. კვლევის შედეგებზე დაყრდნობით შეიძლება გაკეთდეს დასკვნა, რომ საქართველოს კაოლინიზირებული თიხების (ქობულეთის, მახინჯაურის, ბრილის და მაკვნეთის) გამოყენებით შესაძლებელია ძნელადდნობადი კერამიკული მასალების მიღება.

შემუშავებულია იქნა ძნელადდნობადი კერამიკული მასალების წარმოების ტექნოლოგია და შესწავლილია მათი ძირითადი ტექნიკური და საექსპლუატაციო პარამეტრები. დადგინდა გამოწვის ოპტიმალური ტემპერატურა 1200°C.

შემუშავებული მასალების გამოყენება შესაძლებელია თბურ აგრეგატებში ამონაგის სახით. მათგან შესაძლებელია ისეთი ნაკეთობების დამზადება, როგორიცაა საფასადე (კლინკერის) აგური და ფილები კედლების და გზების მოსაპირკეთებლად, რომლებიც მკაცრი კლიმატური პირობების და აგრესიული გარემოს ზეგავლენას განიცდიან.

საკვანძო სიტყვები: კაოლინიზირებული თიხა, კაოლინი, ძნელადდნობადი კერამიკული მასალა, კერამიკა.

DOI https://doi.org/10.36073/2960-9534

THE GEORGIAN CERAMISTS ASSOCIATION JOINED
THE INTERATIONAL CERAMIC FEDERATION SINCE 2008

THE GEORGIAN CERAMISTS ASSOCIATION HAS BEEN A MEMBER
OF THE EUROPEAN CERAMIC SOCIETY SINCE 2002

THE GEORGIAN CERAMIC ASSOCIATION WAS FOUNDED IN 1998
THE MAGAZINE WAS FOUNDED IN 1998

TBILISI, "INTERNATIONAL JOURNAL OF CERAMICS, COMPOSITES, SCIENCE AND ADVANCED TECHNOLOGIES", Vol. 27. 2(54). 2025

Reference of magazine is obligatory on reprinting

Print circulation 5,5. Contract amount 50. Printed A4 format.

GEORGIAN CERAMISTS ASSOCIATION. Tbilisi. Str. Kostava 69. Phone: +995 599 151957
E-mail: kowsiri@gtu.ge, Zviad Kovziridze

http://ceramics.gtu.ge